Laser diagnosis and computer modelling of C/H/O and C/H/N plasmas used in diamond chemical vapour deposition

Mark Kelly

A dissertation submitted to the University of Bristol in accordance with the requirements for the award of the degree of Doctor of Philosophy in the Faculty of Science.

School of chemistry

Abstract

Laser and optical emission spectroscopies have been employed to study the gas phase chemistry in the growth environment for diamond chemical vapour deposition (CVD) in a microwave (MW) reactor. Computational investigations have also been used to explore the energetics of elementary reactions on a diamond surface, to give insight into which species are likely to incorporate into a growing diamond film. The focus of this thesis is on O and N containing C/H plasmas.

Cavity ring down spectroscopy (CRDS) and optical emission spectroscopy (OES) were used to study $CH_4/CO_2/H_2$ and CO/H_2 plasmas. Spatially resolved column densities for C_2, CH, H(n=2) and OH were measured by CRDS for a range of process conditions (flow rates, pressure, power, *etc*.). Emissions from C_2*, CH*, H(n=3), OH* and CO* were also measured. OES and CRDS results were then used to validate a 2D model describing the plasma activation and gas phase chemistry. Such modelling reveals that $CH_4/CO_2/H_2$ plasmas have a lower thermal conductivity than CH_4/H_2 plasmas, which is why the same gas temperature (T_{gas}) can be obtained in the former plasma at a common pressure (150 Torr) using an applied MW power of 1 kW (*cf*. 1.5 kW in a CH_4/H_2 plasma). CO/H_2 plasmas yielded significantly lower CH and C_2 column densities, and negligible diamond growth when compared with $CH_4/CO_2/H_2$ gas mixtures with the same C/H/O mole fraction ratio.

Nitrogen containing plasmas have been explored also, as these underpin all CVD of semiconducting N-doped diamond. Spatially resolved column densities of C_2, CH, H(n=2), CN and NH and emissions from C_2*, CH*, H(n=3), CN*, NH* and N_2* were measured in N_2/H_2, NH_3/H_2, $N_2/CH_4/H_2$ and $NH_3/CH_4/H_2$ plasmas, as functions of process parameters. The distributions and column densities of NH in N/H plasmas, and of NH and CN in C/N/H plasmas, were found to be sensitive to the choice of N atom source (NH_3 *vs*. N_2). NH column densities in NH_3/H_2 plasmas were larger and more extensive than in a N_2/H_2 plasma with equivalent N mole fraction. NH column densities in C/N/H plasmas were lower than in N/H plasmas with the same N mole fraction, and both the NH and CN column densities were found to be larger in C/N/H plasmas involving NH_3 rather than N_2. All of the experimental observations indicate that NH_3 is a much more active participant in the gas phase plasma chemistry - consistent with the lower bond strengths in NH_3 compared with N_2. Such findings should serve to inspire future detailed modelling of microwave activated N/C/H gas mixtures.

Elementary reactions of OH, NH, N, and CN and HCN on a diamond surface have been investigated using quantum mechanical (QM) and quantum mechanical / molecular mechanical (QM/MM) techniques. Energetically favourable pathways for OH, N and CNH incorporation into a growing diamond film were identified. Addition of a CNH moiety, with a pendant N atom extending above the growing layer, could act as a nucleation site for next layer growth – thereby offering a possible explanation for the oft reported finding of increased diamond growth rates when N containing species are present in the process gas mixture.

Acknowledgement

I would like to thank my supervisor, Professor Mike Ashfold for his support, guidance and encouragement throughout my PhD. I would also like to thank Dr Colin Western for his support with Pgopher and Professor Jeremy Harvey for his assistance with computational investigations. I would like to give thanks and gratitude to Dr James Richley for passing on his knowledge of the CRDS experiment and QM / QM/MM calculations. Thanks go to Dr Yuri Mankelevich for his continued expertise and support. Additional thanks goes to Dr James Smith, Mr Keith Rosser, and Dr Ben Truscott for their technical advice and assistance with experimental work. Finally, I would like to thank Element Six Ltd for sponsoring half of my PhD, for the loan of the microwave reactor, and for guidance throughout my PhD.

Declaration

I declare that the work in this thesis was carried out in accordance with the requirements of the University's Regulation and Code of Practice for Research Degree Program's and that it has not been submitted for any other academic reward. Except where indicated by reference throughout the text, the work is the candidates own work. Work completed in collaboration with, or with the assistance of others is indicated. Any views expressed in this thesis are views of the author.

SIGNED: _____ DATE: _____

Contents

List of Figures

List of Tables

Chapter 1 Introduction

1.1 Diamond: structure, properties and areas of research.

Diamond is a metastable allotrope of carbon, in which carbon atoms are bonded together in an sp^3 hybridised tetrahedral network, with a face centered cubic unit cell. The result of this solid tetrahedral array of carbon atoms creates the hardest natural material known to man. The tetrahedral orientation of carbon atoms is shown below in fig. 1.1 (a). Fig 1.1 (b) shows the bonding in a single layer of graphene, which forms sp^2 hybridised bonds between C atoms.

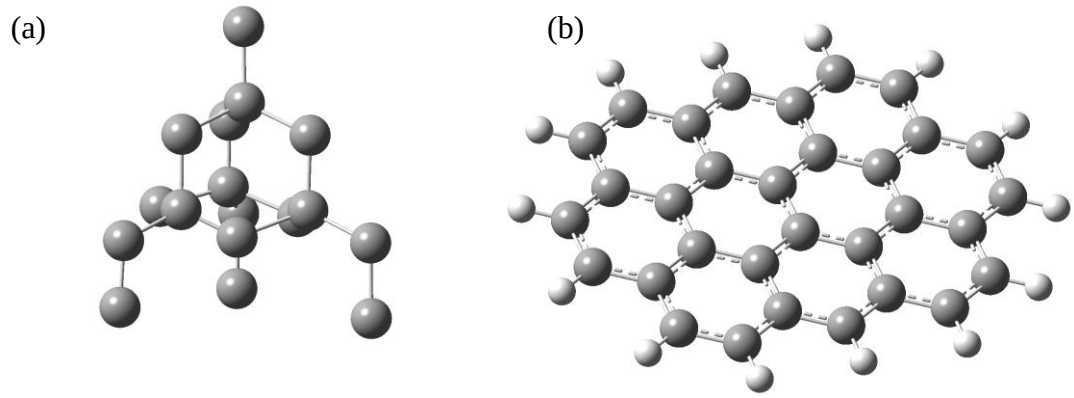

Fig. 1.1 Different allotropes of carbon, where (a) is diamond, and (b) is graphene.

The crystalline structure of diamond provides it with extremely useful properties, which make diamond a valuable material with industrial applications. For example, the extreme hardness, high thermal conductivity and low thermal expansion coefficient allows diamond to be used in devices, which are used in extreme conditions at high temperatures. One area, which commonly uses diamond, is in the abrasives industry.[1] For example, if a drill-bit is coated with a polycrystalline diamond (PCD) layer, the hardness of diamond greatly enhances its cutting power, and the high thermal conductivity of diamond stops the material from overheating. In order for films to have high thermal conductivities they should preferably be thick with a low number of grain boundary networks, as these may contain impurities.[2] The high thermal conductivity of diamond makes it useful as a heat sink, especially in

electronic devices.[3] Diamond also has a high optical transparency, transmitting light from the UV through to the IR. Having a high optical transparency makes diamond useful in applications such as optical windows.[4] In order for diamond have high optical transparency, it must have high crystallographic perfection with few impurities. All of these properties are utilized in using diamond in extreme conditions, such as IR windows for heat sensing cameras, domes for high-speed missiles, or as heat sinks in diode lasers.[5–7]

Diamond can also be used in electronic devices. When diamond is un-doped, it has a large band-gap (5.45. eV),[8] and so behaves as an insulator. However, diamond can become a conducting material when doped. For example, p-type doping of diamond with boron creates a semiconducting material, and below a certain concentration, $[B]<2 \times 10^{19}$ cm^{-3}, the sample conducts via a process called variable range hopping.[9,10] When $[B]>2 \times 10^{19}$ cm^{-3}, the doped diamond film will behave like a metal, and when these samples are cooled to below a critical temperature, (2 K), they can even behave as superconductors.[9–13] Diamond can also be doped with nitrogen,[14] however this is not as effective as boron at producing a semiconductor, and conduction in this case mainly occurs due to an increase in the formation of C=C bonds in grain boundaries.[15] Nitrogen is beneficial to diamond in other ways, such as increasing film growth rate,[16,17] however this will be discussed in greater detail in chapter 6.

1.2 Chemical vapour deposition of diamond

Chemical vapour deposition (CVD) involves the activation of a gas mixture, followed by the adsorption/incorporation of gas phase species onto the surface of a solid material.[18–21] In diamond CVD, activation of the gas mixture creates an abundance of gas phase radicals, ions and molecules. However, methyl radicals and hydrogen atoms are the main species responsible for diamond growth, and therefore the reactor must contain a gas mixture with a carbon and hydrogen source, as well as an energy source to activate the gas.[22] The species responsible for diamond growth are created in the activated gas mixture,[23] and diamond is grown via CVD as shown in fig. 1.2. This

section discusses some of the methods available for activation of the gas mixture responsible for diamond CVD.

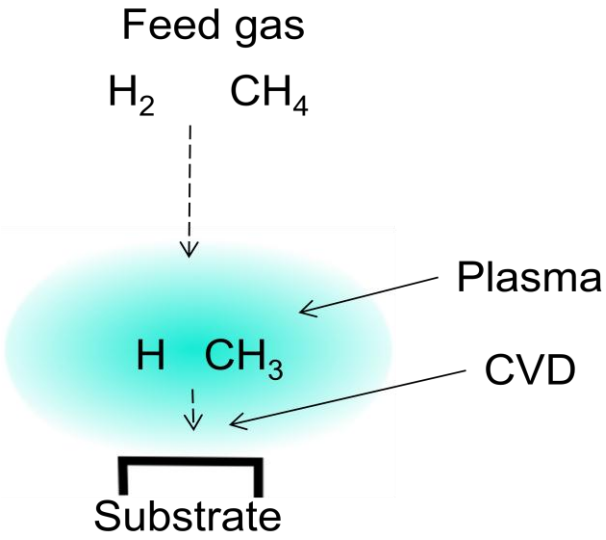

Fig. 1.2. The CVD process in a CH_4/H_2 reactor, showing the main species responsible for diamond growth.

1.2.1 Hot filament

Hot filament (HF) reactors (fig. 1.3) for diamond CVD work by activating the gas mixture, usually CH_4/H_2, using a metal filament, (fig.1.3, **5**) such as Ta, usually heated to around 2000-2500^{o}C. This filament within the reactor acts as a catalyst and power source to dissociate H_2 molecules into H atoms. These H atoms then have the effect of activating the gas mixture. The film is grown on a pre-seeded substrate, such as Si or Mo, which is heated separately by a power source to around 900^{o}C.

However, HF reactors have limitations. One of these is that they cannot run at very high growth rate (G), eg. > 4 μm/h, due to parameters such as filament temperature and pressure. If the filament temperature is too high, there may be incorporation of filament atoms in the grown film. With regards to pressure, it is usually low, at around 5-20 Torr.[24] However, some reactors can run at pressures such as 100 Torr.[25] Another drawback of these reactors is the finite surface area of the filament used; if too much

CH_4 is fed into the reactor, the filament can easily become coated in a layer of carbon in place of hydrogen, and result in the formation of graphitic carbon, which may form graphitic impurities on the growing diamond film. The choice of feed gas used is also important to consider in HF reactors, as the use of novel gas mixtures could lead to degradation of the filament, such as the presence of O being able to oxidise and destroy the metal HF. The distance and position of the filament to the growing surface is also an important parameter to consider in HF reactors, in order to maintain a hot enough gaseous region to accommodate the necessary gas phase chemistry, and to ensure uniformity across the grown film. A study by Quiping *et al.* [26] found that the quality of diamond grown in a HF reactor decreased with distance away from the filament.

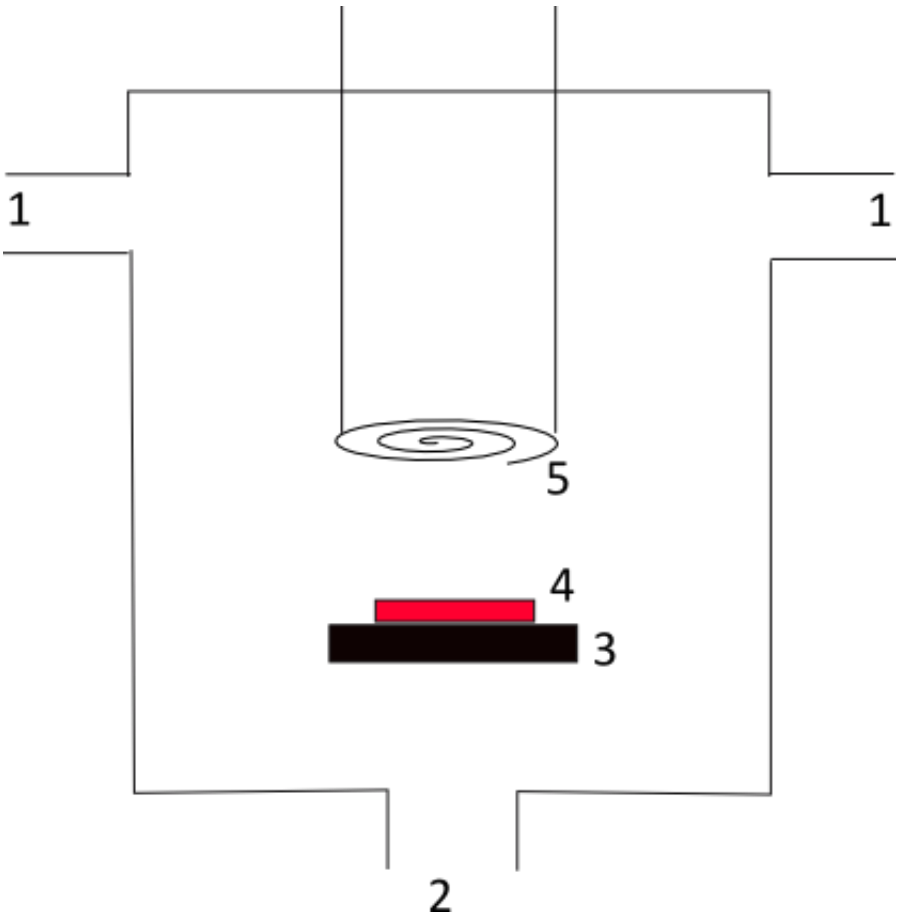

Fig. 1.3. Schematic of a HF reactor. **1** represents the gas inlet system, **2** represents the gas outlet, **3** represents the substrate holder, **4** represents the substrate and **5** represents the filament.

Although there is a limited gas volume which can be activated by a single filament in a HF reactor, there are multifilament reactors on the market capable of growing diamond over much larger areas than can be achieved in a microwave MW reactor.[27]

1.2.2 Microwave reactors

Microwave reactors (MW) work by activating a gas mixture with microwave power to create a plasma. Microwaves are directed into the reactor where they interact with electrons, which then undergo collisions with gas phase molecules. Inelastic collisions result in the excitation of these species, which can then lead to both ionization and dissociation. The advantage of using a MW reactor is that they can be run at higher power and pressure than HF reactors. The result of this is that higher growth rates (G) can be achieved. Though most commercial reactors will offer independent substrate heating/cooling to allow for the optimization of the substrate temperature (T_{sub}), MW reactors do not require separate substrate heating, as the hot plasma heats the substrate. Power (P) and pressure (p) can be controlled to achieve the optimum growth temperature. Another advantage of using MW over HF reactors is the ability to use alternative gas mixtures to the conventional C/H gas mix, as no consideration has to be taken into the degradation of the power source. The purity of the grown material is also an advantage of growing diamond in MW reactors, compared to HF reactors, in which degredation of the HF can cause film contamination.

1.3 Gas phase chemistry in a MW reactor

The gas phase within a microwave reactor for diamond CVD consists of a mixture of atoms, ions, radicals and stable molecules. These are constantly undergoing a complex series of collisions and reactions, which lead to formation of a steady state concentration of the carbon radicals responsible for diamond growth.

1.3.1 The Bachmann diagram

The Bachmann diagram is a C/H/O phase diagram, first proposed by Bachmann *et al.* in 1991,[28] and has been re-evaluated by others since.[29] The Bachmann diagram is shown in fig. 1.4, where the three vertices are labeled for H, C and O. A point on a line connecting two vertices represents a gas mixture only composed of the labeled vertices which the line connects, and everything within the triangle represents a mixture of H, C and O. A typical gas feed for diamond growth in a MW reactor consists of a dilute CH_4/H_2 mixture, which is situated around the H vertex on the diagram. The Bachmann diagram was composed to show how the addition of O to the gas phase would affect the diamond growth. There are three main regions to the diagram representing: successful diamond growth, the growth of non-diamond carbonaceous material and conditions where diamond nor any other carbonaceous deposit would not be expected to grow. The area for successful diamond growth connects the H-vertex to the side of the phase diagram connecting C and O. The Bachmann diagram in fig. 1.4 will be discussed further in chapter 3.

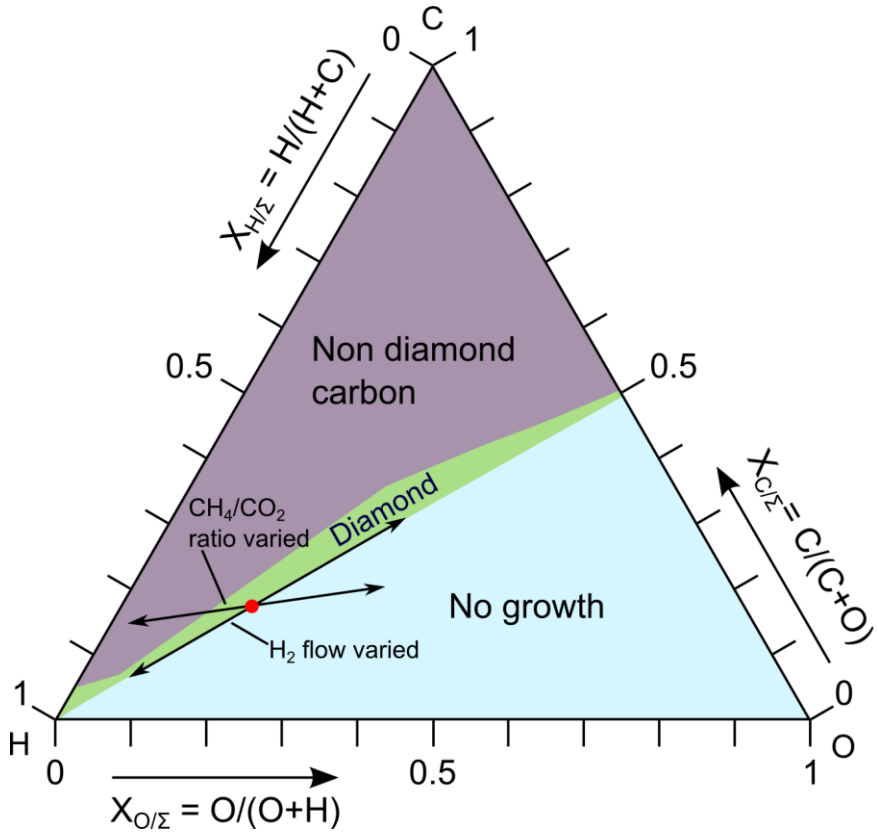

Fig. 1.4. The Bachmann diagram

1.3.2 Chemistry within a $CH_4/H_2/(Ar)$ plasma

As the conventional gas mixture used for diamond CVD is one containing CH_4 and H_2, often with the inclusion of Ar, it is important to consider and to understand the gas phase chemistry prevailing in this environment. Firstly, it is important to consider the chemistry within different areas of the plasma. In a MW reactor, there exists a large temperature gradient from the reactor walls to the hot plasma core; around 500→3000 K. The plasma within a MW reactor can therefore be split into different local temperature regions, within which there are differences in chemistry, which has an effect on species distribution.[23]

The splitting of the plasma into three main temperature regions affects the distribution of CH_4 and C_2H_2, which is related to [H]. In a study by Gicquel *et al.* [30] it was found that below 2500 K, the breaking apart of H_2 is dominated by electron impact dissociation, and above 2500 K by thermal dissociation. Atomic H, although formed mainly in the hot region, is a very light, mobile species, and so can diffuse throughout the reactor volume. The three temperature regions into which the plasma can be split are: (a) 500 K< T< 1400 K, (b) 1400 K<T< 2000 K and (c) 2000 K<T< 3000 K. In the first region (a), the $C_2H_2 \rightarrow CH_4$ reaction prevails. This reaction is dependent upon H atoms.[24] In region (b) however, the opposite $CH_4 \rightarrow C_2H_2$ reaction prevails, which involves the net consumption of H atoms. In the hottest plasma region (c) the higher [H] ensures fast H-shifting and H-recombination reactions, and so there is an equilibrium between CH_4 and C_2H_2 species, however above 2000 K, this equilibrium lies strongly in favor of C_2H_2, as this is the most thermodynamically stable species.[23] A diagram to show the H shifting reactions between CH_x and C_2H_x species is shown in fig. 1.5. This diagram also shows the combination of CH_x species, forming a C_2H_x species. These reactions are essential for forming the CH_3 radical for growing diamond, and fig. 1.5 shows the importance of H in activating the gas mixture.

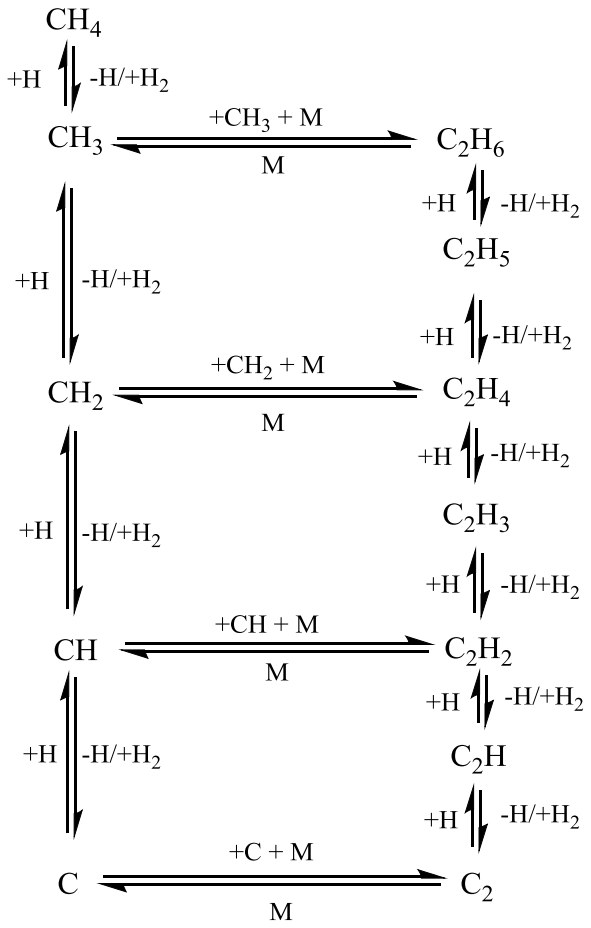

Fig. 1.5. Illustration of the chemistry between CH_4 and C_2H_2 within the plasma for diamond CVD.

It has also been shown that the distribution and number densities of carbon containing species within the plasma is independent of the hydrocarbon source gas[31] used as shown in fig 1.6, however is still dependent upon the C/H ratio in the input gas mixture. Fig. 1.6 shows how the same column densities of H(n=2) atoms, and C_2 and CH radicals are reached regardless of whether CH_4 or C_2H_2 are used in the source gas. This is because the same local thermodynamic equilibrium between CH_x and C_2H_y due to the reaction mechanisms as shown in fig 1.5.

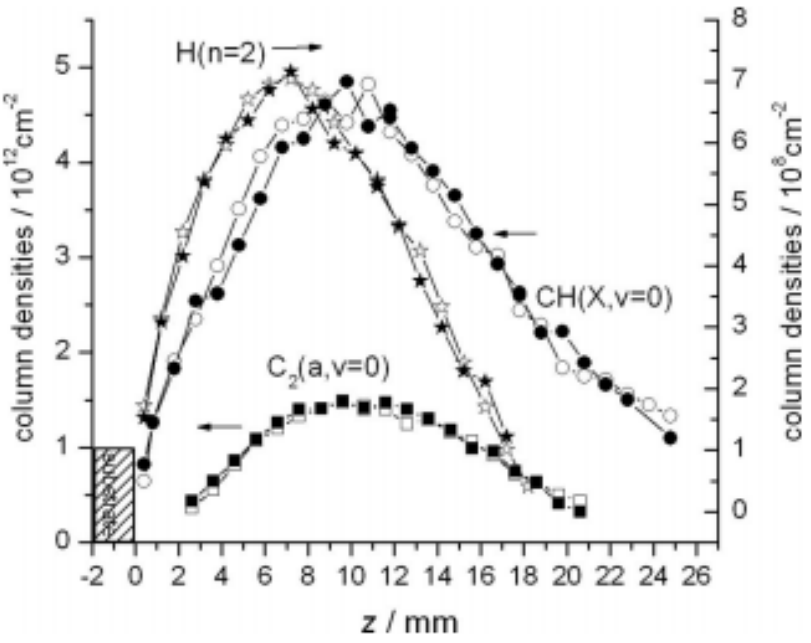

Fig. 1.6. Column densities of C_2, CH and H(n=2), in CH_4/H_2 (open symbols) and C_2H_2/H_2 (closed symbols) plasmas within a MW reactor, where z is the height above the substrate.[31]

The inclusion of a noble gas in the plasma can help to stabilize the discharge, and Ar is often added to the C/H gas mixture, which helps to localize the absorbed input power into a smaller plasma volume. Roberstson *et al.* studied the effects of varying the noble gas added to the plasma, ranging from He to Kr,[32] and found that increasing the mass of the inert gas affected the thermal conductivity of the plasma. The study focused on conditions for growing ultrananocrystalline diamond (UNCD) films, and so the fraction of the inert gas was >80%. Ar was found to be the most useful as it has the effect of decreasing the thermal conductivity of the plasma, therefore allowing the use of a lower input power to create the required gas temperature. Using He increased the thermal conductivity of the plasma relative to using Ar, as He is a much lighter species, and very close in mass to H. Addition of >80% He increased the size of the plasma and made it more diffuse.

1.3.3 Gas phase composition effects on growth

Varying the ratio of C/H within the plasma, with and without the inclusion of Ar, dramatically affects the structure of diamond grown. The growth species for diamond is expected to be the CH_3 radical.[33] In order of increasing average crystallite sizes, structures grown under different growth environments vary from UNCD, nanocrystaline diamond (NCD), microcrystalline diamond (MCD) to single crystalline diamond (SCD).

UNCD films are grown under conditions where the gas phase consists of only around $1\%CH_4/1\%H_2/98\%Ar$. With such a small CH_4 concentration in the feed gas, (G) for UNCD films are expected to be slow.[34,35] The small crystallite sizes with diameter d <10 nm arise from the lack of hydrogen above the growing surface which greatly reduces the chances of forming radical sites and also reduces CH_2 migration. This leads to an increase in nucleation sites. Removing Ar from the plasma and having a $5\%CH_4/95\%H_2$ gas mixture grows NCD films, which have larger crystalline facets, where 10 nm < d < 1μm. If the CH_4/H_2 ratio is then reduced further to $1\%CH_4/H_2$, this has the affect of decreasing $[CH_3]$ at the surface. This reduces the adsorbed CH_x groups on the surface, and gives migrating CH_x groups a greater chance of reaching a step edge rather than encountering another CH_2 group, reducing the opportunity to create other nucleation sites. This has the effect of increasing the crystal size where, 1 μm < d < 1 mm, this corresponds to MCD. SCD films[36] are grown with as much as a $10\%CH_4/H_2$ mixture, but at higher power densities, so that in comparison to other structures mentioned, there is 100x more atomic H at the growing surface, allowing the growth of films with d>1mm, and at much higher G.

1.4 Surface Chemistry

Understanding the surface chemistry in the CVD process is crucial to optimizing diamond growth conditions. This includes considering surface reactions, which lead to the incorporation of gas phase species into films, as well as routes by which adsorbed species may leave the surface.

1.4.1 Models for growth

Since the early 1990's, several different mechanisms for diamond growth have been proposed, and now the argument is strongly in favor of the CH_3 radical being responsible for C incorporation.[31,37,38] In the early years of modelling diamond growth, Harris *et al.* proposed a mechanism for CH_3 addition on a C_9 cluster, adamantane, representative of a diamond (100) surface.[33] This reaction mechanism shows an early theoretical study of the successful incorporation of a gas phase CH_3 radical into diamond, as can be seen in fig.1.7.

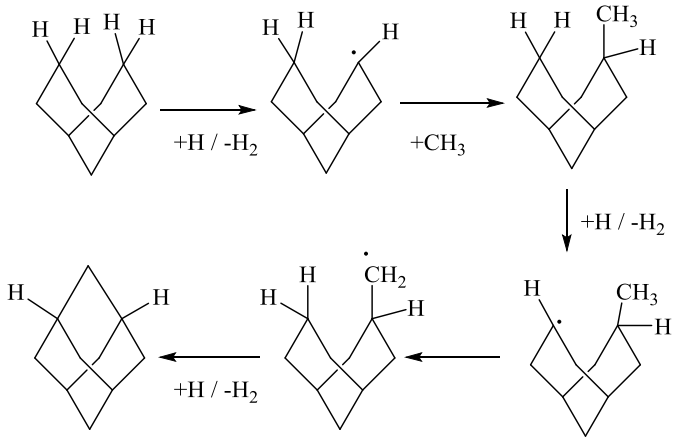

Fig. 1.7. Diamond growth mechanism proposed by Harris *et al.* [33] on a (100) surface.

This mechanism has been developed further since 1990 by Cheesman *et al.*[39] to show an energetically feasible mechanism for the incorporation of carbon into diamond, as in fig. 1.8. This is the same as in fig. 1.7, but on the 2 x 1 (100) reconstructed surface.

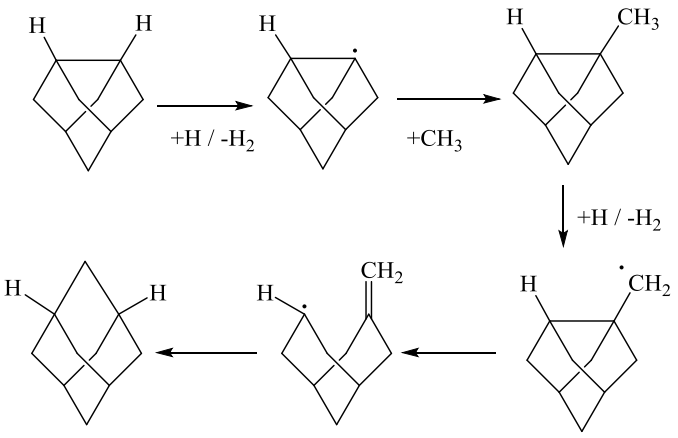

Fig. 1.8. Growth mechanism on a (100) 2 x 1 reconstructed surface

Others have considered the C_2 radical as being responsible for diamond growth.[40,41] In 1994 Skokov *et al.*[42,43] proposed a mechanism for the adsorption of acetylene to a diradical site on a diamond surface. In terms of the main growth species, however, CH_3 radicals are calculated to be in greater abundance than C_2 radicals at the growing diamond surface[23], so will have a higher rate of interactions with the surface. Once adsorbed, however, the C_2 radical is more likely to hydrogenate and then etch from the surface, such as via the β-scission reaction.

1.4.2 β-scission reaction

The β-scission reaction is a proposed mechanism for the cleavage of adsorbed surface species containing more than one atom linked together in a chain.[44] This mechanism gives an etch route for C_xH_y (x>1) species, and removal of non-diamond carbonaceous material from a growing surface. The β-scission mechanism for C_2H_5 is shown in fig. 1.9. This mechanism shows the removal of the C_2H_5 β-H atom, along with the removal of C_2H_4. This creates an ethylene molecule, and a radical site on the diamond surface.

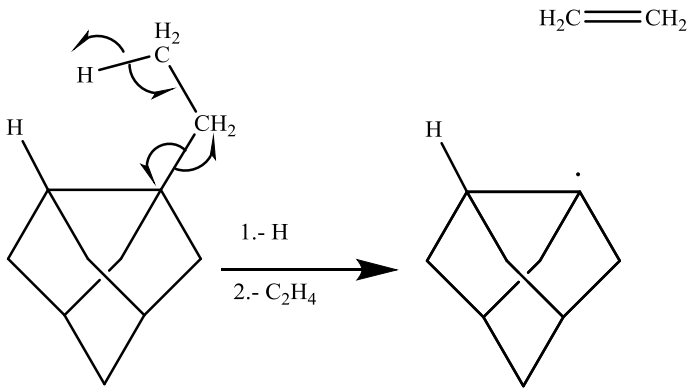

Fig. 1.9. The *β*-scission mechanism for an adsorbed C_2H_5 group.

The removal of the *β*-hydrogen from the adsorbed C_2H_5 results in the subsequent cleavage of the diamond-C bond, etching the C_2H_4 group from the surface. The β-scission reaction was also proposed to account for the removal of a CN group by Butler *et al.*[45]

1.4.3 Surface migration

The migration of hydrocarbon groups on a diamond surface is thought to be an important mechanism in diamond growth and in the formation of a smooth diamond surface. Cheesman *et al.*, and others [39,46–48] investigated the migration of a CH_2 group along and across a dimer chain on the 2 x1 (100) reconstructed H-terminated diamond surface. This is explained further in Chapter 6.

1.5 The Bristol-Moscow model

Collaborations between Bristol and Moscow for the modelling of plasmas in diamond CVD using MW reactors has provided a wealth of detailed information into the complex processes occurring when using a variety of different gas mixtures for diamond CVD.[20,49]

Optical emission spectroscopy (OES) and cavity ring-down spectroscopy (CRDS) are used to monitor the plasma whilst varying conditions to build up a picture of how the

concentrations of select species are affected by changing parameters. Results obtained experimentally are then used to validate a 2D model, which is comprised of three main blocks describing:

1. Power absorption, heat/ mass transfer and gas heating.
2. Plasma activation, plasma chemical kinetics and species diffusion.
3. Gas-surface processes

In the model, the plasma size is treated as an external parameter and is guided by experimental results. Plasma activation involves the absorption of generated microwaves by electrons, which then undergo interactions with gas phase species. The rate coefficients for e-atom or e-molecule interactions are calculated as a function of the electron temperature and gas temperature. The absorbed power density, Q, is then calculated as a sum of power losses/gains from electron-particle interactions. Previous calculations[23] for CH_4/H_2/Ar plasmas showed 95% of absorbed power being expended in the vibrational and rotational excitation of H_2. Plasma activation and plasma chemical kinetics involves a complex series of gas phase reactions. Previous publications have utilized over 240 direct and reverse reactions for 30 neutral species and 8 charged species.[23] Some examples of these reactions with their reaction rates are shown below. These are typical rates within the hot centre of a CH_4/H_2 plasma, with an input power, P =1.5 kW and pressure, p = 150 Torr.

Dissociation:	$CH_4 + e \rightarrow CH_3 + H + e$	R=8.04 x 10^{13} cm^{-3} s^{-1}	(1.1)
Ionisation	$C_2H_2 + e \rightarrow C_2H_2^+ + e + e$	R=1.09 x 10^{15} cm^{-3} s^{-1}	(1.2)
Recombination:	$C_2H_2^+ + e \rightarrow C_2H + H$	R=9.84 x 10^{14} cm^{-3} s^{-1}	(1.3)

Since the bulk of power absorption goes into exciting H_2, excited H_2 may then dissociate to form 'hot' H atoms, or undergo elastic reactions with other gas phase species. It is the collisions between gas phase species, which results in the overall distribution of excess energy resulting in the heating of the gas mixture. The surface kinetics involves the reaction of C_xH_y species, H_2 and H with the reactor base and walls, as well as the diamond surface.

The reactor is assumed to be cylindrically symmetrical (an approximation revisited later). The model itself consists of a 6 cm x 6cm 2D slice with axial and radial coordinates (z,r) constructed of 1 x 1mm squares between which species can migrate. Constructing the reactor volume like this allows for temperature gradients to be realized and local thermodynamic equilibria can be reached within each square. In the model, the plasma does not reach down to the surface, but does go as far as z=0.5 mm.

The work presented in this thesis aims to further the understanding of gas phase and surface chemistry for oxygen and nitrogen containing C/H plasmas. For this, gas phase diagnostics and 2D modelling provide information about the plasma, and computational modelling provides the energies of structures on a growing diamond surface. The theory behind these techniques is detailed in the following chapter.

1.6 References

1. Diamond and Diamond-Like Film Applications. 497 (CRC Press, 1998)

2. Plamann, K., Fournier, D., Anger, E. & Gicquel, A. Photothermal examination of the heat diffusion inhomogeneity in diamond films of sub-micron thickness. *Diam. Relat. Mater.* **3,** 752 (1994).

3. Graebner, J. E., Jin, S., Kammlott, G. W., Herb, J. A. & Gardinier, C. F. Large anisotropic thermal conductivity in synthetic diamond films. *Nature* **359,** 401 (1992).

4. Woerner, E., Wild, C., Mueller-Sebert, W. & Koidl, P. CVD-diamond optical lenses. *Diam. Relat. Mater.* **10,** 557 (2001).

5. Klein, C. A. Diamond windows for IR applications in adverse environments. *Diam. Relat. Mater.* **2,** 1024 (1993).

6. Endriz, J. G. *et al.*. High power diode laser arrays. *IEEE J. Quantum Electron.* **28,** 952 (1992).

7. Mollart, T. P. The development of CVD infrared optics from planar windows to missile domes. *AeroSense 2003* (Tustison, R. W.) 127 (International Society for Optics and Photonics, 2003).

8. Zapol, P., Sternberg, M., Curtiss, L., Frauenheim, T. & Gruen, D. Tight-binding molecular-dynamics simulation of impurities in ultrananocrystalline diamond grain boundaries. *Phys. Rev. B* **65,** 045403 (2001).

9. Sato, T. *et al.*. Transport of heavily boron-doped synthetic semiconductor diamond in the hopping regime. *Phys. Rev. B* **61,** 12970 (2000).

10. Collins, A. T. & Williams, A. W. S. The nature of the acceptor centre in semiconducting diamond. *J. Phys. C Solid State Phys.* **4,** 1789 (1971).

11. Klein, T. *et al.*. Metal-insulator transition and superconductivity in boron-doped diamond. *Phys. Rev. B* **75,** 165313 (2007).

12. Bustarret, E. *et al.*. Dependence of the Superconducting Transition Temperature on the Doping Level in Single-Crystalline Diamond Films. *Phys. Rev. Lett.* **93,** 237005 (2004).

13. Bustarret, E. *et al.*. Metal-to-insulator transition and superconductivity in boron-doped diamond. *Philos. Trans. A. Math. Phys. Eng. Sci.* **366,** 267 (2008).

14. Kajihara, S., Antonelli, A., Bernholc, J. & Car, R. Nitrogen and potential n-type dopants in diamond. *Phys. Rev. Lett.* **66,** 2010 (1991).

15. Achatz, P. *et al.*. Effect of nitrogen on the electronic properties of ultrananocrystalline diamond thin films grown on quartz and diamond substrates. *Phys. Rev. B* **74,** 155429 (2006).

16. Gicquel, A., Chenevier, M., Hassouni, K., Tserepi, A. & Dubus, M. Validation of actinometry for estimating relative hydrogen atom densities and electron energy evolution in plasma assisted diamond deposition reactors. *J. Appl. Phys.* **83,** 7504 (1998).

17. Yan, C. Very high growth rate chemical vapor deposition of single-crystal diamond. *Proc. Natl. Acad. Sci.* **99,** 12523 (2002).

18. Robertson, J. *et al.*. High rate homoepitaxial growth of diamond by microwave plasma CVD with nitrogen addition. *Diam. Relat. Mater.* **15,** 455 (2006).

19. Bénédic, F. *et al.*. Spectroscopic Diagnostics of Pulsed Microwave Plasmas used for Nanocrystalline Diamond Growth. *Chem. Vap. Depos.* **14,** 173 (2008).

20. Ma, J., Richley, J. C., Davies, D. R. W. & Ashfold, M. N. R. Spectroscopic and modelling investigations of the gas phase chemistry and composition in microwave plasma activated $B_2H_6/CH_4/Ar/H_2$ mixtures. *J. Phys. Chem. A* **114,** 10076 (2010).

21. Petherbridge, J., May, P. W. U., Pearce, S. R. J., Rosser, K. N. & Ashfold, M. N. R. Molecular beam mass spectrometry investigations of low temperature diamond growth using CO_2/CH_4 plasmas. **3,** 393 (2001).

22. Silva, F., Hassouni, K., Bonnin, X. & Gicquel, A. Microwave engineering of plasma-assisted CVD reactors for diamond deposition. *J. Phys. Condens. Matter* **21,** 364202 (2009).

23. Mankelevich, Y. A., Ashfold, M. N. R. & Ma, J. Plasma-chemical processes in microwave plasma-enhanced chemical vapor deposition reactors operating with C/H/Ar gas mixtures. *J. Appl. Phys.* **104,** 113304 (2008).

24. Hirmke, J. *et al.*. Improved flow conditions in diamond hot filament CVD—Promising deposition results and gas phase characterization by laser absorption spectroscopy. *Vacuum* **81,** 619 (2007).

25. May, P. W. & Mankelevich, Y. A. Experiment and modelling of the deposition of ultrananocrystalline diamond films using hot filament chemical vapor deposition and $Ar/CH_4/H_2$ gas mixtures: A generalized mechanism for ultrananocrystalline diamond growth. *J. Appl. Phys.* **100,** 024301 (2006).

26. Wei, Q. *et al.*. Diamond growth on WC-Co substrates by hot filament chemical vapor deposition: Effect of filament–substrate separation. *Diam. Relat. Mater.* **20,** 641 (2011).

27. Schwarz, S., Rosiwal, S. M., Frank, M., Breidt, D. & Singer, R. F. Dependence of the growth rate, quality, and morphology of diamond coatings on the

pressure during the CVD-process in an industrial hot-filament plant. *Diam. Relat. Mater.* **11,** 589 (2002).

28. Bachmann, P. K., Leers, D. & Lydtin, H. Towards a general concept of diamond chemical vapour deposition. *Diam. Relat. Mater.* **1,** 1 (1991).

29. Marinelli, M. *et al.*. Compositional and spectroscopic study of the growth of diamond films from several gaseous mixtures. *J. Appl. Phys.* **76,** 5702 (1994).

30. Gicquel, A., Hassouni, K., Silva, F. & Achard, J. CVD diamond films: from growth to applications. *Curr. Appl. Phys.* **1,** 479 (2001).

31. Ma, J., Richley, J. C., Ashfold, M. N. R. & Mankelevich, Y. A. Probing the plasma chemistry in a microwave reactor used for diamond chemical vapor deposition by cavity ring down spectroscopy. *J. Appl. Phys.* **104,** 103305 (2008).

32. Robertson, J. *et al.*. The role of inert gas in MW-enhanced plasmas for the deposition of nanocrystalline diamond thin films. *Diam. Relat. Mater.* **18,** 750 (2009).

33. Harris, S. J. Mechanism for diamond growth from methyl radicals. *Appl. Phys. Lett.* **56,** 2298 (1990).

34. May, P. W. & Mankelevich, Y. A. Experiment and modelling of the deposition of ultrananocrystalline diamond films using hot filament chemical vapor deposition and $Ar/CH_4/H_2$ gas mixtures: A generalized mechanism for ultrananocrystalline diamond growth. *J. Appl. Phys.* **100,** 024301 (2006).

35. May, P. W. & Mankelevich, Y. A. From Ultrananocrystalline Diamond to Single Crystal Diamond Growth in Hot Filament and Microwave Plasma-Enhanced CVD Reactors: a Unified Model for Growth Rates and Grain Sizes. *J. Phys. Chem. C* **112,** 12432 (2008).

36. Tallaire, A. *et al.*. Characterisation of high-quality thick single-crystal diamond grown by CVD with a low nitrogen addition. *Diam. Relat. Mater.* **15,** 1700 (2006).

37. Harris, S. J. & Martin, L. R. Methyl versus acetylene as diamond growth species. *J. Mater. Res.* **5,** 2313 (2011).

38. Ashfold, M. N. R. *et al.*. Unravelling aspects of the gas phase chemistry involved in diamond chemical vapour deposition. *Phys. Chem. Chem. Phys.* **3,** 3471 (2001).

39. Cheesman, A., Harvey, J. N. & Ashfold, M. N. R. Studies of carbon incorporation on the diamond [100] surface during chemical vapor deposition using density functional theory. *J. Phys. Chem. A* **112,** 11436 (2008).

40. Gruen, D. M., Liu, S., Krauss, A. R., Luo, J. & Pan, X. Fullerenes as precursors for diamond film growth without hydrogen or oxygen additions. *Appl. Phys. Lett.* **64,** 1502 (1994).

41. Zhou, D., McCauley, T. G., Qin, L. C., Krauss, a. R. & Gruen, D. M. Synthesis of nanocrystalline diamond thin films from an Ar–CH[sub 4] microwave plasma. *J. Appl. Phys.* **83,** 540 (1998).

42. Skokov, S., Weiner, B. & Frenklach, M. Chemistry of Acetylene on Diamond (100) Surfaces. *J. Phys.Chem* **1,** 8, (1995).

43. Skokov, S., Weiner, B. & Frenklach, M. Elementary reaction mechanism for growth of diamond (100) surfaces from methyl radicals. *J. Phys.Chemm*,**28**, 7073, (1994)

44. Butler, J. E., Woodin, R. L., Brown, L. M. & Fallon, P. Thin Film Diamond Growth Mechanisms [and Comment]. *Philos. Trans. R. Soc. A Math. Phys. Eng. Sci.* **342,** 209 (1993).

45. Butler, J. E. & Oleynik, I. A mechanism for crystal twinning in the growth of diamond by chemical vapour deposition. *Philos. Trans. A. Math. Phys. Eng. Sci.* **366,** 295, (2008).

46. Tsuda, M., Hata, M. & Oikawa, S. Adatom migrations and nucleations on reconstructed (001) surfaces II. Diamond. *Appl. Surf. Sci.* **107,** 116 (1996).

47. Larsson, K. & Carlsson, J.-O. Surface migration during diamond growth studied by molecular orbital calculations. *Phys. Rev. B* **59,** 8315 (1999).

48. Frenklach, M., Skokov, S., Park, U. V & Pennsyl, V. Surface Migration in Diamond Growth. **5647,** 3025 (1997).

49. Mankelevich, Y. A., Ashfold, M. N. R. & Orr-Ewing, A. J. Measurement and modelling of Ar/H_2/CH_4 arc jet discharge chemical vapor deposition reactors II: Modelling of the spatial dependence of expanded plasma parameters and species number densities. *J. Appl. Phys.* **102,** 063310 (2007).

Chapter 2 Theory and experimental concepts

This chapter outlines the theory behind experimental techniques and the interpretation of experimental and computational data. This begins with a discussion of the molecular spectroscopy involved in atomic and electronic transitions, followed by an introduction to the laser apparatus used and the interaction of light with matter, as well as diagnostic techniques. The chapter finishes by introducing the computational methods used for calculating the optimized geometries and energies of structures on a diamond surface.

2.1 Atomic and molecular spectra

2.1.1 The Schrodinger equation

The system within an atom or molecule can be described by it's wavefunction (Ψ), which is a function of temporal and spatial coordinates Ψ(x,y,z,t). The wavefunction of a system can be described by solving the Schrodinger equation. The Schrodinger equation is written as,

$$\hat{H}\Psi = E\Psi \tag{2.1}$$

where E is an eigenvalue, H is the Hamiltonian operator and Ψ is an eigenfunction. In order to solve the Schrodinger equation, the energy of the system is first defined in terms of classical quantities as the sum of potential and kinetic energies, and then re-defined in terms of linear momenta and position coordinates. The classical function is then transformed to give the Hamiltonian operator.[1]

The Hamiltonian operator represents both kinetic and potential energy, and in classical terms this can be represented as:

$$H = T + V \tag{2.2}$$

where T is the kinetic energy and V the potential energy. In quantum mechanical form, the Hamiltonian can be re-written as

$$\hat{H} = \frac{-\hbar^2}{2m}\left(\frac{\partial^2}{\partial x^2} + \frac{\partial^2}{\partial y^2} + \frac{\partial^2}{\partial z^2}\right)\Psi + V\Psi \quad (2.3)$$

Now replcing $\left(\frac{\partial^2}{\partial x^2} + \frac{\partial^2}{\partial y^2} + \frac{\partial^2}{\partial z^2}\right)$ with the laplacian ∇^2 (del squared), the Schrodinger equation can be written as:

$$\frac{-\hbar^2}{2m}\nabla^2\Psi + V\Psi = E\Psi \quad (2.4)$$

The above derivation explains the time-independent Schrodinger equation, which can be solved exactly to give energies in a one-electron system. When many electrons are present, it becomes more difficult due to repulsive interactions between electrons, and the Schrodinger equation cannot be solved exactly. When solving the Schrodinger equation for a many electron system, calculations use the Born-Oppenheimer approximation,[2] which treats the nuclei as being stationary with electrons moving around them. This means that the nuclear and electronic parts of the Schrodinger equation are treated separately.

$$\Psi_{tot} = \Psi_{elec} + \Psi_{nuc} \quad (2.5)$$

The total wavefunction can be split into electronic, rotational and vibrational wavefunctions:

$$\Psi_{tot} = \Psi_{elec} + \Psi_{rot} + \Psi_{vib} \quad (2.6)$$

2.1.2 Atomic spectra

The motion of an electron around the nucleus is seen as:

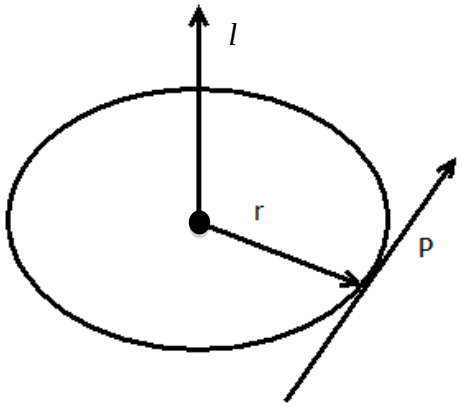

Fig. 2.1. The motion of an electron around the nucleus.[3]

where l is the angular momentum quantum number, P is the linear momentum and r is the radius.

The orbital angular momentum quantum number, l defines the motion of an electron around the nucleus and is quantized as:

$$l=0,1,2,3\ldots,(n\text{-}1) \tag{2.7}$$

and given the term symbols s,p,d,f…, representing different orbitals for a one electron system. The s-orbital has no angular momentum, as motion is purely radial.

Since l defines the motion around the nucleus, the magnetic quantum number m_l, or $|l_z|$describes the projection of l in the z-axis. The magnetic quantum number m_l can take values from:

$$m_l = 0, \pm1, \pm2, \ldots,\pm l \tag{2.8}$$

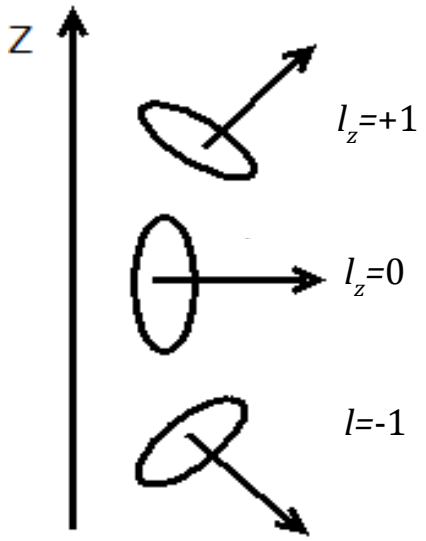

Fig. 2.2. The direction, $|lz|$of an electron orbital angular momentum vector with respect to a chosen z-axis.[3]

Orbital sketches show the angular dependence of the electron orbital, and the amplitude of Ψ, where Ψ^2 is the electron probability density.

The electron also possesses spin angular momentum, which is a vector $|s|$. The spin multiplicity S is given as,

$$S=(2S+1) \tag{2.9}$$

In a one electron system, when the electron possesses both orbital and spin angular momenta, the quantum number *j* represents the total angular momentum associated with orbital and spin angular momenta, where *j* can take the values,

$$j = l+s,\ l+s\text{-}1,\ldots,\ |l-s| \tag{2.10}$$

The term symbol is then written as ${}^{2S+1}l_J$.

The hydrogen atom is an example of an atom, which has only one electron. This means that for the H-atom, the Schrodinger equation can be solved exactly. Studying emissions from the hydrogen atom in the late 19th century led to recognition of the Lyman and Balmer series, and the Rydberg formula. The Rydberg formula is shown in 2.21, and describes the wavelength of spectral lines for, in this case, hydrogen.

$$\frac{1}{\lambda} = R_H\left(\frac{1}{n^2}-\frac{1}{n'^2}\right) \tag{2.11}$$

where, n=1,2,3.. and n'>n, R_H is the Rydberg constant, and λ is the wavelength. The Lyman series involves transitions to or from the n=1 level. The Balmer series involves transitions to or from the n=2 level. Both the Lyman and Balmer series are shown in fig. 2.3.

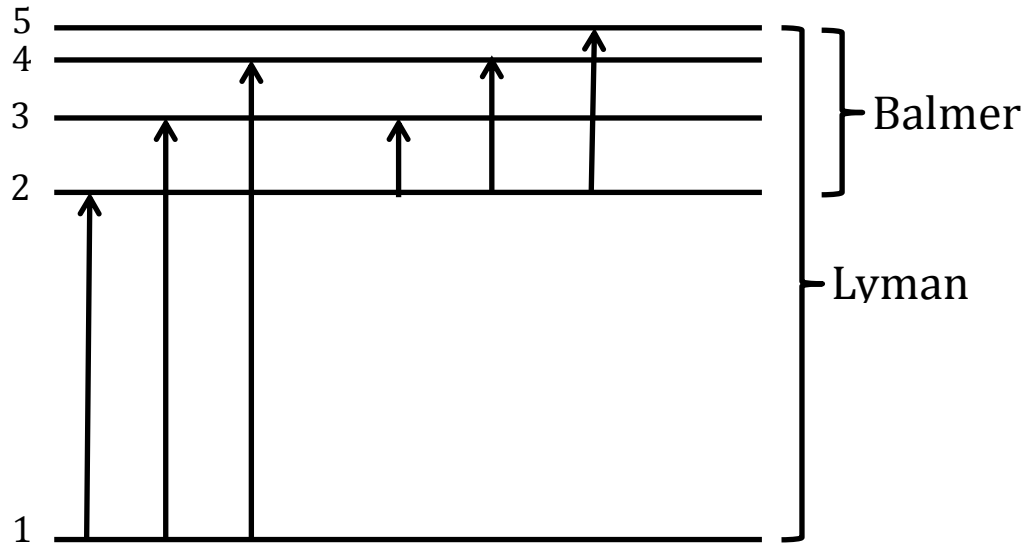

Fig 2.3. The H-atom energy levels, and transitions shown within the Lyman and Balmer series. Energy level values for *n* are given on the left hand side.

Transitions used in this thesis involve the Balmer series and, specifically, between the n=2 and n=3 levels, which is known as the Hα transition. There are seven very closely spaced allowed transitions associated with the Hα line, which are shown in fig. 2.4.

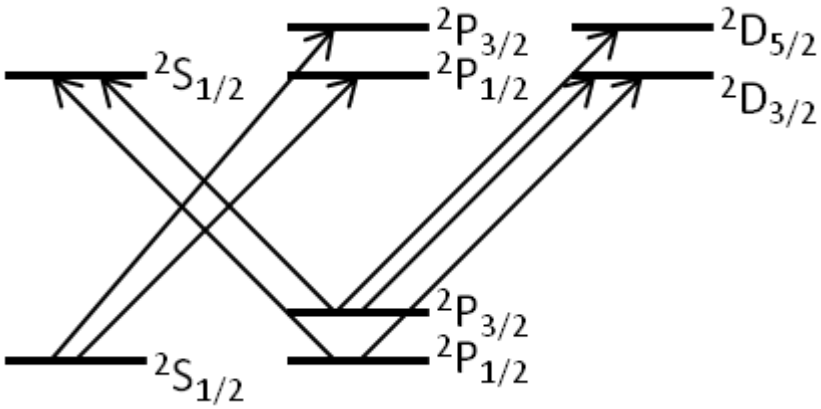

Fig 2.4. The allowed transitions for Hα.

When considering an atom which contains more than one electron, the coupling of spin and orbital angular momenta is important. In atoms other than hydrogen, the extent of coupling depends on the size of the atom. In heavy atoms for example, the coupling of spin momenta and the coupling of angular momenta is seen as too small to make a difference to the total angular momentum. The coupling between an electron and its own angular momentum to create ***j*** is, however seen as being strong, and the coupling between ***j***'s is noticeable. This type of coupling is called *jj*-coupling.[4]

A type of coupling in most light atoms is the opposite of *jj*-coupling; it represents the coupling of spin angular momenta, and the coupling of orbital angular momenta. This coupling is called Russell-Saunders coupling. When considering two orbiting electrons in an atom, the vectors of their angular momenta, *l*, couple to give *L*. This is called *ll* coupling, where *L* can take the values:

$$L = l_1+l_2,\ l_1+l_2\text{-}1,\ldots,\ |l_1 - l_2| \qquad (2.12)$$

These term symbols are labeled S,P,D,F… corresponding to L=0,1,2,3. M_L values for space quantization are equivalent for m_l, and are given as $M_L=L,L\text{-}1,\ldots,\text{-}L$.

The equivalent coupling for spin angular momenta is called *ss* coupling, and gives *S* where,

$$S = s_1+s_2,\ s_1+s_2\text{-}1, \ldots, |s_1 - s_2| \quad (2.13)$$

There is now coupling between orbital and spin angular momenta to consider. This spin orbit coupling is called LS coupling, and gives a total angular momentum vector *J*, which can take the values,

$$J = L+S,\ L+S\text{-}1, \ldots, |L - S| \quad (2.14)$$

The term symbol is then written as ${}^{2S+1}L_J$.

The selection rules which determine whether or not the promotion of an electron to an excited orbital in a 1 electron system will be allowed are

- Δn is unrestricted
- $\Delta l = \pm 1$ (2.15)

The selection rules, which govern the promotion of an electron to an excited state in an atom with more than 1 electron, are

$$\Delta L = 0, \pm 1 \quad (\text{except } L = 0 \leftrightarrow L = 0) \quad (2.16)$$

$$\Delta J = 0, \pm 1 \quad (\text{except } J = 0 \leftrightarrow J = 0) \quad (2.17)$$

$$\Delta S = 0 \quad (2.18)$$

2.1.3 Molecular spectra

The majority of spectroscopy in this thesis involves electronic transitions in diatomic molecules. Electronic spectroscopy involves a transition between two electronic levels, which is accompanied by changes in both vibrational, and rotational energy. In the classification of the electronic states for a diatomic molecule the same approach is used as in the Russell-Saunders approximation. This means that orbital and spin angular momenta of electrons are coupled to give quantum numbers Λ and Σ, in place of L and S. For a diatomic molecule, L is no longer a good quantum number, due to it

being so strongly coupled to the electrostatic field produced by the two nuclear charges. The allowed values of Λ, with corresponding labels are,

$$\Lambda = 0 \quad \Sigma \tag{2.19}$$

$$\Lambda = \pm 1 \quad \Pi \tag{2.20}$$

$$\Lambda = \pm 2 \quad \Delta \tag{2.21}$$

where the total is given as the sum of quantum number m_l, which corresponds to the axial orbital momentum of each electron.

$$\Lambda = |\sum m_l| \tag{2.22}$$

S is also no longer a good quantum number, due to it being coupled to the orbit of electrons around the inter-nuclear axis. For Σ, allowed values are

$$\Sigma = S, S - 1, \ldots, -S \tag{2.23}$$

The total spin, Σ is given as

$$\Sigma = \sum s \tag{2.24}$$

and as for atoms, the spin multiplicity is given as (2S+1). The third quantum number is Ω, which represents the total orbital plus spin angular momentum along the internuclear axis, where

$$\Omega = |\Lambda + \Sigma| \tag{2.25}$$

And so the term symbol becomes ${}^{2S+1}\Lambda_{\Omega}$.

There is also angular momentum of the rotating nuclear framework within the diatomic molecule to consider, R. The coupling of R with Ω gives the total angular momentum J as,

$$J = R + \Omega \tag{2.26}$$

Fig 2.5 shows all of the discussed quantum numbers with regards to the internuclear axis. There are, however additions which need to be made to molecular term symbols representing electronic states. One of these applies to Σ states, and involves the addition of a + or – sign to represent reflection in any σ_v plane containing the internuclear axis, where + represents the electronic configuration being symmetric on reflection, and – represents the electronic configuration being antisymmetric on reflection. The other involves the addition of 'g' or 'u' to the state labels of homonuclear diatomics. This is because only with two identical nuclei is there a centre of inversion, to which this rule applies, where 'g' represents the state wavefunction being symmetric on inversion and 'u' antisymmetric on inversion through the centre of the molecule.

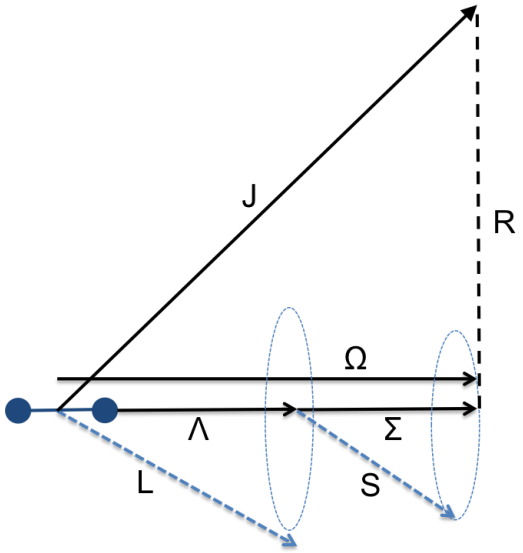

Fig. 2.5. Quantum numbers of angular momenta for a diatomic molecule. The arrows represent the direction of vectors. The circles around L and S represent the coupling of these vectors to the internuclear axis.

The selection rules for electronic transitions are as follows

$$\Delta\Lambda = 0, \pm 1 \tag{2.27}$$

$$\Delta\Omega = \pm 1 \tag{2.28}$$

$$\Sigma^+ \leftrightarrow \Sigma^+, \Sigma^- \leftrightarrow \Sigma^-, \Sigma^+ \not\leftrightarrow \Sigma^- \tag{2.29}$$

$$g \leftrightarrow u,\ g \not\leftrightarrow g, u \not\leftrightarrow u \tag{2.30}$$

The letter preceding the term symbol acts as a label, where X commonly represents the ground electronic state. Fig 2.5 shows all of the quantum numbers for an

electronic state, where J is the total angular momentum, R is the rotational angular momentum, and Λ and Σ are orbital and spin angular momenta.

Electronic transitions, however, are accompanied by vibrational and rotational transitions. Absorptions in pure-vibrational spectroscopy lie in the IR region, and pure-rotational transitions in the microwave region. With an electronic transition, the vibrational quantum number may change, and this is governed by the Franck-Condon principle. The Franck-Condon principle is based on the idea that an electronic transition occurs much faster than a vibrational motion, so that immediately after a vibronic transition, the nuclei are in the same position. This means that the transition between 2 electronic states, represented by potential energy curves as in fig. 2.6, will be vertical, i.e. *r* does not change during the transition. This may have the effect of promoting a molecule to a higher vibrational quantum level. This, however is dependent upon the equilibrium bond length, r_e, of the upper electronic state, as transitions may still occur between vibrational levels of the same quantum number. An example of vibronic transitions where there is (a) change and (b) no change in r_e is shown in fig. 2.6.

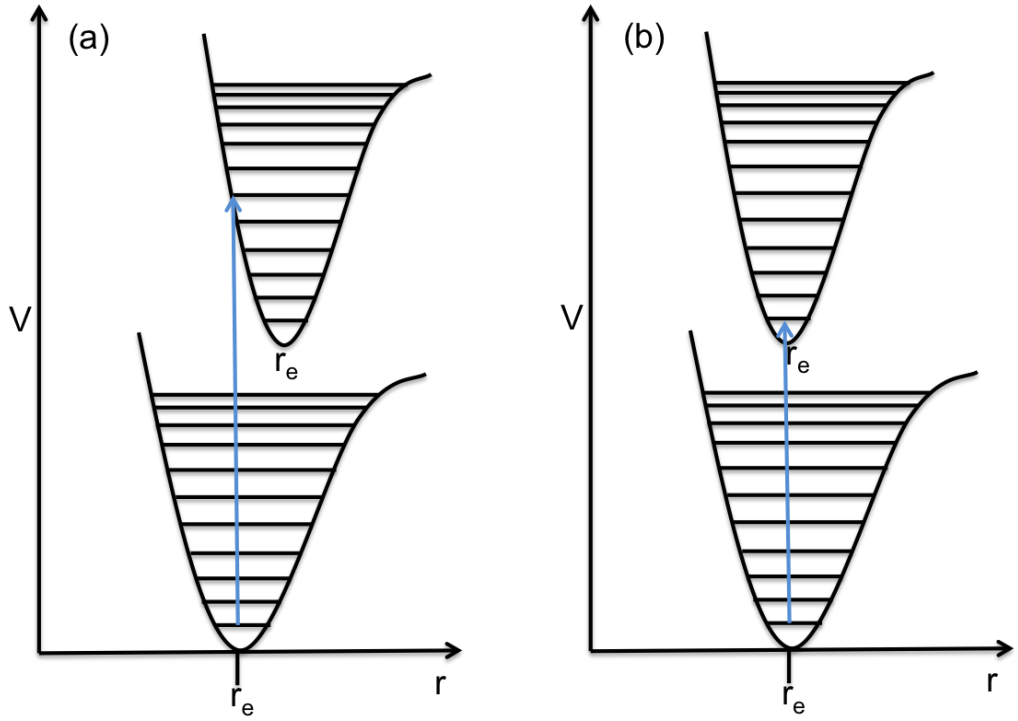

Fig. 2.6. Illustration of the Franck-Condon principle, where in (a) r_e(upper) > r_e(lower) and in (b) r_e(upper) = r_e(lower).

Fig. 2.6 also shows the nature of vibrations in a potential energy curve, in that the molecule behaves as an anharmonic oscillator. The anharmonic oscillator allows dissociation of the bond to occur with increasing bond length, *r*. The term values for an anharmonic oscillator are given as,

$$G(v) = \omega_e \left(v + \tfrac{1}{2}\right) - \omega_e x_e \left(v + \tfrac{1}{2}\right)^2 + \omega_e y_e \left(v + \tfrac{1}{2}\right)^3 \ldots \quad (2.31)$$

where ω_e is the frequency of the oscillator, and v the vibrational quantum number. The terms x_e and y_e are known as anharmonicity constants. These are required because the distance between adjacent vibrational levels decreases with increasing quantum number due to anharmonicity in the vibration.

As mentioned, vibronic transitions are accompanied by rotational transitions between the rotational levels in the lower and upper electronic states. The rotational term value for a given state is given as,

$$F(J) = BJ(J+1) - DJ^2(J+1)^2 \quad (2.32)$$

Where *B* is the rotational constant, *D* is the moment of inertia and *J* is the rotational quantum number. The rotational constant *B* is defined as,

$$B = \frac{h}{8\pi^2 cI} \text{ cm}^{-1} \quad (2.33)$$

where *I* is the moment of inertia, which is a measure of the resistance given by a rotating body to change in its angular velocity. The moment of inertia between two atoms m_1 and m_2 is seen as,

$$I = \mu r^2 \quad (2.34)$$

where μ is the reduced mass

$$\mu = \frac{m_1 m_2}{m_1 + m_2} \quad (2.35)$$

Rotational fine structure in vibronic transitions gives rise to P, Q and R branches, which correspond to the rotational selection rule,

$$\Delta J = 0, \pm 1 \tag{2.36}$$

where for P-branch transitions $\Delta J = -1$, for Q-branch transitions, $\Delta J = 0$ and for R-branch transitions, $\Delta J = +1$.

Collecting all of these contributions, the energy of a given rovibronic transition in a closed shell diatomic molecule would thus be given by

$$\Delta E = T_{oo} + G(v) + F'(J) - G''(v) - F''(J) \tag{2.37}$$

where ‘and “ contributions refer to respectively, the upper and lower states and T_{oo} is the energy separation between the potential minima of the combining electronic states.

2.1.4 Line intensity

Radiation can either be absorbed or emitted by matter, and in order for a spectroscopic transition to occur, the oscillating dipole of a molecule must be equal to the frequency of the radiation. The closer in energy these two oscillations are, the more likely there is to be a transition, where

$$h\nu = E_k - E_j \tag{2.37}$$

here, E_k and E_j represent the energies of the upper and lower levels involved in the transition, and $h\nu$ represents the energy of the radiation. The upper and lower levels may be rotational, vibrational, or electronic, but we will henceforth focus on electronic transitions.

The line intensity of a transition will be dependent upon the populations of the upper and lower levels. Whether the overall process involves absorption or emission will depend upon both the population and degeneracy of the two levels. A system at thermal equilibrium will obey the Boltzmann distribution, where

$$\frac{N_k}{N_j} = \frac{g_k}{g_j} exp^{\left(\frac{-\Delta E}{kT}\right)} \tag{2.38}$$

N_j and N_k represent the populations of lower and upper levels, and g_j and g_k represent the degeneracies of the lower and upper levels.

It is also important to consider the actual probability of transitions occurring, which involves Einstein coefficients. Einstein coefficients correspond to the absorption and emission of radiation, of which there are two emission processes; stimulated and spontaneous. A diagram showing the different processes for absorption and emission is shown in fig. 2.7,

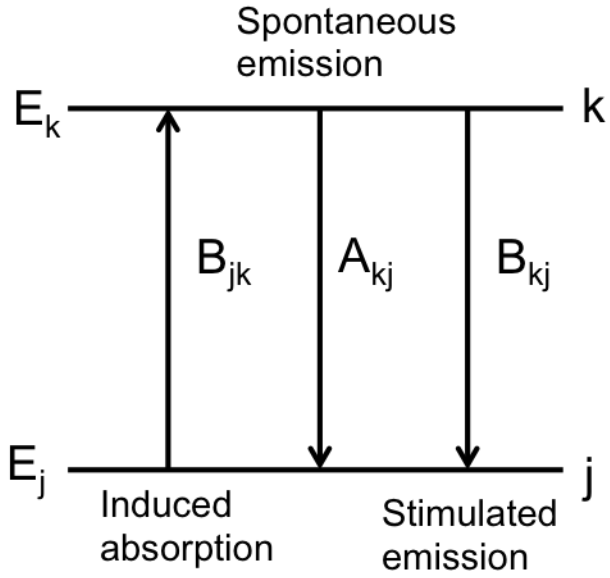

Fig. 2.7. Absorption and emission processes between upper and lower energy levels k and j showing Einstein coefficients for induced absorption, spontaneous and stimulated emission.

The Einstein B coefficient is used to represent absorption and stimulated emission due to the interaction of an atom or molecule with radiation. Induced absorption occurs when an atom or molecule absorbs a quantum of radiation, and is excited from lower level *j* to upper level, *k*. The intensity of this absorption is

$$I_{abs} = N_j h\nu B_{jk}\, \rho(\nu_{jk}) \tag{2.39}$$

where N_j is the population of the lower level, $h\nu$ is the energy difference and $\rho(\nu_{jk})$ is the radiation density at frequency ν, which is the energy stored per unit volume (J m^{-3}). Stimulated emission occurs when an electron is induced to move from a higher to a lower level, by radiation of an energy which matches that of the energy difference between the two levels, this adds to the intensity of the incident radiation, and is the fundamental process behind the workings of a laser. For stimulated emission, the Einstein B coefficient is also used

$$I_{em} = N_k h\nu B_{kj} \rho(\nu_{kj}) \tag{2.40}$$

Spontaneous emission depends upon the population of the excited state and the Einstein coefficient A, and is not dependent upon interaction with radiation. The intensity of spontaneous emission is given as

$$I_{em} = N_k h\nu A_{kj} \tag{2.41}$$

There will however, within a group of molecules, be both spontaneous and stimulated emission, and the combination of the two gives

$$I_{em} = N_k h\nu [A_{kj} + B_{kj}\, \rho(\nu_{jk})] \tag{2.42}$$

The relationship between the Einstein coefficients is given as

$$A_{kj} = 8\pi h\nu^3 B_{kj} \tag{2.43}$$

$$B_{jk} = \frac{g_k}{g_j} B_{kj} \tag{2.44}$$

The Einstein coefficients describe the probability of a transition occurring, however in absorption spectroscopy it is important to be able to describe the interaction of light

with the absorbing material. The Beer Lambert law describes the passing of light through a substance, as shown in fig. 2.8,

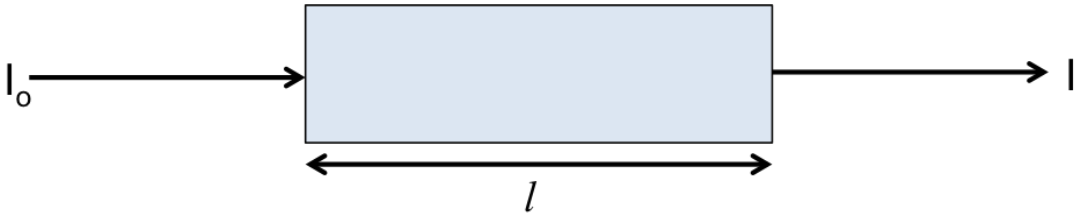

Fig. 2.8. Representation of an absorption experiment, where I_o and I represent the intensity of the radiation entering, and leaving an absorbing material of length l.

The intensity of light leaving the material is

$$I = I_o \, e^{-lc\varepsilon} \tag{2.45}$$

where l is the length of the absorber, c is the concentration and ε the molar absorption coefficient, which has units m^2/mol, and is a measure of how strongly a given species absorbs light at a given wavelength. The formula shows how absorption is dependent upon the concentration of the absorber and the length of the cell through which the radiation has to pass. With increasing concentration or cell-length, the intensity of the transmitted radiation decays exponentially.

Experimentally recorded data will contain lines, in absorption or emission, which are broadened. Because of the high temperatures reached in this work, the main broadening effect is Doppler broadening, and is a result of there being a slight change in the frequency at which an atom or molecule will absorb, dependent upon the velocity of the species travelling towards or away from the excitation source, in the case of laser absorption spectroscopy, or the detector in the case of emission spectroscopy. Doppler broadening is directly proportional to the gas temperature (T_{gas}) as shown below,

$$\Delta v = \frac{v}{c}\left(\frac{2kTln2}{m}\right)^{1/2} \tag{2.46}$$

where T is temperature, $\Delta\nu$ is the full width half maximum of the Doppler broadened lineshape, and m is the mass of the atom or molecule and ν is the transition frequency.

2.2 Experimental techniques

2.2.1 Lasers

The word laser is an acronym, which stands for 'light amplification by the stimulated emission of radiation'. As discussed, stimulated emission requires light of the correct frequency interacting with a system where the population of an excited, or upper state is greater than the ground, or lower state. When the population of the upper state is greater than the lower, this is known as population inversion, and is central to producing laser light. Population inversion is achieved by 'pumping' i.e. exciting a system, such as a solid material, with light in an optical cavity between two parallel mirrors. These mirrors are highly reflective, however one of them will allow 1-10% of the radiation to pass through, which creates the laser beam. Due to the parallel alignment of the mirrors, the beam produced has directionality, which means the beams of radiation produced are parallel with minimal spread or divergence over space. The might produced is also coherent, which means that the waves are propagating in phase.

In the optical cavity, creating an effective system with population inversion requires more than just a two-level system. This is because in a two level system at equilibrium, induced absorption will occur until the population of the upper level is equal to that in the lower, at which point induced emission will occur at the same rate as absorption, making a population inversion impossible to achieve. The use of a three or four-level system allows for creation of a population inversion. An example of a four-level system is shown in fig. 2.9, which shows the four energy levels involved. In this system, population is pumped to level 4, where fast relaxation occurs to level 3, creating a population inversion between levels 3 and 2. In this system population inversion is enhanced by the fast population depletion between levels 2 and 1.

Maintaining population inversion can be difficult, which is why pulsed lasers can be more effective, as this does not allow saturation to occur between the levels of the system.

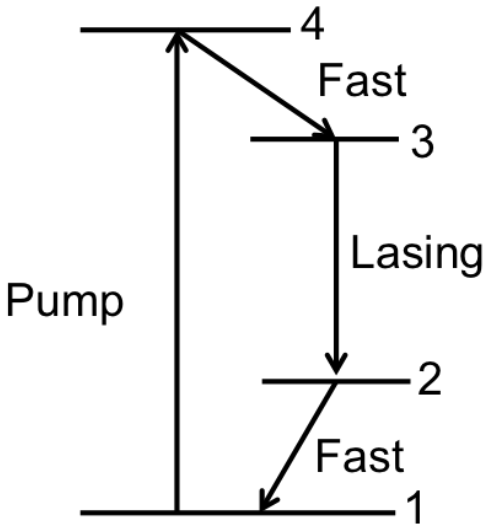

Fig. 2.9. A four-level laser system

Optical pumping involves a short intense pulse of light within the cavity, and uses a solid or liquid material (the "gain" medium) for producing the laser light.

To create even shorter, intense pulses, a mechanism called Q-switching can be applied. Q defines the quality factor of a cavity and can be described as

$$Q = \frac{v}{\Delta v} \tag{2.47}$$

where v is the frequency, and Δv is the laser line width. When Q is high, this means that there are low losses from the optical cavity, and when Q is low, there are high losses from the cavity. When decreasing Q, and allowing light to escape the cavity, has the effect of reducing the light within the cavity. When this happens, this allows a build up of population inversion in the upper state of the material since there is no light to induce the stimulated emission process. Lowering Q for a very short period of time, followed by increasing it rapidly results in the formation of a short, powerful laser pulse. These short pulses were historically called giant pulses. The shorter the pulse at a given energy, the higher the power achieved, as shown by

$$P_p = \frac{E_p}{\Delta t} \tag{2.48}$$

where P_p is the pulse power, E_p is the pulse energy and Δt is the pulse duration. Q switching has the ability to reduce the pulse length from 0.1-100 μs to 5-50 ns.

2.2.1.1 Nd-YAG laser

The Nd-YAG laser is one such pulsed four-level laser system. The laser producing material consists of Nd^{3+} ions embedded in a $Y_3Al_5O_{12}$ matrix. The four level system for the Nd-YAG laser is shown in fig. 2.10. The Nd-YAG rod is pumped with light from a monochromatic flashlamp eg. λ=806 nm, which excites population from the $^4I_{9/2}$ level to the $^4F_{5/2}$ level. This state then relaxes quickly to the $^4F_{3/2}$ level, in a non-radiative process. The $^4F_{3/2}$ level has a long lifetime, since the $^4F_{3/2} \rightarrow {}^4I_{11/2}$ transition is forbidden, which has the effect of enhancing population inversion. The laser producing process then comes from the movement of electrons from the $^4F_{3/2} \rightarrow {}^4I_{11/2}$ transition. The $^4F_{3/2} \rightarrow {}^4I_{13/2}$ transition also occurs, but this is weak in comparison.

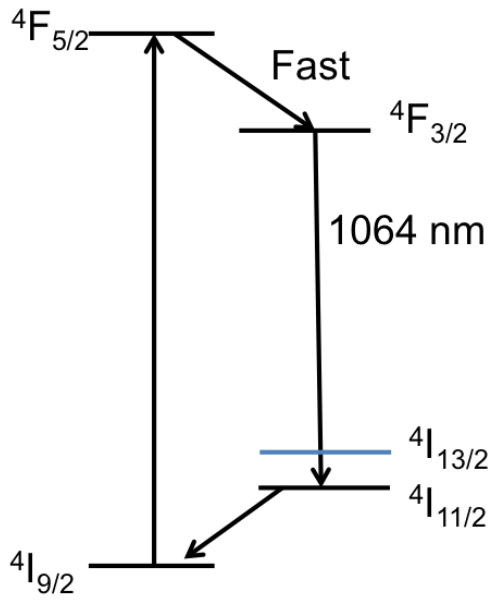

Fig. 2.10 Energy level diagram of the four-level system in a Nd-YAG laser.

The Nd-YAG fundamental wavelength 1064 nm is however, not particularly useful. As in most applications, the 2nd and 3rd harmonic output of the laser is used in this

thesis; 532 nm and 355 nm. To create these wavelengths the light is either frequency doubled or tripled, using a non-linear optical material.

2.2.1.2 Dye laser

Dye lasers produce laser light whilst being continuously tunable over a large wavelength range. They typically consist of an organic dye dissolved in a solvent, such as methanol. Each dye has a range of wavelengths over which it will radiate. An example of the transitions involved in the absorption of radiation, and production of laser light from a dye laser is shown in fig. 2.11.

The dye laser works in a similar style to a four-level laser. Dye molecules are pumped from the S_0 state, to the upper singlet states S_1 and S_2. This will result in upper vibrational and rotation levels being populated i.e. v>0. Each state in fig. 2.11 shows the upper vibrational levels as a continuum, since the dye is in a liquid, these states broaden due to interaction with solvent molecules and lose the vibrational spectroscopic structure as achieved in a gas. These highly excited states will decay into the lowest S_1 level. The $S_1(v=0) \rightarrow S_0(v>0)$ radiative process produces laser light and as written, this transition will also be to levels of v>0 in the S_0 state. If intersystem crossing (ISC) occurs between S_1 and T_1, this will reduce the population of S_1 and can have the effect of lowering the laser power. The $T_2 \leftarrow T_1$ transition then has the effect of reducing the reverse ISC, $T_1 \rightarrow S_0$, which would also reduce the power of radiation produced by the laser. For this reason, pulses of light produce the optimum output from dye lasers, because this greatly reduces the chances of T_1 interacting with the incident beam.

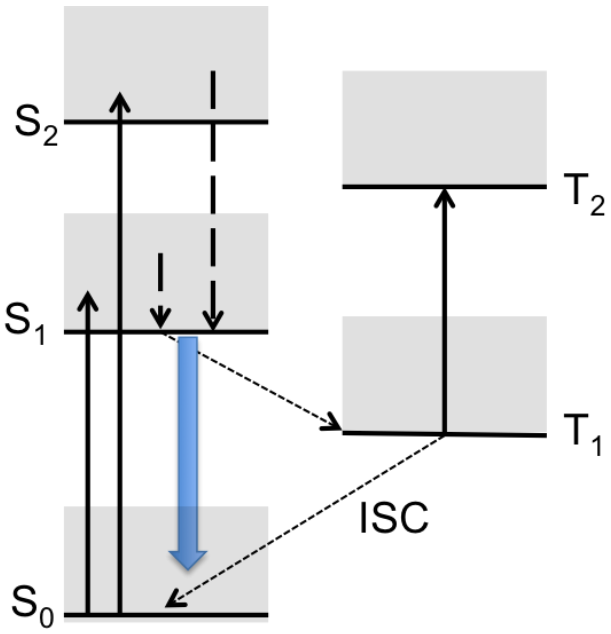

Fig 2.11. Energy level diagram of a dye laser. S represents singlet states, and T represents triplet states. ISC = intersystem crossing.

2.2.2 Optical emission spectroscopy

Optical emission spectroscopy (OES) measures emissions from excited atoms or molecules. This is a qualitative technique and is valuable for giving initial insight into which species are present in a plasma from their emissions. However, species emission is dependent upon the concentration of species in their excited states, and is therefore a convolution of the concentration and distribution of ground state species, and the source for their excitation i.e. electrons in a plasma. For this reason, trends gained using OES should be used in conjunction with a quantitative technique, such as absorption spectroscopy. In OES, light is usually collected from the emitting source, and directed onto a diffraction grating, which separates the light into its constituent wavelengths. The light is usually then passed onto a detector such as a charged couple detector (CCD), and can then be converted into an emission spectrum.

2.2.3 Absorption spectroscopy

Absorption spectroscopy is a spectroscopic technique, which involves the interaction of radiation with atoms or molecules in a gas, liquid or solid. These species are

generally in their ground states and, on absorption, are promoted to a higher state. In a general spectroscopic experiment, radiation entering the cell containing the material under investigation decreases in intensity as a result of being absorbed. This change in intensity is measured as the light leaves the cell and hits a detector. Absorption spectroscopy is a quantitative technique.

2.2.3.1 Cavity ring-down spectroscopy

Cavity ring-down spectroscopy (CRDS) is an ultra-sensitive laser absorption technique, which can be used to detect gas phase species, which are low in concentration. Unlike other absorption techniques CRDS is insensitive to fluctuations in the incident light intensity. One of the requirements of CRDS is that the species being measured absorbs the laser radiation. The experiment also requires two highly reflective mirrors, and a detector, as in fig. 2.12. The presence of the two mirrors allows the light to make thousands of round trips through the cavity. A detector sits behind one of the mirrors. This collects light as it passes through the mirror, since the mirror is not 100% reflective. This then allows the decay of each light pulse within the cavity to be measured as a function of time, which gives a decay rate, or ring-down time (RDT). A typical RDT is usually of the order of micro-seconds.

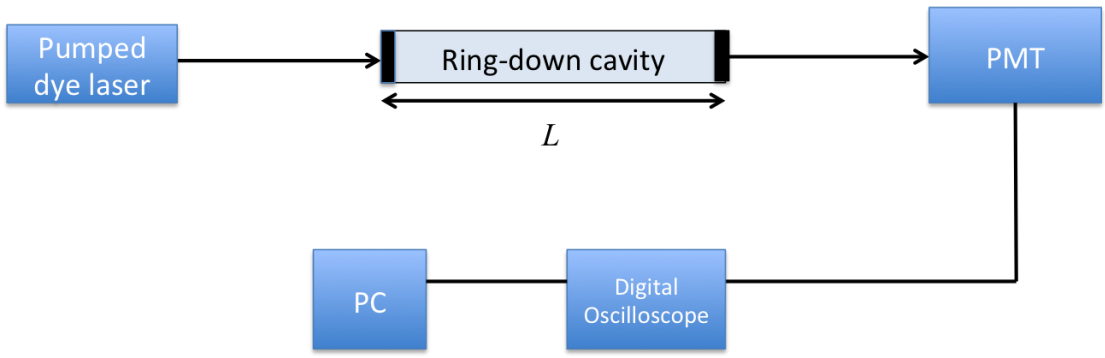

Fig 2.12. Example schematic for CRDS showing: Nd-YAG pumped dye laser, photomultiplier tube (PMT), the ring-down cavity with mirrors at both ends, and digital oscilloscope/PC for recording data.

The photomultiplier tube (PMT) used as a detector collects light from the laser pulse on each round trip it makes within the cavity. The time duration of each pulse used experimentally in this thesis is around 10 ns. If the light detected at each round trip is

given as an intensity spike, the decay of light within the cavity is exponential, as can be seen in fig. 2.13. The smooth line which follows the top of each spike provides a more realistic trace of the decay rate, since the time delay of the PMT is usually not sensitive enough to measure each spike. However, one cavity round trip takes ~6 ns, so with a pulse duration of ~10 ns, each pulse is ≥ one round trip. Reducing the pulse duration would therefore give the spikes shown in fig. 2.13.

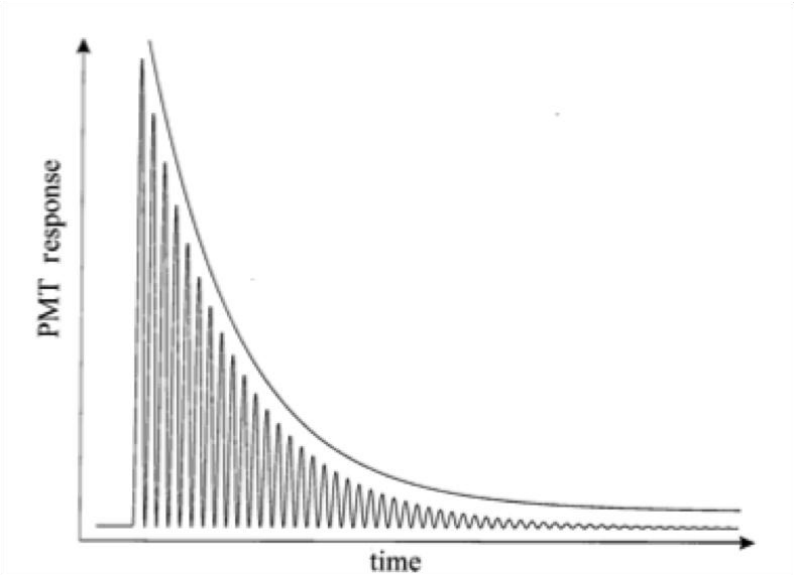

Fig 2.13 Schematic diagram of the response of a PMT to the light exiting the cavity mirror positioned in front of the detector.

2.2.4 Raman spectroscopy

The concept of Raman spectroscopy is slightly different to that for laser absorption spectroscopy. A sample is irradiated with highly monochromatic light, and the scattered radiation is then detected. The interaction of the incident radiation with vibrations in the solid can result in a change in the wavenumber of scattered radiation, if it either gains or loses energy. The energy of most of the scattered radiation is unchanged, and this radiation is referred to Rayleigh scattering. If the scattered radiation decreases in energy, this is called a Stokes Raman transition, and if the energy increases relative to the incident radiation, this is referred to as an anti-Stokes Raman transition. Rayleigh, Stokes and anti-stokes Raman scattering can be seen in fig. 2.14, which shows the absorption of radiation between actual and virtual vibrational states.

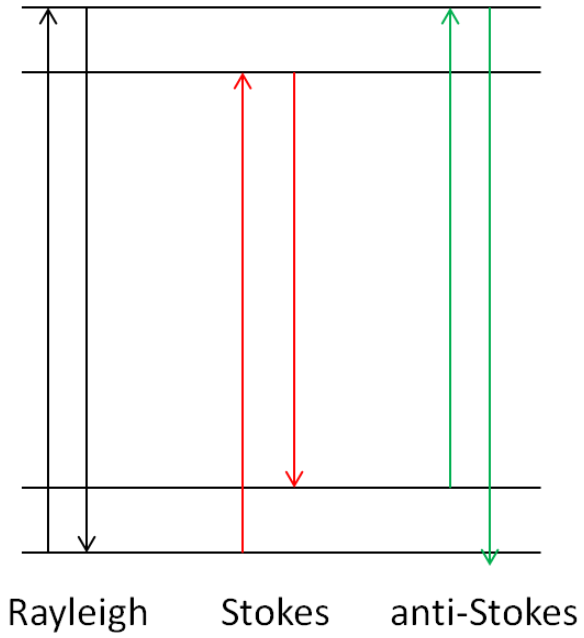

Fig. 2.14. Vibrational Raman scattering

In order to observe a vibrational Raman effect, there must be a change in polarizability with the vibrational displacement of a molecule. Polarizability, α, defines the intensity of scattering and is a measure of the degree to which the electron density can be displaced relative to the nuclei.

2.2.5 Scanning electron microscopy

Scanning electron microscopy (SEM) is a technique, which involves firing a beam of electrons at a surface, to give an image. The magnification of the sample is dependent on the size of the produced electron beam. When the electron beam is fired at the sample, inelastic collisions of electrons with the top atomic layers of the surface excite the sample, releasing secondary electrons. These electrons are detected with a secondary electron detector. SEM can produce resolution of better than 1 nm.[5]

2.3 Computational chemistry

Computational chemistry is the theoretical study of chemical reactions by use of a computer. Through calculations, which will be discussed, the course of a chemical

reaction can be followed in terms of bond lengths and angles between constituent nuclei in a potential energy surface (PES). The PES is defined by the potential energy for all possible atomic arrangements available to a collection of atoms involved in a reaction. The reaction coordinate displays the lowest energy pathway of a reaction. Fig 2.15 shows an example of a reaction coordinate,

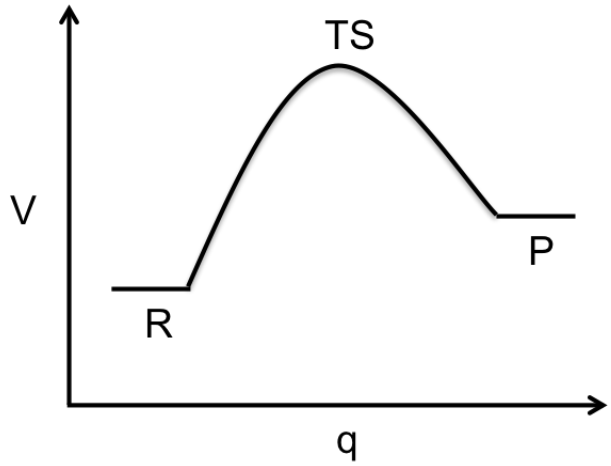

Fig. 2.15. Typical example of a reaction coordinate, where V is energy and q is the reaction coordinate. R, P and TS stand for reactants, products and transition state.

On a reaction coordinate, global minima are reached when bond lengths and angles have been optimized, so that the energy of a structure is at its lowest possible value. Reactants (R) and products (P) in fig. 2.15 are seen as stationary points, which are flat relative to the horizontal axis. Stationary points are reached when the first derivative of the energy with respect to the reaction coordinate is equal to zero, as shown below[6],

$$\frac{\partial E}{\partial q_i} = \frac{\partial E}{\partial q_2} = 0 \tag{2.49}$$

where q_1 and q_2 represent bond lengths and angles. The transition state (TS) for a reaction is also shown in fig. 2.15. TS's are seen as saddle points; energy is maximum along the reaction coordinate, but minimum in all other directions.

2.3.1 Molecular mechanics

Molecular mechanics (MM) treats atoms as balls, and the bonds holding them together in molecules as springs. MM uses classical mechanics to study the variation

of the energy in molecules with varying geometry. MM differs from quantum mechanics (QM) because it utilizes the Born-Oppenheimer approximation and treats atoms only as nuclei, making no reference to electrons and therefore electronic properties such as bond strengths cannot be calculated. MM calculations are faster than QM calculations, and useful for calculating geometries of large molecules. MM methods use force fields, which have 2 main components:

- Equations, which are used to show the effect the positions of atoms in a molecule have on potential energy.
- MM uses atom types to define elements dependent upon their chemical surroundings/environment e.g. CO is treated differently to a CH group.

The potential energy of a molecule can be written as:

$$E = \sum_{bond} E_{stretch} + \sum_{angle} E_{bend} + \sum_{dihedrals} E_{torsion} + \sum_{pairs} E_{non-bond} \tag{2.50}$$

From (2.50), the potential energy for bond stretching can be written as,

$$E_{stretch} = \frac{1}{2} k_{AB} (r_{AB} - r_{AB,eq})^2 \tag{2.51}$$

where k is the force constant between atoms A and B. The Morse function better describes anharmonic oscillation, but this is unsuitable computationally for these types of calculation. One problem with the approach in (2.51) is that at large r_{AB} the potential energy becomes infinitely positive, which is not chemically accurate, since dissociation should occur and the force constant should become 0. The addition of higher terms from the Taylor series, cubic and quartic, compensates for this problem.

The potential energy for angle bending can also be written as,

$$E_{angle} = \frac{1}{2} k_{ABC} (\theta_{ABC} - \theta_{ABC,eq})^2 \tag{2.52}$$

where the force constant is now written as k_{ABC}, since any change in angle will be dependent upon more than 2 atoms, and θ is the bond angle between bonds AB and BC.

The energy of torsion needed to rotate about the bond AB-CD is known as the torsional energy. Torsional energies are important only for single bonds, since double and triple bonds are too rigid. Torsional energies can be calculated as

$$E_{Torsion} = \sum_{r=1}^{n} \frac{1}{2} k_{tor}[1 + \cos(r\Phi)] \qquad (2.53)$$

where the angle Φ is the dihedral angle about the bond and k_{tor} is the torsional constant dependent upon the rotational barrier i.e $k_{tor}1$, k_{tor} 2 and k_{tor} 3 will be the torsional constants for one-fold, two-fold and three-fold rotational barriers. An example of a 3-fold rotational barrier for ethane is shown in fig. 2.16.

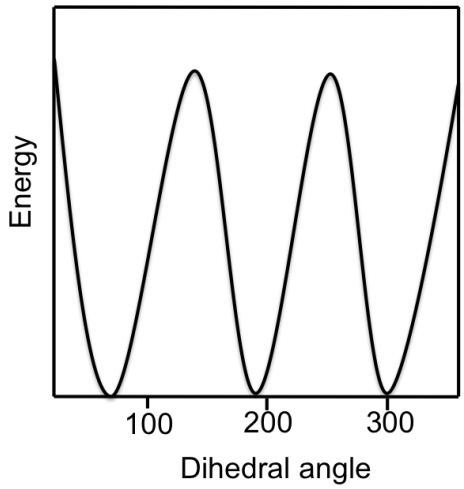

Fig. 2.16. An example of a 3-fold rotational barrier, to show how the energy varies with bond angle in a cosine pattern.

The combination of bond stretching, bending and torsional energies gives a good representation of the variations in potential energy experienced by bonding atoms in a molecule. However, an additional energy which has to be taken into consideration is that of non-bonding atoms. An example of the non-bonding energy between two atoms in an A-X-Y-B system would be between A and B The force between these two atoms is Van der Waals, and accounts for steric interactions. A potential energy surface for this interaction is shown in fig. 2.17.

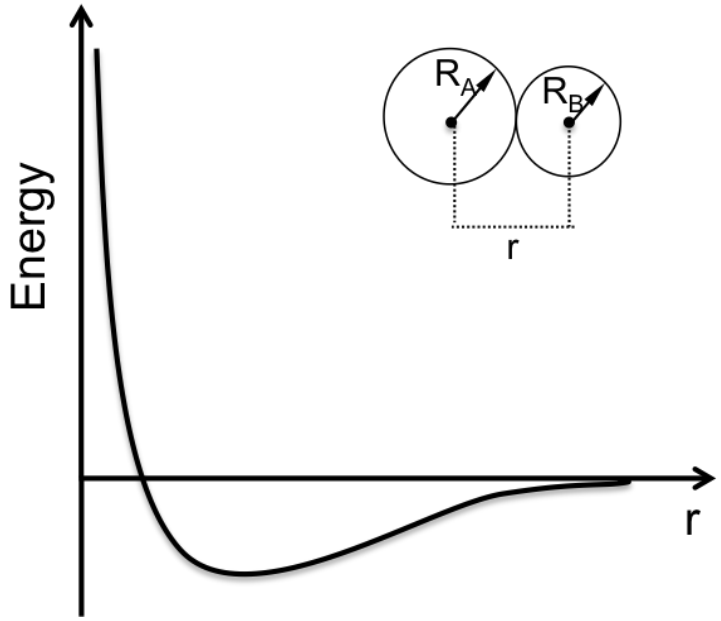

Fig 2.17. Shows the potential energy curve for the Van der Waals force contribution in a non-bonding interaction. The 2 circles represent the circumference of the Van der Waals forces, and R_A and R_B represent the radius from the nucleus to the circumference.

In fig. 2.17, the shallow dip represents the ideal interatomic distance between atoms A and B, and the steep rise in potential energy that arises when the Van der Waal radii are pushed too close together. The potential energy curve is approximated using the Lennard-Jones 12-6 potential, which is written as,

$$E_{non-bond} = \varepsilon \left[\left(\frac{r_m}{r} \right)^{12} - \left(\frac{r_m}{r} \right)^{6} \right] \tag{2.54}$$

where r is the distance between the two nuclei, ε is the depth of the well and r_m is the value of r when the potential energy is lowest. The 12^{th} and 6^{th} powers represent short range repulsive and long range attractive terms.

The above equations which are included in MM calculations are useful, but do not include any electrons, so the results cannot be used to give any insight into orbital shapes or bond strengths.[6]

2.3.2 Density Functional Theory

Density functional theory (DFT) is a technique which uses electron density functionals to investigate the electronic structure of molecules. The basis of DFT calculations treats the electron density as having only three spatial coordinates, *x,y* and *z.* This makes DFT calculations much faster than ab-initio calculations such as Hartree-Fock[7], which take each electron into consideration, where a single electron has 4 coordinates; 3 spatial and 1 spin. Early research by Thomas[8] and Fermi[9] (TF) provided the first DFT methods. The TF model treats the nucleus as a positive potential in a uniform, non-interacting electron gas.

Modern DFT is based on the Kohn-Sham[10] approach. The Kohn-Sham approach, however, was based on two Hohenberg-Kohn theorems.[11] The first theorem states that all of the properties of a molecule in its ground state can be determined by the ground state electron density functional $\rho(x,y,z)$ or $\rho(\boldsymbol{r})$. This means that the ground state energy E_0 could be calculated if the ground state electron density is known. The second Hohenberg-Kohn theorem states that any trial electron density function will give an energy higher than or equal to the true electron density function of a molecule. In these trial functions, the electronic energy calculated is the movement of electrons under a potential imposed by atomic nuclei. When concentrating on electrons, the nuclei are seen as being external in line with the Born-Oppenheimer approximation. The nuclear potential is $v(\mathbf{r})$, and the electronic energy of a trial electron density becomes,

$$E_v[\rho_t] \geq E_0[\rho_0] \tag{2.55}$$

where E_v and E_0 are the electronic and ground state energies, and ρ_t and ρ_0 are the trial and ground state electron density functionals. The energy is calculated as a functional of these functions. The trial electron density must also satisfy the condition,

$$\int \rho_t(\boldsymbol{r}) d\boldsymbol{r} = n \tag{2.56}$$

which means that the integrated electron density in all directions must be equal to the total number of electrons 'n' in the molecule. The one drawback of DFT however, is

that exact functionals for obtaining ground state energies are unknown, and so approximate functionals are used.

The Kohn-Sham equations treat the energy of a molecule as a sum of terms. The basis of these terms originated from the Thomas-Fermi (TF) model.

$$E_0 = T[\rho] + V_{Ne}[\rho] + V_{ee}[\rho] \tag{2.57}$$

where *T* is the kinetic energy of the electron density, V_{Ne} is the attraction between the nucleus and electrons and V_{ee} is the repulsive potential between two electrons. The attraction between electrons and the nucleus can be written as,[12]

$$V_{Ne}[\rho] = \sum_a \frac{Z_a \rho(\boldsymbol{r})}{|\boldsymbol{R_a} - \boldsymbol{r}|} d\boldsymbol{r} \tag{2.58}$$

which shows the integral of the electron density multiplied by the external potential imposed by nucleus *a*, which is dependent upon the distance of nucleus (R_a) from the electron cloud *r*.
The V_{ee} energy can be expressed as,

$$V_{ee}[\rho] = \frac{1}{2} \iint \frac{\rho(\boldsymbol{r})\rho(\boldsymbol{r'})}{|r - r'|} d\boldsymbol{r} d\boldsymbol{r'} \tag{2.59}$$

which shows the integrated interaction of two separate clouds of electron density. The factor of 1/2 allows the integration to run over all space for both **r** and **r**'.

The first term in (2.57) is the kinetic energy for a system of non-interacting electrons. To improve on the accuracy of this, Kohn and Sham introduced orbitals, and split the kinetic energy into two parts, one which can be calculated exactly, and a small correction term. The kinetic energy is calculated exactly for a non-interacting system where the solution to the Schrodinger equation is given as a Slater determinant composed of the molecular orbitals of a reference system ψ_r, as[12]

$$T_S = \sum_{i=1}^{N} \left\langle \psi_r \middle| -\frac{1}{2}\nabla^2 \middle| \psi_r \right\rangle \tag{2.60}$$

where subscript ‘s’ represents that the kinetic energy has been calculated using a Slater determinant. An example of a Slater determinant for ψ_r in a 4-electron system is,

$$\psi_r = \frac{1}{\sqrt{4!}}\begin{vmatrix} \psi_1(1)\alpha(1) & \psi_1(1)\beta(1) & \psi_2(1)\alpha(1) & \psi_2(1)\beta(1) \\ \psi_1(2)\alpha(2) & \psi_1(2)\beta(2) & \psi_2(2)\alpha(2) & \psi_2(2)\beta(2) \\ \psi_1(3)\alpha(3) & \psi_1(3)\beta(3) & \psi_2(3)\alpha(3) & \psi_2(3)\beta(3) \\ \psi_1(4)\alpha(4) & \psi_1(4)\beta(4) & \psi_2(4)\alpha(4) & \psi_2(4)\beta(4) \end{vmatrix} \tag{2.61}$$

where in the first row, there are Kohn-Sham orbitals ψ_1 and ψ_2. Each spatial orbital is comprised of spin functions α and β allowing each electron to have $\pm\frac{1}{2}$. This gives an antisymmetrized orbital of each spin. However, in a system where electrons are interacting with one another, the kinetic energy cannot be solved exactly, and an exchange-correlation term $E_{XC}[\rho]$ must be included to give,

$$E = T[\rho_0] + V_{Ne}[\rho_0] + V_{ee}[\rho_0] + E_{XC}[\rho] \tag{2.62}$$

This Kohn-Sham equation now gives an estimation of the energy of a molecule based on calculating the exact kinetic energy of a non-interacting electron cloud, with an exchange correlation term to account for the very small fraction of the energy which comes from interactions between electrons. In calculations, however, there are different levels of Kohn-Sham DFT which have various methods for calculating the exchange-correlation energy (a functional of the electron density function). In these calculations, some initial approximation is given for the E_{XC} energy, and the KS equations start with some initial guess to the electron density, which is minimized. The Local Density Approximation[10] (LDA) treats local electron density as a uniform electron gas when approximating E_{XC}. The term local only means an infinitesimally small region around a point in the molecule. Local Spin Density Approximation (LSDA) is almost the same, except it takes electron spin into account, which makes calculations for open-shell molecules more accurate. The Generalized Gradient Approximation (GGA) is a method which includes both the electron density and its gradient in functionals for calculating the exchange-correlation energy. These take the first derivative of density at a given point within the molecule, which gives a better representation of the electron density distribution.

2.3.3 QM/MM calculations

QM/MM techniques are used as they provide the means to calculate the energy of a small molecular area by QM, which is embedded in a larger molecular network. The energy of the large area surrounding the QM region is calculated using MM. This provides a more realistic approximation of the QM region, as the MM region prevents it from optimizing to any unphysical geometry.

QM/MM was first developed to study enzymes in catalytic systems,[13] however since then, and do date, QM/MM papers share a common methodology

$$H = H_{QM} + H_{MM} + H_{QM/MM} \tag{2.63}$$

where the Hamiltonian is the QM Hamiltonian, the MM forcefield, and a Hamiltonian to describe the interactions between QM and MM regions. The total energy of the system can also be split into three parts,

$$E = E_{QM} + E_{MM} + E_{QM/MM} \tag{2.64}$$

The energy of the QM system is usually calculated by DFT or Hartree-Fock. The QM and MM regions have to connect in some way. The interface between the two regions involves covalent bonds. An example of how to create the interface, is via the link-atom approach.[14] In this approach, H atoms are placed at the peripheral atoms of the QM regions to accommodate valence electrons. This approach is used in the few QM/MM calculations described in Chapter 6.

2.4 References

1. Brown, J. M. *Molecular Spectroscopy (Oxford Chemistry Primers)*. 96 (Oxford University Press, USA, 1998).

2. Born, M. & Oppenheimer, R. Zur Quantemtheorie der Molekeln. *Ann. Phys.* **389,** 457–484 (1927).

3. Orchard, A. F. *Magnetochemistry: 75 (Oxford Chemistry Primers)*. 180 (OUP Oxford, 2003)

4. Hollas, J. M. *Modern Spectroscopy (Google eBook)*. 480 (John Wiley & Sons, 2004)

5. Hayat, M. A. Principles and techniques of scanning electron microscopy. Biological applications. Volume 1. (1974)

6. Lewars, E. G. *Computational Chemistry: Introduction to the Theory and Applications of Molecular and Quantum Mechanics*. 600 (Springer, 2011)

7. Slater, J. A Simplification of the Hartree-Fock Method. *Phys. Rev.* **81,** 385–390 1951).

8. Thomas, L. H. The calculation of atomic fields. *Math. Proc. Cambridge Philos. Soc.* **23,** 542 (2008).

9. Fermi, E. Eine statistische Methode zur Bestimmung einiger Eigenschaften des Atoms und ihre Anwendung auf die Theorie des periodischen Systems der Elemente. *Zeitschrift fur Phys.* **48,** 73(1928).

10. Kohn, W. & Sham, L. J. Self-Consistent Equations Including Exchange and Correlation Effects. *Phys. Rev.* **140,** A1133 (1965).

11. Hohenberg, P. Inhomogeneous Electron Gas. *Phys. Rev.* **136,** B864–B871 (1964).

12. Jensen, F. *Introduction to Computational Chemistry: Second Edition*. 620 (Wiley-Blackwell, 2006).

13. Warshel, A. & Levitt, M. Theoretical studies of enzymic reactions: Dielectric, electrostatic and steric stabilization of the carbonium ion in the reaction of lysozyme. *J. Mol. Biol.* **103,** 227 (1976).

14. Singh, U. C. & Kollman, P. A. A combined ab- initio quantum mechanical and molecular mechanical method for carrying out simulations on complex molecular systems: Applications to the CH_3Cl + Cl exchange reaction and gas phase protonation of polyethers. *J. Comput. Chem.* **7,** 718 (1986).

Chapter 3 CRDS and growth investigations of C/H/O plasmas

3.1 Introduction: C/H/O plasmas for diamond growth

In the standard growth model for CVD diamond, the main species responsible for growth is the CH_3 radical.[1] Activation of the conventional CH_4/H_2 gas mixture ultimately leads to the formation of high concentrations of CH_3 radicals in the vicinity of the growing diamond surface. Unconventional feed gas mixtures have been investigated in an attempt to optimise growth conditions. Early studies of C/H/O plasmas indicated that diamond could be grown at lower temperature, and the presence of O containing species in the plasma decreased graphitic carbon impurities on the diamond surface.[2–4] Some C/H/O plasmas used a $CH_4/H_2/H_2O$ gas mixture and found that the addition of H_2O into the gas mixture allowed films to be grown at a higher growth rate than with the conventional CH_4/H_2 mixture.[5] Other groups followed with studies incorporating CO_2, CO, O_2 as the oxygen and carbon source.[6,7] It will be shown in this chapter, however that diamond growth is dependent upon the source gas used in the MW reactor used for these experiments, and a balance between C/H/O must be reached to optimize diamond growth conditions.

Interest in C/H/O containing plasmas began in the early 1990's. As noted in the introduction, one of the most recognized studies of that period was by Bachmann *et al.*.[6,8] They created a C/H/O phase diagram depicting the window for successful diamond growth and proposed that the quality of diamond grown is independent of the starting materials, and only dependent on the ratio of C, H and O in the feed gas mixture. The group used around 80 different growth results varying the C/H/O ratio to construct the diagram, some of which were taken from literature at the time and some which were results from his own group. This allowed Bachmann *et al.* to explore the quality of subsequent diamond grown, if any, and create his phase diagram. Shown in fig 3.1 is the original diagram proposed. The H-O axis is defined in the diagram in terms of the elemental mole fraction of oxygen, $X_{O/\Sigma}$=O/(O+H), i.e. H_2O sits 1/3 along the axis when moving from the H vertex towards O. The O-C axis is defined in terms

of the elemental mole fraction of carbon, $X_{C/\Sigma}$=C/(C+O) i.e. CO sits 1/2 way up the axis. Keeping with the same structure, the C-H axis is defined in terms of $X_{H/\Sigma}$=H(H+C). When moving from C towards H, CH_4 sits 1/5 away from the H vertex.

An unclear area of the diagram is where the diamond growth domain meets the C-O tie line. Bachmann concludes that growth with a pure CO mixture is unlikely, yet he still expands the growth domain to its widest on the CO line. Following the publication of this paper, several groups made modifications to the diagram based on their own results and theories, most of which argue about the size of the diamond growth domain, especially at the intersection with the C-O line.[9–11] A more current version of greater accuracy is shown in fig. 3.2.

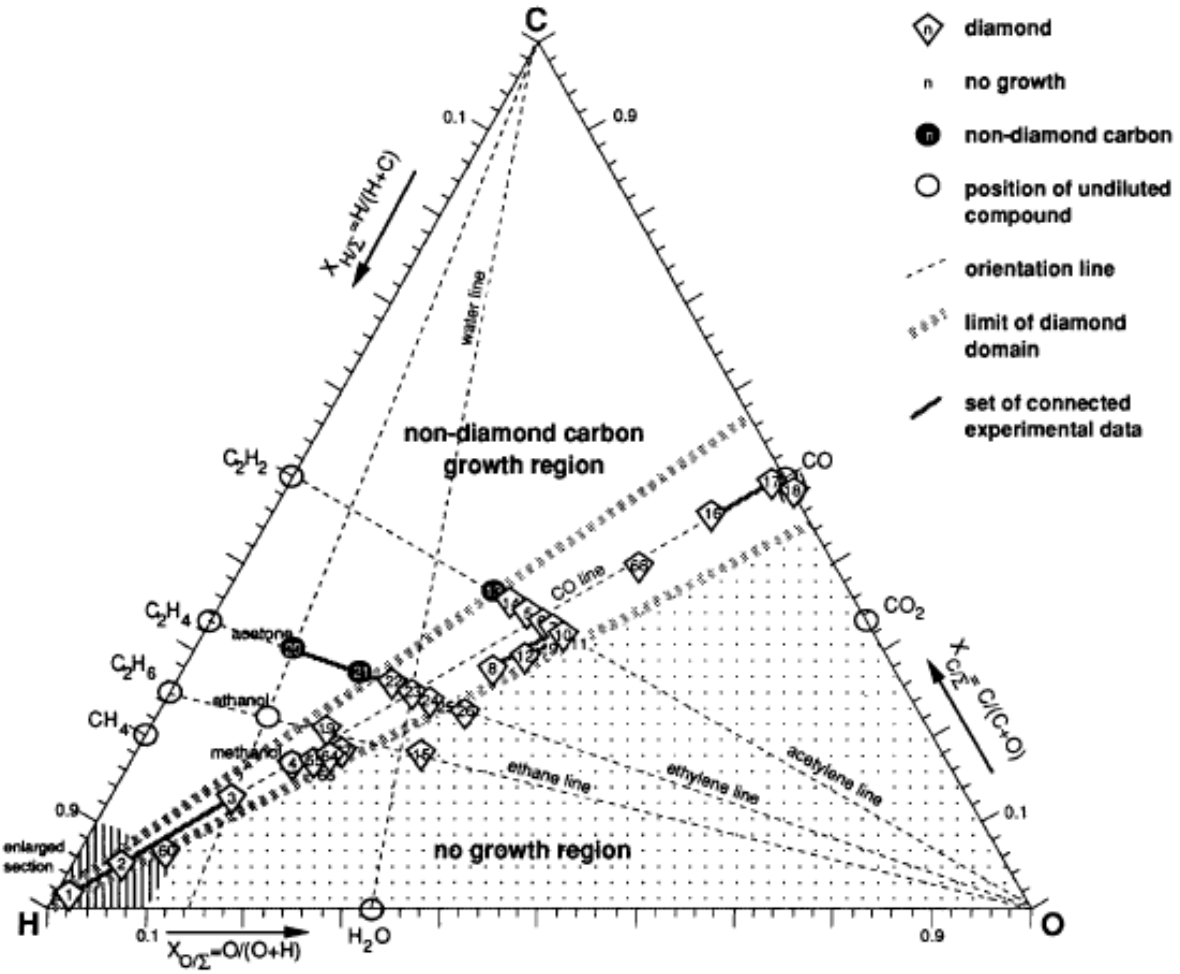

Fig 3.1: The original Bachmann diagram[6]

Many research groups have used the Bachmann diagram to guide experiments when changing the ratio of C/H/O and used various diagnostic tools to study these

plasmas.[12,13] The Vandenbulcke group from CNRS in Orleans, France have contributed significantly to the understanding of diamond growth via C/H/O plasmas. Their investigations include growth analysis of diamond films from different C/H/O gas mixtures,[14] OES and molecular beam mass spectrometry (MBMS) of the gas phase.[15,16] One of the results from the Vandenbulcke group,[14] in a agreement with others,[17] shows the increase in hydrocarbon species in CH_4/CO_2 plasmas when increasing the $\%CH_4$. A study into $CH_4/CO_2/H_2$ plasmas by Mollart and Lewis[18] found that the highest quality diamond is grown with equal amounts of carbon and oxygen in the plasma eg. on the CO tie line of the Bachmann diagram. Using the 1331 cm^{-1} Raman line, they conclude that the quality material decreases with increasing $\%CH_4$, once C>O in the input gas mixture. This is because the 1331 cm^{-1} line corresponds to sp^3 bonded carbon in diamond, and a decrease in the size of this line is representative of a decrease in grown films.

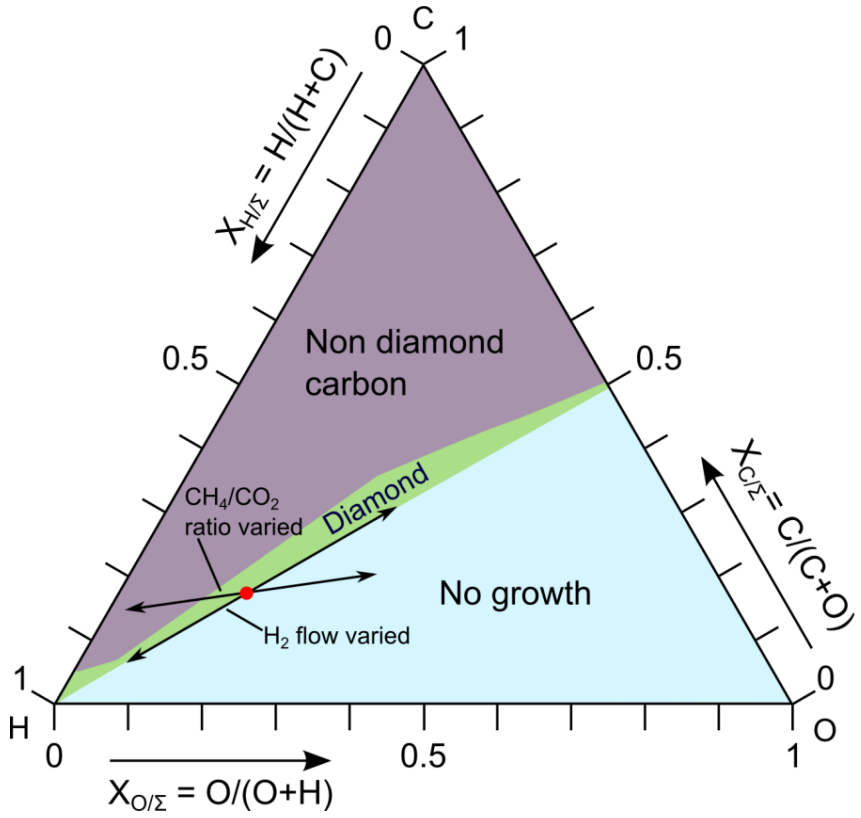

Fig 3.2 A more recent interpretation of the Bachmann diagram

As well as diagnostics of C/H/O plasmas, modelling of the gas phase chemistry has also been attempted. In 2009 Gries *et al.*[14] constructed a kinetic model of a CH_4/CO_2 plasma. The model was based on experimental results varying gas mixtures, flow rate, pressure and power and was based on pressures around 20 Torr. The model predicts

with reasonable accuracy the increase in carbon species and decrease in oxygen containing species with increasing inlet $\%CH_4$, as found experimentally with molecular beam mass spectroscopy (MBMS). May *et al.* also used MBMS results with gas phase simulations to explore trends. They changed the CH_4/CO_2 ratio and monitored the evolution of species within the plasma.[12] It was found that levels of hydrocarbon species increased once CH_4 was in excess of CO_2, and that oxygen containing species levels decreased with decreasing CO_2. The computational model produced results that suggested CO, H_2 and H were the most abundant species within the reactor, where CO is seen as a very stable species.

Calculations and experimental work give insight into which species are most abundant in C/H/O plasmas under different conditions, however there is one simple question, which has yet to be answered: Why can a particular growth temperature be achieved in a C/H/O plasmas at lower power than in a C/H plasma? The following section contains the most detailed diagnostic and modelling interpretations of C/H/O plasmas to date. Since comparisons are made between $CH_4/CO_2/H_2$ and CO/H_2 plasmas, diamond growth experiments are also included to show the optimum conditions for CVD diamond under these conditions.

3.2 Experimental

The MW reactor used for the experiments in this thesis was custom made and given to Bristol University diamond group by Element Six Ltd. on a long-term loan. A schematic of the reactor is shown in fig. 3.3. The reactor is cylindrical in shape, and the area in which plasma activation/diamond growth occurs sits below a centrally positioned quartz window. Gas flow was controlled using separate calibrated mass flow controllers. The separate input gases are premixed and enter the reactor via two diametrically opposed entrance channels. Microwaves at 2.45 GHz are fed through a waveguide, and pass through the quartz window and into the reactor where plasma activation occurs. The base of the reactor and the sidewalls were cooled with water. The top face of the quartz window is prevented from overheating via a cooling fan. The system allows operation at pressure $\leq$300 Torr, and at microwave powers up to around 1.8 kW. A constant pressure is kept in the reactor; the flow of gas leaving the reactor is controlled by regulating the pumping speed via a butterfly valve.

For laser and optical diagnostics, 30 mm long vertical slits exist on opposite sides of the reactor in exactly the same positions, behind each window. These allow laser light to pass through the reactor and into the detector for CRDS. Pulsed laser light (14) is produced using a Continuum Surelite III Nd:YAG laser, which pumps a Quanta Ray PDL-3 dye laser. The light pulses are 10 ns in duration, and arrive at a frequency of 10 Hz. The Nd:YAG laser is capable of producing three output wavelengths: 355 nm, 532 nm 1064 nm. The CRDS setup involves a cavity, which is 85 cm in length and consists of 2 arms (9) attached to the cavity walls over the vertical slits. The cavity is defined by the area between the two highly reflective (R>0.99) Layertech CRDS mirrors, which are under vacuum. The mirrors are positioned on adjustable mounts (15). A photomultiplier tube (PMT) (10) is used as a detector for light exiting the right hand mirror as shown in figure. 3.3. A digital LeCroy WaveRunner oscilloscope is used alongside a Labview program on a PC to display and collect the CRDS data. The arms and detector sit on an adjustable platform, which can be moved vertically relative to a fixed reactor with sub-millimetre precision.

In the present study, the species monitored using CRDS are: C_2 ($d^3\Pi_g$-$a^3\Pi_u$); CH ($A^2\Delta$-$X^2\Pi$); H (n=3 - n=2) and OH ($A^2\Sigma^+$-$X^2\Pi$). The dyes used for C_2, CH, H(n=2) and OH were:, Coumarin 503, Exalite 428, DCM and Rhodamine 640 frequency doubled using a KDP R6G crystal to achieve wavelengths in the region of 320 nm.

Base conditions for this work were: total pressure, p=150 Torr, total power, P = 1.5 kW and total flow F = 500 sccm (standard cubic centimetres per minute). At base conditions, within F = 500 sccm, $F(CH_4) = F(CO_2) = 175$ sccm and $F(H_2) = 150$ sccm. The elemental carbon mole fraction, $X_{C/\Sigma}$ is used to define the various gas mixtures, where $X_{C/\Sigma} = X_{elem}(C) / [X_{elem}(C) + X_{elem}(O)]$, and therefore $X_{C/\Sigma} = [X_0(CH_4)+X_0(CO_2)] / [X_0(CH_4) + 3X_0(CO_2)]$. And $X_{elem}(C) = [(F(CH_4) + F(CO_2)] / [5F(CH_4) + 3F(CO_2) + 2F(H_2)]$. Base conditions, unless stated otherwise, therefore correspond to $X_{C/\Sigma} = 0.5$ and $X_0(H_2)=0.3$. The red dot on fig. 3.2 shows where experimental base conditions sit on the Bachmann diagram, with regards to the elemental mole fractions of C, H and O. For CO/H_2 measurements, $X_{C/\Sigma} = 0.5$. The calculated elemental mole fractions in a $CH_4/CO_2/H_2$ plasma at $X_{C/\Sigma} = 0.5$ is C=0.206, O=0.206 and H=0.588. The equivalent means that the CO must have an elemental mole fraction of 0.412, if $X_0(H_2)=0.588$. The CO/H_2 ratio was therefore 41.2%CO/58.8%H_2.

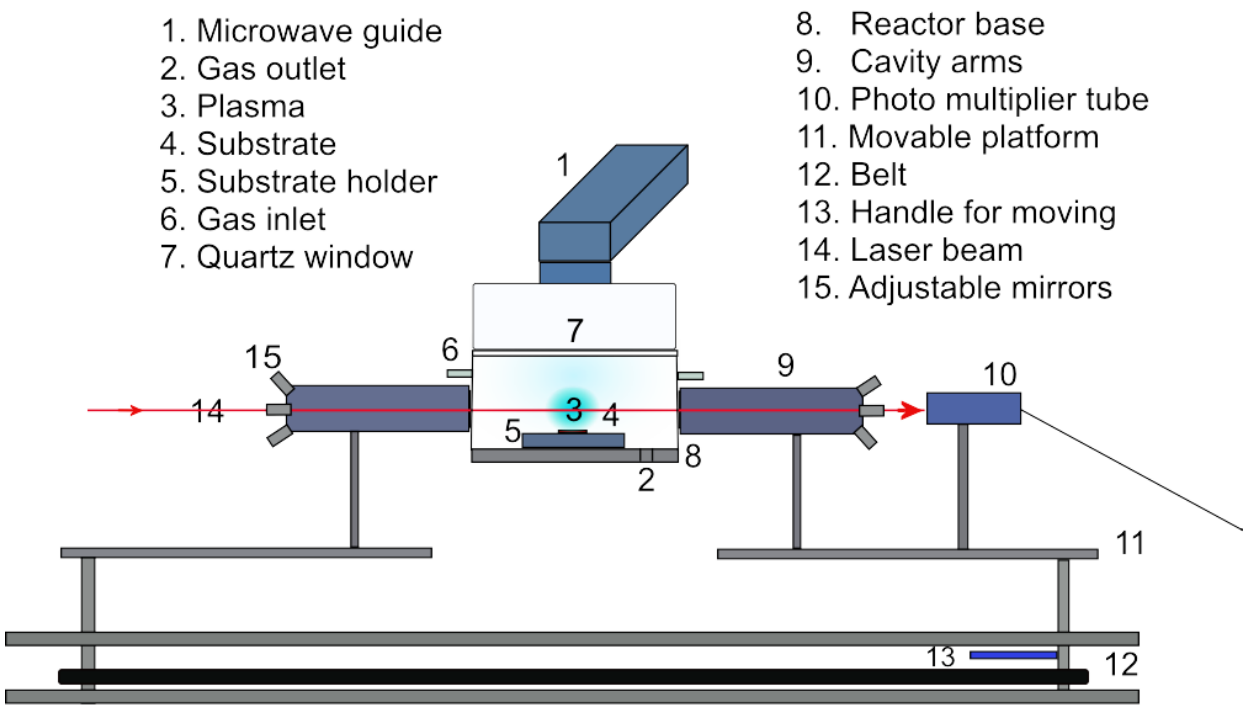

Fig. 3.3 Schematic diagram for the CRDS experimental setup

3.3 Results and Discussion

3.3.1 Measured CRDS absorption spectra

For measuring absorption spectra from C_2, the C_2 Swan system provides the electronic ($d^3\Pi_g$-$a^3\Pi_u$) (0,0) transition in the green. The C_2 transition is from the $a^3\Pi_u$ state, as opposed to the ground state $X^1\Sigma_g^+$. The reason for this relates to the degeneracies of the 2 electronic states. Which are, respectively 1 for the $X^1\Sigma_g^+$ state and 6 for the $a^3\Pi_u$ state. The fraction of upper, N_k and lower, N_j state populations is given by:

$$\frac{N_k}{N_j} = \frac{g_k}{g_j} exp^{\left(-\frac{\Delta E}{kT}\right)}$$

where g_k/g_j=6, ΔE=0.088 eV and T_e=1.2 eV. This implies the population in the $a^3\Pi$ state to be around 5.5 times that of the $X^1\Sigma_g^+$ state. The section of the C_2 ($d^3\Pi_g$-$a^3\Pi_u$) (0,0) transition measured experimentally by CRDS is shown in fig. 3.4. The three lines at lower wavenumber correspond to R branch transitions from low J levels. The last 3 correspond to P branch transitions from high J levels, of which the last line is a convolution of two. The positioning of transitions of low rotational levels next to higher rotational levels allows the use of recorded absorption spectra to give a measure of the gas temperature (T_{gas}), on the basis that rotational-translational energy transfer processes are sufficiently fast to ensure local thermodynamic equilibrium. The population of higher rotationally excited J levels, the P lines in fig. 3.4, will be greater at higher T_{gas}, and so the ratio between the low J (R) and high J (P) lines will increase, or decrease with changing T_{gas}. Mapping recorded spectra onto a spectral simulation program then allows estimation of T_{gas}, by comparison of recorded data to the simulation based on the ratio of the R and P line intensities. An example of how this particular spectrum changes with increasing T_{gas} on simulated spectra is simulated in fig. 3.5. The data in fig. 3.5 comes from pgopher, and is part of the C_2 ($d^3\Pi g$-$a^3\Pi_u$) (0,0) band. Data collected experimentally are nearest to the 3000 K spectra.

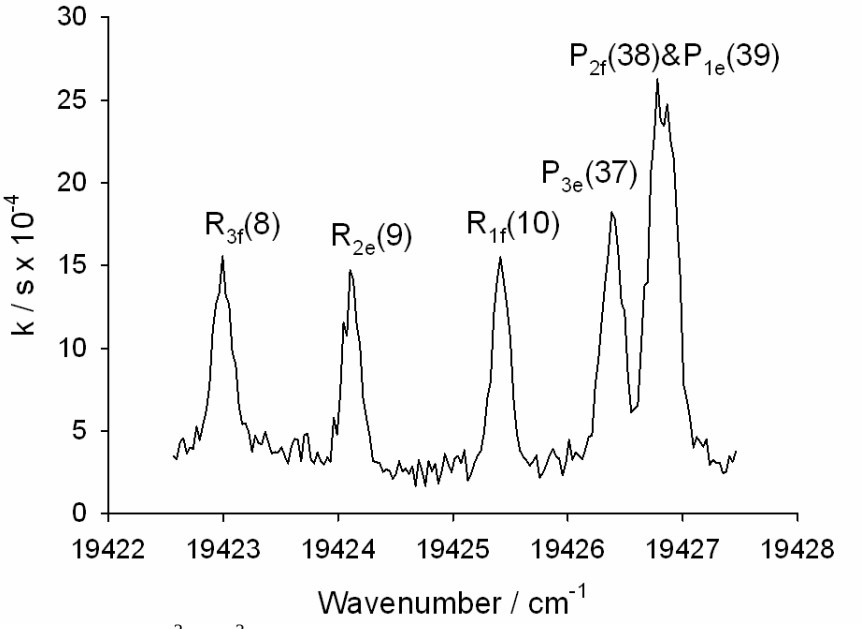

Fig. 3.4 Measured C_2 ($d^3\Pi_g$-$a^3\Pi_u$) (0,0) absorption spectrum measured by CRDS

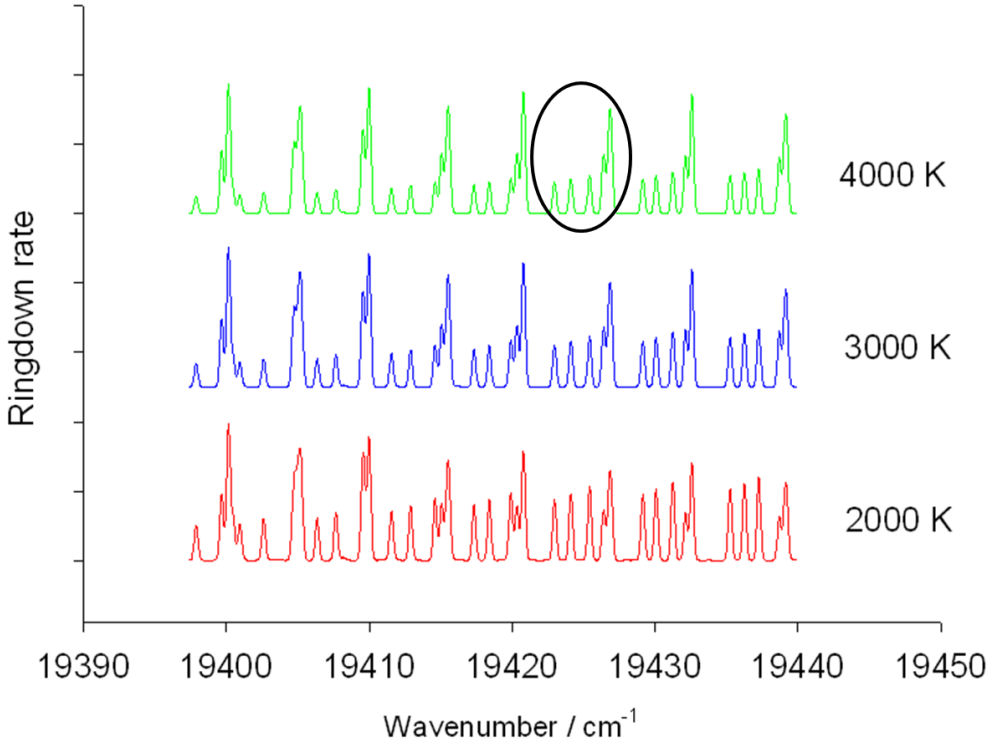

Fig. 3.5 Part of the C_2 ($d^3\Pi g$-$a^3\Pi_u$) (0,0) spectrum simulated by pgopher, at 3 different temperatures. The area used for CRDS measurements has been circled.

The band origin of the CH ($A^2\Delta$-$X^2\Pi$) (0,0) transition is at 431 nm. All rotational lines measured are R branch transitions, and the second line measured is a

convolution of two transitions. The measured absorption spectrum of CH is shown in fig. 3.6.

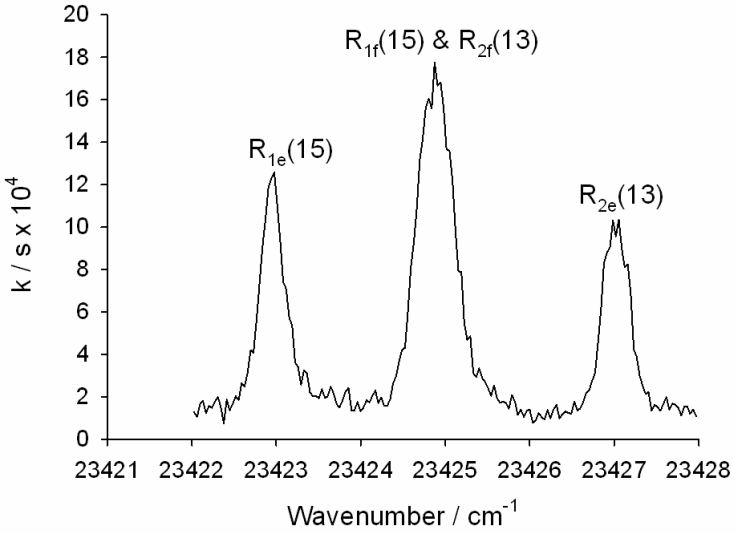

Fig. 3.6 Measured CH ($A^2\Delta$-$X^2\Pi$) (0,0) absorption spectrum recorded by CRDS.

The H(n=3 ← n=2) Balmer-alpha transition is in the red, and an example of the spectrum recorded is in fig. 3.7. The line recorded for H(n=2) is a convolution of seven fine structure transitions. The broadening of these seven lines merges them together in the formation of one broad peak at 656 nm.

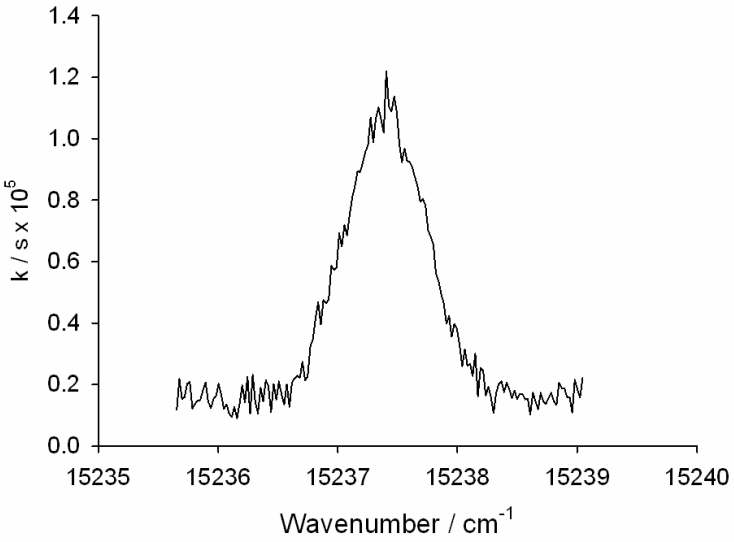

Fig. 3.7 Measured H(n=2) spectrum recorded by CRDS.

The part of the OH ($A^2\Sigma^+$-$X^2\Pi$) (0,0) spectrum chosen for study consists of one Q branch and two R branch transitions. A typical absorption spectrum for OH is shown

in fig. 3.8. Like C_2 the presence of transitions from low J next to transitions involving high J levels allows estimation of the gas temperature. An example of the change in peak size for low and high J levels with increasing T_{gas} is shown in fig. 3.9.

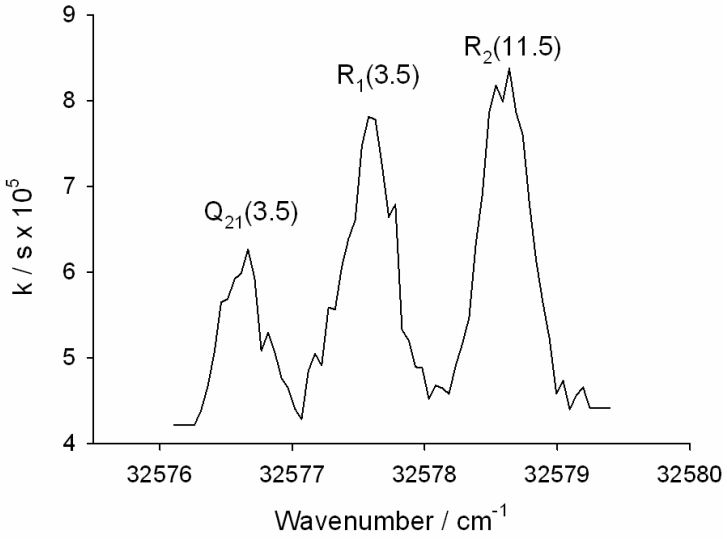

Fig. 3.8 Measured OH ($A^2\Sigma^+$-$X^2\Pi$) (0,0) spectrum recorded by CRDS.

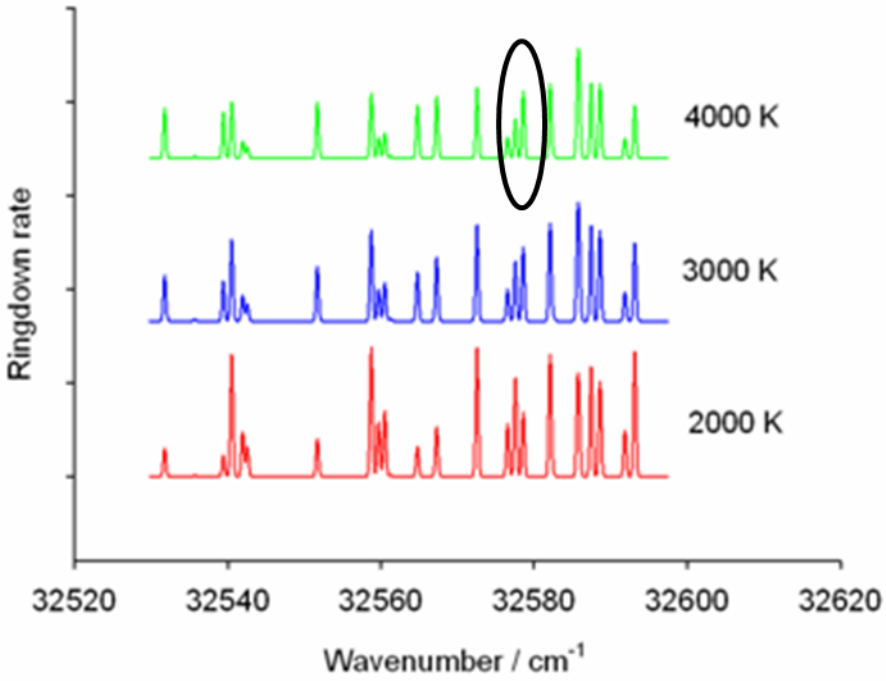

Fig. 3.9. Part of the OH ($A^2\Sigma^+$-$X^2\Pi$) (0,0) spectrum simulated by Pgopher. The area used for CRDS measurements has been circled.

3.3.2 Column density calculations

The collection of rotational lines from C_2, CH and OH transitions are used in the calculation of the respective column densities of these species within the plasma. When considering the absorption of light by a species at a particular wavelength, it is important to acknowledge the absorption coefficient, α, as shown in equations (3.1) and (3.2).

$$\alpha = \frac{L\Delta k}{c\, l_{eff}} \tag{3.1}$$

$$\int \alpha d\tilde{\nu} = \frac{\lambda^2}{8\pi c} \cdot \frac{g_k}{g_j} \cdot [X]\, A_{oo} p \tag{3.2}$$

Equation (3.1) shows how the absorption coefficient relates to the difference in ringdown rate where L is the distance between the two mirrors, Δk is the measured change in ringdown rate, c the speed of light and l_{eff} the length occupied by the absorber. Equation (3.2) relates the integrated absorption over the whole line profile to the concentration of absorbing species within the plasma, where $\tilde{\nu}$ is the wavenumber, λ the wavelength, g_k and g_j the degeneracy of upper and lower levels, [X] the concentration of the absorber, p the fraction of the total band oscillator strength of the rotational line, and A_{oo} the Einstein A coefficient. Substituting equation (3.1) into equation (3.2), with some rearrangement gives equation (3.3), to calculate the column density of the absorbing species.

$$[X] l_{eff} = \frac{L8\pi}{\lambda^2 A_{oo} p} \cdot \frac{g_j}{g_k} \cdot \int \Delta k d\tilde{\nu} \tag{3.3}$$

where $[X]l_{eff}$ gives the column density D for the measured species.

This formula cannot, however be used for H(n=2) column density calculations. The reason for this is that H(n=2) is an atom, and its spectrum therefore does not have vibrational and rotational fine structures for which the above formula has been developed.

As shown in fig. 2.4, the Hα transition is a convolution of seven transitions between 3 lower levels in n=2 ($^2S_{1/2}$, $^2P_{1/2}$ and $^2P_{3/2}$) and 5 levels in n=3 ($^2S_{1/2}$, $^2P_{1/2}$, $^2P_{3/2}$, $^2D_{3/2}$, $^2D_{5/2}$). The seven individual lines are not resolved; the broadening of these transitions gives one line. The absorption and excitation from n=3 ← n=2 will depend upon the population of lower levels. Equation (3.4) shows the relationship between the absorption coefficient and number density N_j. The absorption coefficient is proportional to the ringdown rate and will also depend upon σ, the absorption cross section.

$$\int \alpha d\tilde{\nu} = \sum_{j,k} N_j \, \sigma_{j,k} \tag{3.4}$$

The population of the lower n=2 levels is related to their degeneracy, since these levels are very close in energy. The relation of N_j to $N_{H(n=2)}$ is shown in equation (3.5)

$$N_j = N_{H(n=2)} \frac{g_j}{\sum_j g_j} \tag{3.5}$$

where $N_{H(n=2)}$ is the total population in n=2. In equation (3.5) $\sum_j g_j$ represents the sum of degeneracies in lower levels, which is 8.

The relationship of the absorption cross section, σ, to the Einstein A coefficient is,

$$\sigma_{jk} = \frac{h\nu}{c} . \frac{g_k A_{kj} \lambda^3}{g_j 8\pi c}$$

$$= \frac{g_k A_{kj} \lambda^2}{g_j 8\pi h} \tag{3.6}$$

Substituting equations (3.5) and (3.6) into (3.4) gives equation (3.7):

$$\int \alpha d\tilde{\nu} = N_{H(n=2)} \frac{g_j}{8} . \frac{g_k A_{jk} \lambda^2}{g_j 8\pi} \tag{3.7}$$

$$\int \alpha d\tilde{\nu} = \frac{N_{H(n=2)}}{64\pi} \sum_{jk} A_{kj} g_k \lambda^2 \tag{3.8}$$

Integrating equation (3.1), the absorption coefficient can also be written as (3.9):

$$\int \alpha d\tilde{\nu} = \frac{L}{cl_{eff}} \int \Delta k \, d\tilde{\nu} \tag{3.9}$$

Combining equations (3.8) and (3.9) gives equation (3.10):

$$\frac{L}{cl_{eff}} \int \Delta k \, d\tilde{\nu} = \frac{N_{H(n=2)}}{64\pi} \sum_{jk} A_{kj} g_k \lambda^2$$

$$N_{H(n=2)} \cdot l_{eff} = D_{H(n=2)} = \frac{64\pi L}{\sum_{jk} A_{kj} g_k \lambda^2} \int \Delta k d\tilde{\nu} \tag{3.10}$$

Equation (3.10) is used to calculate the column densities of H(n=2) in the plasma, where $\int \Delta k \, d\tilde{\nu}$ is the area under the peak, which is fitted using a Gaussian function, and $D_{H(n=2)}$ is the column density of H(n=2). Column densities calculated at a given p, P, $X_{C/\Sigma}$, and z were each repeated three times in order to use a standard deviation calculation to calculate an error for each measurement.

3.3.3 CRDS column density measurements

The spectra recorded used in conjunction with the equations listed in section 3.3.2 are used to calculate column densities of C_2(a, v=0), CH(X, v=0), OH(X, v=0) radicals and H(n=2) atoms whilst varying experimental parameters and conditions. Experimental results are used to validate a 2D model, which in turn gives a detailed analysis of the plasma. Calculated column densities are discussed in the following section, followed by a discussion of experimental results, compared with 2D(r,z) model results. Further results from the model will also be discussed.[19]

As shown in fig. 3.3, the reactor arms and PMT detector sit on a moveable platform, which allows profiling of the plasma. This allows the investigation of column densities of selected species as a function of height (z) above the substrate. Fig. 3.10 shows z-dependent profiles for C_2(a, v=0), CH(X, v=0), OH(X, v=0) radicals and H(n=2) atoms. For measurements using a $CH_4/CO_2/H_2$ plasma, for all species except OH, $X_{C/\Sigma}$=0.505. This corresponds to a 51%CH_4/49%CO_2 ratio. When F(CH_4) is in slight excess of F(CO_2), it is easier to record well defined peaks for C_2 and CH. OH

data were recorded at $X_{C/\Sigma}$=0.5 which corresponds to a 50%CH_4/50%CO_2 ratio, and is because when %CH_4 is in slight excess of %CO_2 it is difficult to record well defined peaks of OH. For the CO/H_2 plasma, elemental mole fractions for a CO/H_2 gas mixture were calculated, which were equivalent to the base conditions for a CH_4/CO_2/H_2 gas mixture, assuming X_{elem}(H)=0.588, which gives a CO/H_2 ratio of 41.2%CO/58.8%H_2.

The C_2 and CH distributions within the plasma are similar, due to their formation being dependent mainly upon thermal chemistry. Their column densities maximize at around z=8.5 mm. CH column densities are around an order of magnitude greater than those for C_2. The distribution of H(n=2) sits lower in the plasma in comparison to C_2 and CH at around z=7 mm OH distribution peaks at around 10mm and extends to higher z than C_2 and CH, indicating that its distribution and formation may not be as dependent upon the local T_{gas}. Open symbols represent data for OH and CH recorded from a CO/H_2 plasma. Calculated column densities for CH and OH are lower in these plasmas than in a CH_4/CO_2/H_2 plasma, which will be discussed further in the following section.

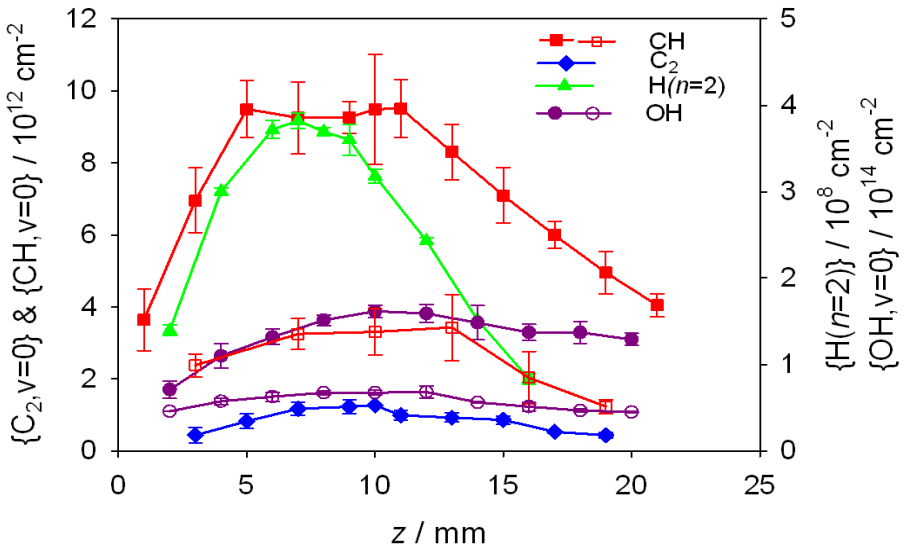

Fig. 3.10 (a) Column densities of C_2(a, v=0), CH(X, v=0), OH(X, v=0) radicals and H(n=2) atoms measured as a function of height (z). Solid symbols represent a CH_4/CO_2/H_2 plasma operating at base conditions, where for OH $X_{C/\Sigma}$ = 0.5, and or all other species $X_{C/\Sigma}$ = 0.505. Open symbols represent measured column densities of CH(X, v=0) and OH(X, v=0) in a 41.2% CO/58.8% H_2 plasma, operating at base conditions.

Fig. 3.11 (a) and (b) show differences in column density trends between H(n=2), OH, C_2 and CH with increasing $X_{C/\Sigma}$. These measurements were taken at 2 different X_0(H_2)

values, 0.3 and 0.6. $X_0(H_2)$ represents the mole fraction of H_2 in the feed gas. $X_{C/\Sigma}$ values were calculated first from the CH_4/CO_2 ratio ie. 57% CH_4/CO_2 at $X_0(H_2)$=0.3 gives the CH_4 flow rate out of a total (CH_4+CO_2)=350 sccm as F(CH_4)=199 sccm and F(CO_2)=151 sccm, where F(H_2)=150 sccm. Substituting these values into $X_{C/\Sigma}$= $X_0(CH_4)$+$X_0(CO_2)$/[$X_0(CH_4)$ + 3$X_0(CO_2)$], this gives $X_{C/\Sigma}$= 0.537, which corresponds to the final data points on plots 3.11 (a) and (b).

In both 3.11 (a) and (b) there is a clear difference in trends between O and C containing species when increasing $X_{C/\Sigma}$. In fig. 3.11 (a), when crossing $X_{C/\Sigma}$=0.5 there is an increase in C_2 and CH column densities. With increasing $X_{C/\Sigma}$ there is also a decrease in OH column densities. The same trends are observed in (b), although the increase in C_2 and CH and decrease in OH column densities are more gradual. When comparing column densities for species in (a) and (b), there is a decrease in the column densities of CH and C_2, with a slight increase in H(n=2) and no change in the measured OH column densities when increasing $X_0(H_2)$.

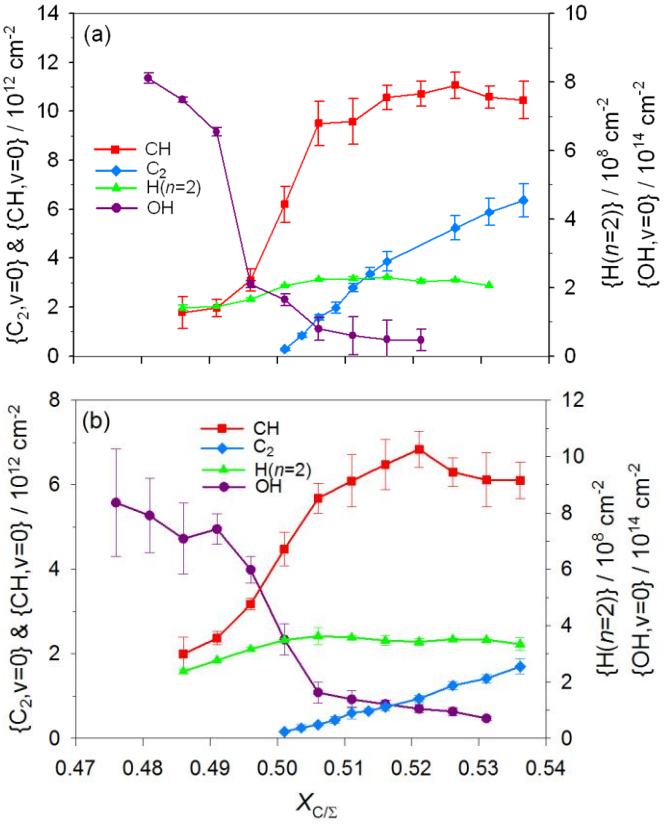

Fig. 3.11 Column densities of C_2(a, v=0), CH(X, v=0), OH(X, v=0) radicals and H(n=2) atoms in a $CH_4/CO_2/H_2$ plasma with increasing $X_{C/\Sigma}$. with (a) $X_0(H_2)$=0.3, and in (b) $X_0(H_2)$=0.6 measured by CRDS at z=10 mm.

The effect of increasing $X_0(H_2)$ can also be seen in fig. 3.12, where column densities of C_2, CH, OH radicals and H(n=2) atoms have been measured as a function of $X_0(H_2)$. The $X_{elem}(C)$ values are shown along the top axis whilst increasing $X_0(H_2)$.

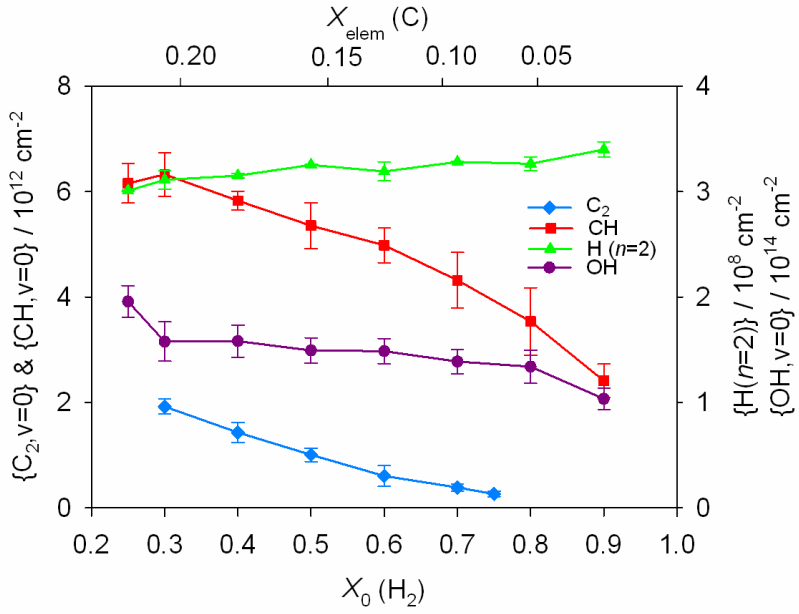

Fig. 3.12 Column densities of C_2(a, v=0), CH(X, v=0), OH(X, v=0) radicals and H(n=2) atoms in a $CH_4/CO_2/H_2$ plasma with increasing $X_0(H_2)$ measured by CRDS at z=10 mm with $X_{C/\Sigma}$=0.5 for OH and 0.505 for all other species. The elemental mole fraction of carbon, $X_{elem}(C)$ is shown along the top axis.

Fig 3.12 shows a decrease in C_2 and CH column densities with increasing $X_0(H_2)$, which is in agreement with the increase in $X_0(H_2)$ in fig. 3.11 (a) and (b). There is no noticeable change in H(n=2) column densities and only a small decrease in OH column density with increasing $X_0(H_2)$, which again shows the insensitivity of these species to large changes in $X_0(H_2)$.

Changes in C_2, CH, OH and H(n=2) column densities with changing power and pressure are shown in fig. 3.13.

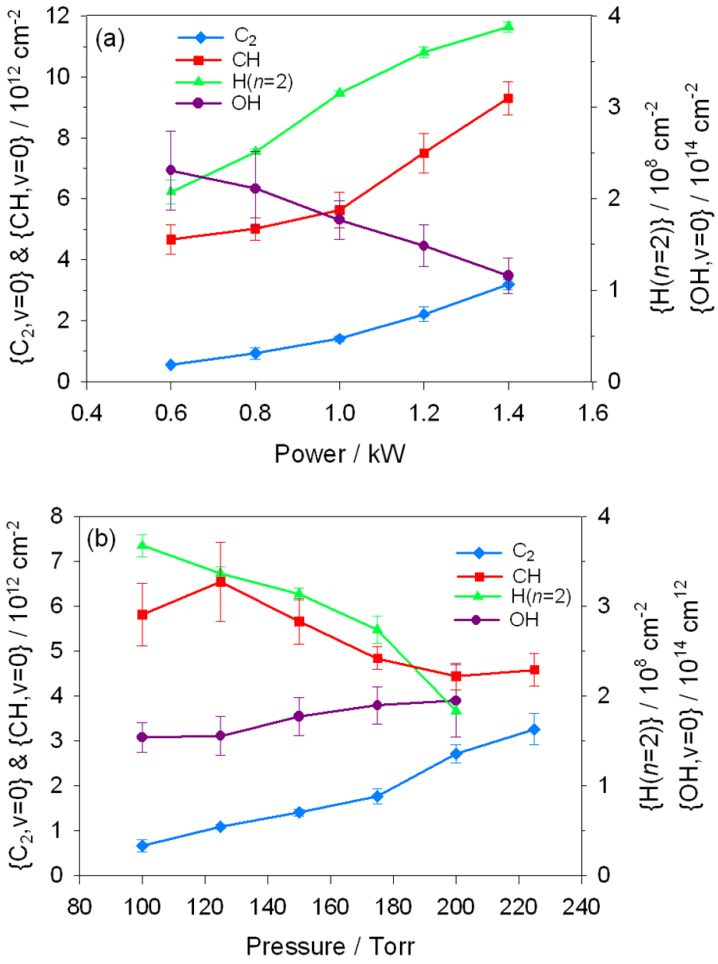

Fig. 3.13 Column densities of C_2(a, v=0), CH(X, v=0), OH(X, v=0) radicals and H(n=2) atoms in a $CH_4/CO_2/H_2$ plasma with increasing (a) MW power and (b) pressure measured by CRDS at z=10 mm with $X_0(H_2)$=0.3 and $X_{C/\Sigma}$=0.5 for OH and 0.505 for all other species.

Increasing the power in a $CH_4/CO_2/H_2$ plasma as in fig. 3.13 (a) results in an increase in column densities of C_2, CH and H(n=2) species but a decrease in OH(X) column densities. Increasing the pressure causes a decrease in H(n=2) column densities and a 4-fold increase in C_2 column density with no substantial changes in the column densities of CH and OH.

3.3.4 Discussion of column density measurements with reference to 2-D model results

The determination of the column densities of key species is the first step to giving a thorough description of $CH_4/CO_2/H_2$ plasmas. Experimental data are used to validate a 2-D(r,z) model.[20] In the model, equations are solved for mass, momentum, energy and species concentration. The model then describes: power absorption, gas heating and heat and mass transfer, plasma activation, plasma-chemical kinetics, the electron energy distribution function (EEDF), species and mass diffusion, ambipolar diffusion of charged species and gas-surface processes. The model assumes cylindrical symmetry and has coordinates r, the radial distance from the center axis of the reactor, and z, the axial distance from the centre of the substrate. OES and CRDS data guide the model, and give an idea of the plasma volume, V, which is incorporated as a parameter and allows estimation of the reduced electric field E/N and T_e. The model plasma chemical-kinetics mechanism includes >500 forward and reverse reactions for neutral species (eg. C_2H_y (y=1-6)), charged species (eg. H_3O^+) and electronically excited atoms and molecules (eg. H(n=2,3)).

The model predicts that the plasma-chemical kinetics and power absorption pathways are much the same as those calculated for C/H plasmas.[20] The main difference here is the presence of CO which, like H_2, acts as a substantial absorber of power via rotational-vibrational excitation through interaction with electrons. The model predicts that mainly CO and H_2 account for 78% of the total power absorption by the gas. Another substantial difference due to the presence of CO is the electronic excitation of CO into its metastable $a^3\Pi$ state, which accounts for 17.5% of the absorbed power, since CO is such an abundant species within the reactor. The rest of the absorbed power is lost via elastic collisions/dissociation reactions of electrons with gas phase species. The quenching of excited gas phase species (mainly CO and H_2) then leads to gas heating. The gas may also lose energy via interaction with the reactor base, substrate and walls as well as in the dissociation of H_2.

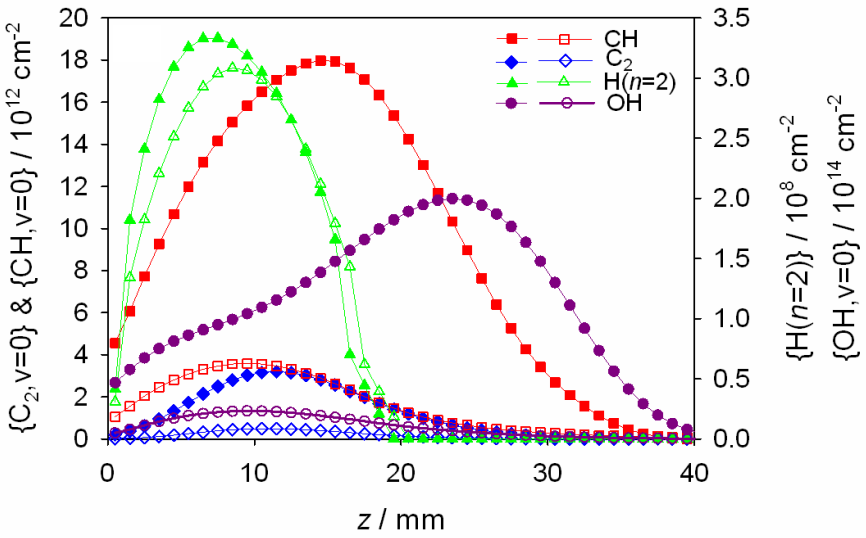

Fig 3.14. z-dependent column densities from the 2-D model, calculating column densities for C_2(a, v=0), CH(X, v=0), OH(X, v=0) radicals and H(n=2) atoms in a $CH_4/CO_2/H_2$ plasma under base conditions. Closed symbols represent a $35\%CH_4/35\%CO_2/30\%H_2$ plasma. Open symbols represent a $41.2\%CO/58.8\%H_2$ plasma.

Fig. 3.14 shows results from the model calculating column densities in both $35\%CH_4/35\%CO_2/30\%H_2$ and $41.2\%CO/58.8\%H_2$ plasmas under base conditions. When comparing 2-D profiles with experimental results as in fig. 3.10, there are both similarities and discrepancies. The distribution of C_2, CH and H(n=2) species in the model match well with experimental results; C_2 and CH peak at $z\approx10$ mm, whereas H(n=2) peaks lower in the plasma, at $z\approx8$ mm. This is due to H(n=2) formation being reliant on the overlap of H(n=1) with high energy electrons (T_e>10 eV). The returned H(n=2) column densities from the model match those from experimental results. Column densities for C_2, CH and OH reported by the model are higher than determined experimentally. The explanation for this discrepancy comes from the gas inputs used for the model and experiment being different. The model assumes gas entry via a cylindrical ring at r=6 cm, whereas the experiment feeds gas in via 2 diametrically opposed pipes. This means that the area above the plasma where CH_4 and CO_2 are dominant experimentally is composed of 2 cloud-like areas below each pipe inlet, which can then feed into the plasma. In the model, however, a ring shaped cloud of CH_4 and CO_2 exists below the cylindrical feed gas entry into the plasma.

When considering the effect increasing $X_{C/\Sigma}$ has on the column densities of species as in fig. 3.11, there is an increase in C containing species, and a decrease in O containing species. With increasing F(CH_4) and therefore $X_{C/\Sigma}$, C_2 is seen to increase

roughly linearly, whereas the increase in CH shows more of a square root dependence. This is consistent with previous model results which show the dependencies as $[CH_4]=[C_2]$ and $[CH_4]^{0.5}=[CH]$. The increase in C_2 and CH column densities and decrease in OH can be understood by recognizing that under base conditions, the bulk of CH_4 and CO_2 fed into the reactor will be converted to CO and H_2, and if either carbon or oxygen are in excess of one another, this will lead to one species 'mopping' up the other. Calculated 2-D(r,z) model results show distributions of CH, C_2H_2, OH and H_2O mole fractions for base reactor conditions in fig. 3.15 (c) and (d). What is clear from this is that although experimental results may provide an accurate description of species distribution with changing conditions in the plasma, the model predicts additional subtleties.

Fig. 3.15 shows calculated 2D(r, z) mole distributions of CH, C_2H_2, OH and H_2O mole fractions for base reactor conditions with three different input mixtures where $X_0(H_2) = 0.3$ and: $X_{C/\Sigma} = 0.46$ in (a) and (b); 0.5 in (c) and (d); 0.53 in (e) and (f). Above each 2D plot are the species and the mole fraction scale from min to max (white to red). In moving from oxygen rich to carbon rich conditions, there is a clear increase in concentration of CH and C_2H_2. When moving from (a)→(c)→(e) the distribution of CH is moving from a thin annular region around the hot plasma centre, when $X_{C/\Sigma}<0.5$, to a larger area outside the centre at $X_{C/\Sigma}=0.5$, to dominating in the central region of the plasma in carbon rich conditions when $X_{C/\Sigma}>0.5$. When moving from (b)→(d)→(f), the concentration and distribution of OH almost mirrors that of CH within the plasma when moving from oxygen rich to carbon rich conditions; OH dominates in the central region under oxygen rich conditions, moving into an annular region around the hot central region when $X_{C/\Sigma} = 0.5$, which then thins as the plasma becomes carbon rich. It is also clear that H_2O in the peripheral region decreases in concentration as C_2H_2 is increasing, when moving from (b)→(d)→(f). The clear increase in concentration of carbon species with increasing $X_{C/\Sigma}$ in the 2D model compares well with experimental results in fig. 3.11. These results also indicate that for a reasonable diamond growth rate, $X_{C/\Sigma}$ should be slightly greater than 0.5 in order to ensure that a high enough concentration of CH_3 radicals exists in the area above the diamond surface. The model predicts that, as in C/H plasmas, CH_3 radicals are the most abundant C_1H_x [x = 0-3] species near the growing diamond surface: $[CH_3]$

~2.5×10^{13} cm^{-3} at base conditions. The conclusion here is that the C/O balance represents one major difference between C/H/O plasmas and conventional C/H plasmas, in which the distribution of species can change dramatically with only a small change in the input gas ratio.

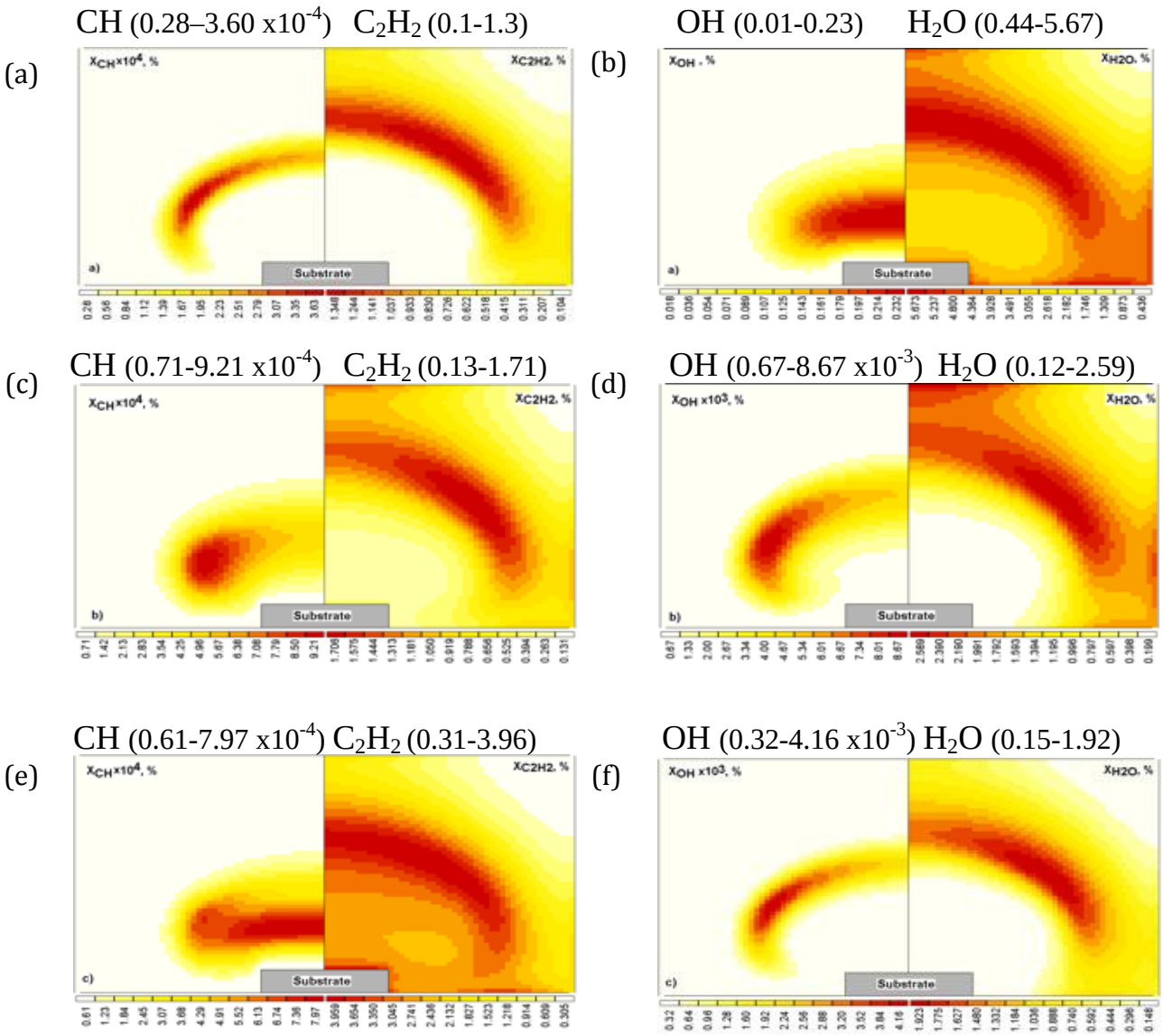

Fig.3.15, Calculated 2D(r, z) mol distributions of CH, C_2H_2, OH and H_2O mole fractions for base reactor conditions (P = 1.0 kW, p = 150 Torr) and three different input mixtures: $X_0(H_2)$ = 0.3 and $X_{C/\Sigma}$ = (a) and (b) 0.46; (c) and (d) 0.5; (e) and (f) 0.53. Above each 2D plot are the species and the mole fraction scale from min to max (white to red).

The C/O balance clearly has a dramatic effect on the distribution of both carbon and oxygen containing species within the plasma. Under base conditions C_xH_y and OH_x

species both maximize in an annular region around the hot central core of the plasma, which consists mainly of CO and H_2. Model results show that diffusion of C_2H_2 and H_2O from annular regions in the plasma periphery provide the source of CH_x species (x=0-3) and OH in the plasma zone. Examples of reactions for the depletion of C and O containing species in the plasma are,

$$O + C_2H_2 \leftrightarrow H + HCCO \quad (3.11)$$

$$\leftrightarrow CO + CH_2 \quad (3.12)$$

$$OH + C_2H_2 \leftrightarrow H + CH_2CO \quad (3.13)$$

$$H + CO_2 \leftrightarrow OH + CO \quad (3.14)$$

where all reactions ultimately lead to the formation of the most stable end point species, CO. Since CO and H_2 are the most stable end products that form in a $CH_4/CO_2/H_2$ plasma from the mutual destruction of C and O containing species, would the plasma have the same structure if we replace CO_2 and CH_4 with CO as a source gas? Comparing model results from fig. 3.14 shows that the spatial distributions of species in a CO/H_2 plasma are different from that in a $CH_4/CO_2/H_2$ plasma. This suggests that the plasma has a completely different structure, and does not contain the same annular regions providing the source for CH and OH species in the hot plasma core as in $CH_4/CO_2/H_2$ plasmas. CO a is very stable molecule, and the C-O bond difficult to break. The model predicts that formation of C and O in a CO/H_2 plasma comes from the dissociation of CO as a result of interactions with $CO(a^3\pi)$ and electron impact dissociation. The difficulty in forming C and O from a CO/H_2 plasma is reflected in both experimental and model calculations in figs. 3.10 and 3.14. These show that in a CO/H_2 plasma, the concentrations of CH and OH are lower than in a $CH_4/CO_2/H_2$ plasma.

With regards to increasing $X_0(H_2)$ as shown in fig. 3.11(a) and (b), it is clear that the increase in C species and decrease in O containing species when crossing $X_{C/\Sigma}$=0.5 becomes more gentle. The model suggests that this is due to a decrease in the plasma size with increasing $X_0(H_2)$. This coincides with an increase in thermal conductivity, and a decrease in the maximal plasma temperature. The decrease in plasma size with the increase in $X_{elem}(H)$ and decrease in $X_{elem}(C)$ and (O) makes the plasma more and more reminiscent of C/H plasmas. This therefore moves the plasma away from the

structure of having these annular regions where an incomplete mutual destruction of C_xH_y species with H_xO occurs. There is therefore a steeper increase in C_2 and CH column densities when $X_0(H_2)$=0.3 compared to $X_0(H_2)$=0.6, as in $X_0(H_2)$=0.6 the destruction of of C_xH_y species with H_xO is reduced. From fig. 3.13, the decrease in C_2 and CH number densities also coincides with the decrease in $X_{elem}(C)$ with increasing $X_0(H_2)$. There is little change in OH and H(n=2) column densities showing their insensitivity to $X_0(H_2)$. H(n=2) may be expected to rise with $X_0(H_2)$, but number densities are a sensitive function of the H(n=1) overlap with the distribution of high energy electrons, and T_{gas}.

3.4 Further conclusions from the model

In keeping with the plasma distribution of oxygen and carbon containing species, an important and unusual conclusion from this work, and specifically the 2D model, is the elctron density, n_e, which maximizes away from the plasma core under base conditions. In these C/H/O plasmas, there is a sensitivity towards which is the dominant ion, which is dependent on the ratio of $[C_xH_y^+]/[H_3O^+]$, and the ion exchange reaction $H_3O^+ + C_xH_y \leftrightarrow H_2O + C_xH_y^+$. In carbon rich conditions the dominant ion is $C_2H_2^+$, whereas under oxygen rich conditions the dominant ion is H_3O^+. At base conditions, the dominant ion in the plasma centre is $C_2H_2^+$, whereas H_3O^+ exists in an annular region outside the center. Electrons are greater in density in an annular region around the plasma core, as they follow the distribution of H_3O^+. This can be explained by considering the relative ion-electron recombination rate coefficients for H_3O^+ and $C_2H_2^+$. The ion-electron recombination coefficient for H_3O^+ is an order of magnitude lower than that for $C_2H_2^+$. The electron density therefore follows the distribution of the ion with the lowest ion-electron recombination coefficient, as electrons are less likely to recombine with their counter cations.

Another important difference between C/H/O and C/H plasmas is the power used experimentally to produce the same T_{gas} values; C/H plasma P = 1.5 kW, C/H/O P = 1 kW. The 2D model has predicted the reason for this being that C/H/O plasmas have a lower thermal conductivity coefficient: $\lambda_{C/H/O} \approx \lambda_{C/H}/2.3$ for T_{gas} ~1500-3000 K. The

lower thermal conductivity value for C/H/O plasmas means that the input power is better retained in the localized plasma volume.

3.5 Growth experiments

To investigate the effect changing the C/H/O ratio has on the diamond CVD process, several films were grown. These were grown to show changes in film thickness and growth rate, as well as film morphology when crossing $X_{C/\Sigma}$=0.5 in a $CH_4/CO_2/H_2$ plasma, and then comparing these to a CO/H_2 plasma.

Scanning electron microscopy (SEM) images from these growth experiments are shown in fig. 3.16. In fig. 3.16, (a)→(b) show cross-sectional and plan views of a film grown with $X_{C/\Sigma}$=0.495, (c) →(d) for $X_{C/\Sigma}$=0.5 and (e)→(f) for $X_{C/\Sigma}$=0.51. All films were grown for 3 hours under base conditions where $X_0(H_2)$=0.3, p=150 Torr and P=1.5 kW and F_{tot}=500 sccm. The lengths of the dark horizontal lines to the left of each image are representative of 1 μm. There is a clear change in film thickness and morphology when increasing $X_{C/\Sigma}$. Dividing the height of the film by 3 therefore gives growth rate (G). For fig 3.16 (a) $X_{C/\Sigma}$=0.495, G=0.3 μm/hr, for (c) $X_{C/\Sigma}$=0.5, G=0.8 μm/hr and for (e) $X_{C/\Sigma}$=0.51, G=2 μm/hr. This reflects the increase in G whilst crossing $X_{C/\Sigma}$=0.5, and increase in concentration of gas phase hydrocarbon species. There is a clear change in surface morphology moving from $X_{C/\Sigma}$=0.495 → $X_{C/\Sigma}$=0.51 which is evident when comparing fig. 3.16 (b), (d) and (f). The size of crystalline facets increases from (b)→(d)→(f), which signifies a faster growth rate, and also indicating the presence of a greater concentration of growth species i.e. CH_3 radicals. These results agree with the Bachmann diagram.

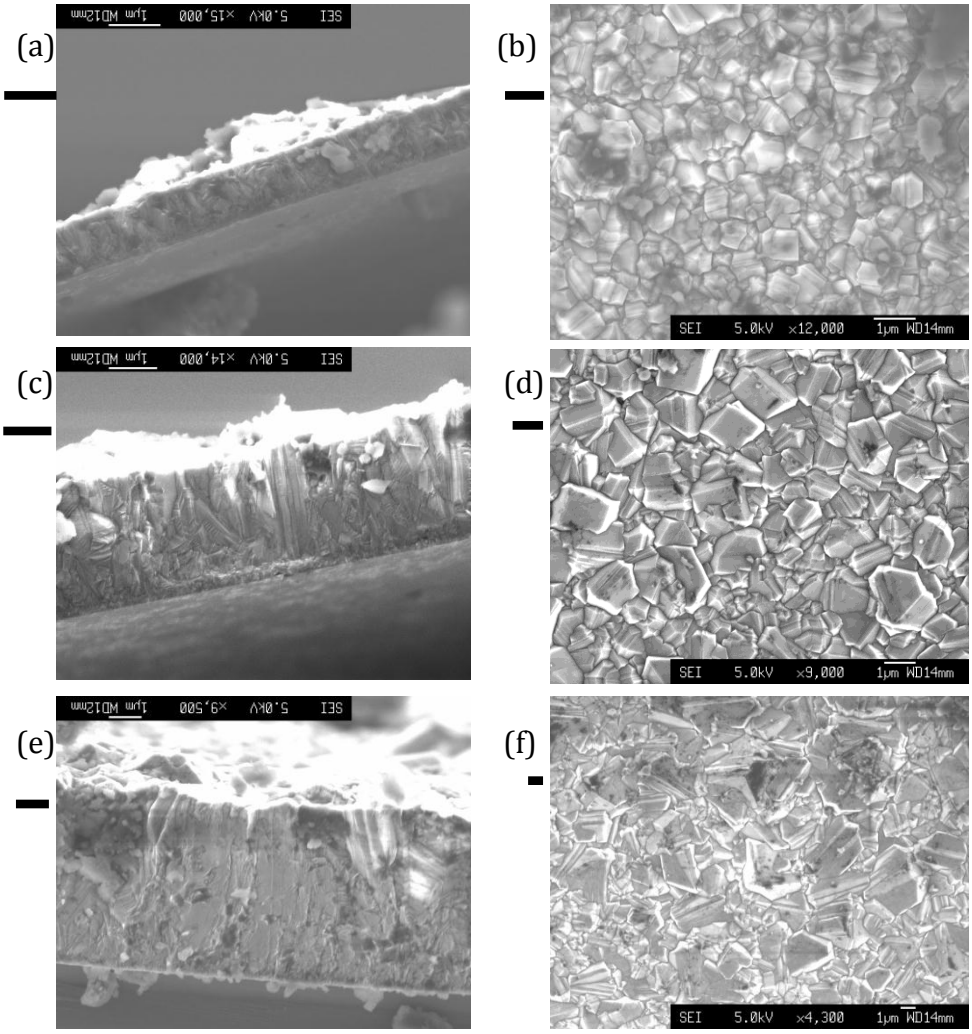

Fig. 3.16. SEM images of diamond films grown for 3 hours in a MW reactor under base conditions. Images (a)→(b) show growth when $X_{C/\Sigma}$=0.495, (c) →(d) when $X_{C/\Sigma}$=0.5, (e)→(f) when $X_{C/\Sigma}$=0.51. The lengths of the dark horizontal lines to the left of each image are representative of 1 μm.

The Raman spectra recorded for these samples are shown in fig. 3.17. The intensity of the diamond peak ($I_{Diamond}$) at 1331 cm^{-1} increases when moving from $X_{C/\Sigma}$=0.495→0.51. With increasing $X_{C/\Sigma}$, there is an increase in $I_{Diamond}$ relative to the intensity of the graphite band ($I_{Graphite}$), at ≈1550 cm^{-1}. The ratio of $I_{Diamond}$ / $I_{Graphite}$ increases with $X_{C/\Sigma}$; $I_{Diamond}$ / $I_{Graphite}$ =1.5 → 2.0 → 2.8 when moving from $X_{C/\Sigma}$=495→0.5→0.51. This indicates that although each sample contains diamond, the quality at which the film grown is greater when $X_{C/\Sigma}$=0.51. This is due to an increase in diamond growth at the surface. When considering the full width half maximum

(FWHM) of the peaks, those for $X_{C/\Sigma}$=0.495 and 0.5 are around 9.8 cm^{-1} whereas FWHM for $X_{C/\Sigma}$=0.51 is 9.0 cm^{-1}. This is indicative of a slight increase in the quality of the film grown.

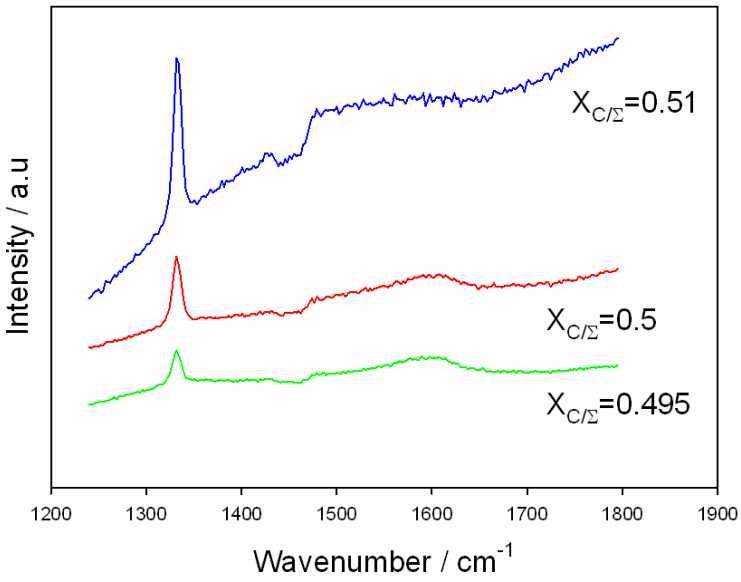

Fig. 3.17. Raman spectrum of recorded films, growing at three different $X_{C/\Sigma,}$.

Images fig. 3.18 show an attempt at growing diamond films in a CO/H_2 plasma. No diamond peaks were observed using Raman spectroscopy, and it can therefore be assumed that images (a) and (b) are of etched silicon, which was used as the substrate for the experiment.

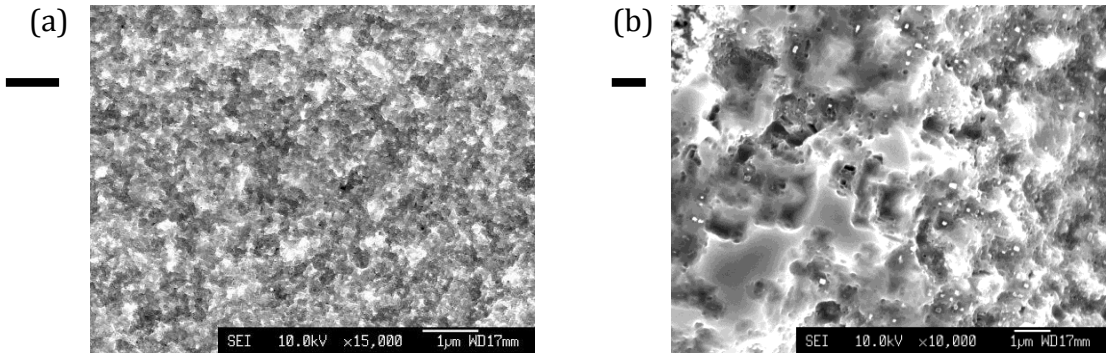

Fig. 3.18. SEM images (a) and (b) taken of diamond films grown for 3 hours in a MW reactor using a CO/H_2 gas mixture with p=150 Torr and P = 1.5 kW. The lengths of the dark horizontal lines to the left of each image are representative of 1 μm. The films were grown on silicon substrates.

3.6 Conclusions

Laser absorption spectroscopy and companion 2-D modelling have been used to investigate C/H/O plasmas under conditions appropriate for diamond CVD. The species studied exist in the hot region of the plasma, and these were: C_2(a), CH(X), OH(X) radicals and H(n=2) atoms. The chemistry prevailing in these plasmas depends strongly on the ratio of C/H/O in the feed gas, and the concentration of C_xH_y radicals in these plasmas is a strong function of $X_{C/\Sigma}$. Both modelling and experimental results show an increase in C containing radical species when $X_{C/\Sigma}$ >0.5, and an increase in O containing radical species when $X_{C/\Sigma}$<0.5, although most of the reactor is filled with H_2 and CO. The main difference between these plasmas and previously studied C/H plasmas is the presence of annular regions around the hot plasma core. Under base conditions, the centre of the plasma contains mainly CO and H_2, which are seen as the most stable end point species for reactions between H_xO and C_xH_y species. H_xO and C_xH_y species, which localise in annular regions outside the hot central core, are also seen as a source of CH and OH radicals. CH_3 radicals, as in C/H plasmas are recognized as the most abundant species in the vicinity of the growing surface,[19] and are therefore seen as being the main growth species in C/H/O plasmas.

Diamond films were grown in order to validate assumptions and conclusions drawn from the gas phase diagnostics and accompanying plasma modelling. Raman spectra were also taken. These experiments confirm the anticipated increase in growth rate and diamond quality as a result of increasing $X_{C/\Sigma.}$ Films were also grown using a CO/H_2 plasma, as column densities of CH and OH were lower than those measured in a $CH_4/CO_2/H_2$ plasma. CO/H_2 grown films were poor in comparison to those grown using $CH_4/CO_2/H_2$ plasmas, as SEM images and showed no diamond growth, and the the diamond peak on Raman spectra was non-existent. This shows a hidden subtlety in the Bachmann diagram, as it is clear that the rate and quality of diamond grown does actually depend upon the source gas, and not simply the ratio of C/O/H.

The main question to be answered from this work however, was why diamond can be grown in these C/H/O plasmas at lower input power (1kW), achieving equivalent substrate temperatures as reached in conventional C/H gas mixtures with a

substantially higher input power (1.5 kW). 2D(r,z) modelling results show that equivalent gas temperatures can be reached for successful growth due to $CH_4/CO_2/H_2$ plasmas having a lower thermal conductivity than CH_4/H_2 plasmas.

3.7 References

1. Butler, J. E., Woodin, R. L., Brown, L. M. & Fallon, P. Thin Film Diamond Growth Mechanisms. *Philos. Trans. R. Soc. A Math. Phys. Eng. Sci.* **342,** 209 (1993).

2. Kawato, T. & Kondo, K. Effects of Oxygen on CVD Diamond Synthesis. *Jpn. J. Appl. Phys.* **26,** 1429 (1987).

3. Harris, S. J. & Weiner, A. M. Effects of oxygen on diamond growth. *Appl. Phys. Lett.* **55,** 2179 (1989).

4. Balestrino, G. *et al.*. Growth of diamond films: General correlation between film morphology and plasma emission spectra. *Appl. Phys. Lett.* **62,** 879 (1993).

5. Saito, Y., Sato, K., Tanaka, H., Fujita, K. & Matuda, S. Diamond synthesis from methane-hydrogen-water mixed gas using a microwave plasma. *J. Mater. Sci.* **23,** 842 (1988).

6. Bachmann, P. K., Leers, D. & Lydtin, H. Towards a general concept of diamond chemical vapour deposition. *Diam. Relat. Mater.* **1,** 1 (1991).

7. Muranaka, Y., Yamashita, H. & Miyadera, H. Characterization of diamond films synthesized in the microwave plasmas of CO/H2 and CO/O2/H2 systems at low temperatures (403–1023 K). *J. Appl. Phys.* **69,** 8145 (1991).

8. Bachmann, P. K., Leers, D. & Wiechert, D. U. Post-depositional diamond etching. *Diam. Relat. Mater.* **2,** 683 (1993).

9. Prijaya, N. A., Angus, J. C. & Bachmann, P. K. Thermochemical computation of the diamond deposition domain. *Diam. Relat. Mater.* **3,** 129 (1994).

10. Forda, I. J., Road, P., Oxi, O. & Kingdom, U. Model of the competitive growth of amorphous carbon and diamond films. *J. Appl. Phys.* **78,** 510 (1995).

11. Marinelli, M. *et al.*. Compositional and spectroscopic study of the growth of diamond films from several gaseous mixtures. *J. Appl. Phys.* **76,** 5702 (1994).

12. Petherbridge, J., May, P. W., Pearce, S. R. J., Rosser, K. N. & Ashfold, M. N. R. Molecular beam mass spectrometry investigations of low temperature diamond growth using CO_2 / CH_4 plasmas. *Diam. Relat. Mater,* **10**, 393 (2001).

13. Petherbridge, J. R., May, P. W., Pearce, S. R. J., Rosser, K. N. & Ashfold, M. N. R. Low temperature diamond growth using CO_2 /CH_4 plasmas: Molecular beam mass spectrometry and computer simulation investigations. *J. Appl. Phys.* **89,** 1484 (2001).

14. Gries, T. *et al.*. Experimental and kinetic studies of C–H–O plasmas for polycrystalline and nano-smooth diamond deposition. *Diam. Relat. Mater.* **18,** 730 (2009).

15. Aubry, O., Delfau, J.-L., Met, C., Vandenbulcke, L. & Vovelle, C. Precursors of diamond films analysed by molecular beam mass spectrometry of microwave plasmas. *Diam. Relat. Mater.* **13,** 116 (2004).

16. Met, C. *et al.*. Emission Spectroscopy, Mass Spectrometry, and Kinetics in CH_4–CO_2 Plasmas Used for Diamond Deposition. *J. Electrochem. Soc.* **153,** F127 (2006).

17. Elliott, M. A. *et al.*. Optical emission spectroscopic studies of microwave enhanced diamond CVD using CH_4/CO_2 plasmas. *Diam. Relat. Mater.* **9,** 311 (2000).

18. Mollart, T. P. & Lewis, K. L. Optical-quality diamond growth from CO - containing gas chemistries. *Diam. Relat. Mater,* **8,** 236 (1999).

19. Kelly, M. W., Richley, J. C., Western, C. M., Ashfold, M. N. R. & Mankelevich, Y. A. Exploring the Plasma Chemistry in Microwave Chemical Vapor Deposition of Diamond from C/H/O Gas Mixtures. *J. Phys. Chem. A* **116,** 9431 (2012).

20. Mankelevich, Y. A., Ashfold, M. N. R. & Ma, J. Plasma-chemical processes in microwave plasma-enhanced chemical vapor deposition reactors operating with C/H/Ar gas mixtures. *J. Appl. Phys.* **104,** 113304 (2008).

Chapter 4 OES investigations of C/H/O plasmas

4.1 Introduction

The Bachmann diagram[1] provides the best description for optimising conditions used for growing diamond in a C/H/O plasma. The most commonly used diagnostic technique for studying these plasmas is OES. OES is a spectroscopic technique, which provides a quick and easy way to provide insight into processes occurring within the plasma with changing parameters eg. power, pressure, height and feed gas ratio.[2–5] Making sense of OES data however is complicated, and requires a proper understanding of the various possible excitation and de-excitation pathways of gas phase species. In this thesis, OES does not provide absolute number column densities as with CRDS. Instead, OES measures emissions from excited species within the plasma. Where trends in species/OES signals differ from CRDS, this can be indicative of changes in T_e and n_e, since OES requires emission from excited states, and in most cases is therefore reliant upon the overlap of n_e with number densities of selected species in their respective ground states, or the metastable 'a' state in the case of C_2. A possible reason species emission may vary from T_e and n_e, could be from the formation of excited state species, which results in chemiluminescent reactions.

Careful interpretation of OES results can give quantitative information from plasmas. Actinometry is one such method, which can be used to calculate concentrations of gas phase species such as H(n=1).[6,7,8] The role of H atoms in the CVD process is vital, and so having an understanding of how the concentration of H varies when in its ground state, whilst varying plasma parameters, is important. Actinometry works by adding a known concentration of inert tracer species such as Ar to the feed gas, then comparing the emission intensities of the actinometer versus the species of interest. The ratio of species/actinometer eg. H(n=3 →n=2)*/Ar* emission is then proportional to the species electronic ground state concentrations. Ma *et al.*[9] used actinometry to study H(n=1) densities in C/H/Ar plasmas whilst changing parameters such as

$F(CH_4)$, F(Ar), power and pressure.[9] They found that increasing power and pressure had the biggest influence in increasing the H(n=1) number densities, as the formation of H(n=1) comes primarily from the thermal dissociation of H_2.

In the sections to follow, OES has been used to follow the behavior of C_2*, CH*, CO*, Hα, Hβ and OH*. Results from OES will be compared with results from the 2D(r,z) plasma model in the previous chapter to make sense of experimental trends, and as OES results can be ambiguous, comparisons will also be made with CRDS results from chapter 3.

4.2 Experimental

The experimental set-up is slightly different from that used for CRDS in chapter 3; the reactor side arms are removed, and replaced with diamond windows. Emissions from the plasma are collected through a two lens telescope as shown in fig. 4.1, and are focused onto the end of a quartz optical fibre. The light then exits the optical fibre as a vertical stripe, where it is dispersed through a monochromator equipped with a charged couple device (CCD) strip detector, which provides a spectral resolution <1 nm. The diffraction grating in the spectrometer is set at two positions to record emission lines in the UV and visible regions, over a range of 300 nm. The CCD detector was cooled to around -10 ^{o}C in order to reduce background noise. The spatially resolved data is collected with an exposure time of 0.5 seconds, through 64 accumulations.

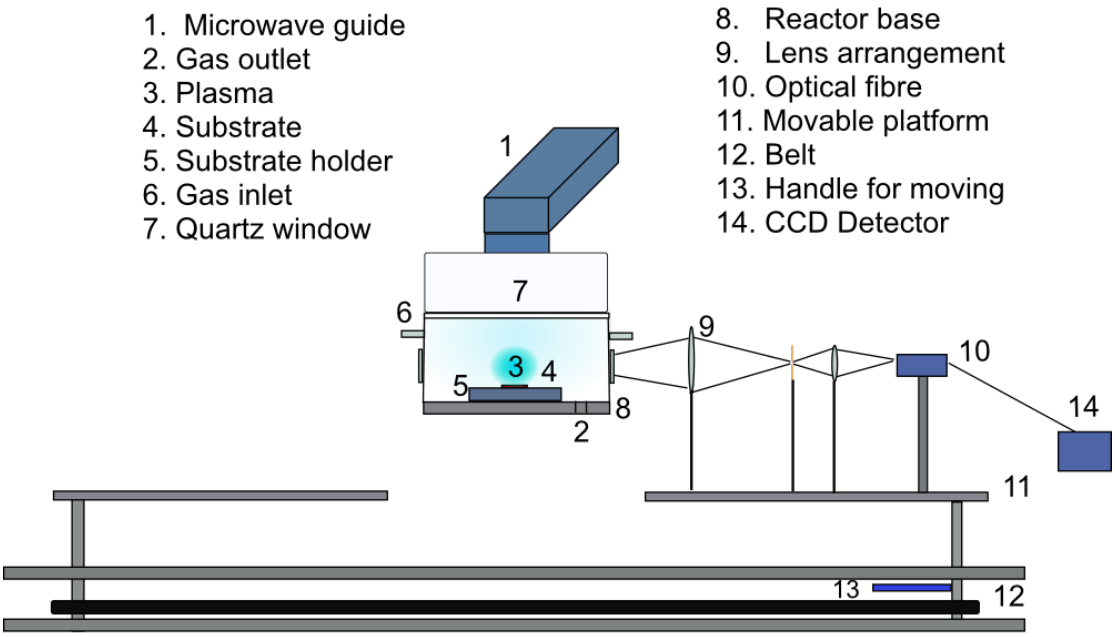

Fig. 4.1 OES reactor design

4.3 Typical OES spectra from a C/H/O plasma

Examples of spectra recorded with increasing $X_{C/\Sigma}$ are shown in fig. 4.2, with data recorded from $CH_4/CO_2/H_2$ plasmas, where $X_{C/\Sigma}$ =0.46, 0.495 and 0.54, and $X_0(H_2)$=0.3. Prominent features of these spectra are: lines from the C_2 Swan band system ($d^3\Pi_g$-$a^3\Pi_u$) at 516 nm; CH ($A^2\Delta$-$X^2\Pi$) at 432nm ; OH ($A^2\Sigma^+$-$X^2\Pi$) at 306nm ; C_3($A^1\Pi_u$-$X^1\Sigma_g$) at 405 nm; the CO Angstrom ($B^1\Sigma^+$-$A^1\Pi$) and 3rd positive system at ($b^3\Sigma$-$a^3\Pi$); as well as H Balmer-α and H Balmer-β emissions. It is clear from the OES data shown in fig. 4.2 that there is a clear decrease in emission from CO* and OH*, and increase in emissions from C_2*, CH* and C_3* with increasing $X_{C/\Sigma}$. The following discussion compares OES data with model results, and CRDS results from chapter 3 to make sense of observed trends. Base conditions for the OES measurements were the same as described for the CRDS measurements in chapter 3.2.

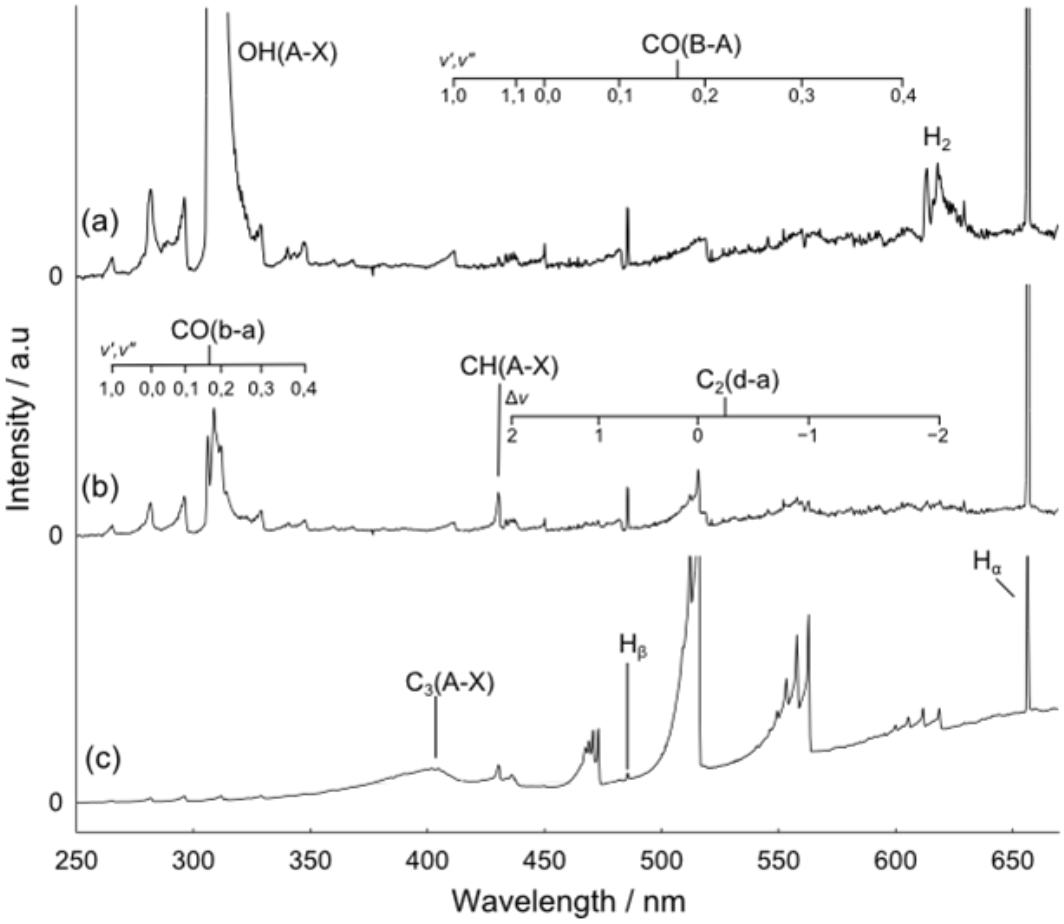

Fig. 4.2. OES spectra from $CH_4/CO_2/H_2$ plasmas, where $X_{c/\Sigma}$=(a) 0.46, (b) 0.495, (c) 0.54. $X_0(H_2)$=0.3, at z=10 mm.

4.4 Results and discussion for OES Results

Emissions from CO*, C_2*, C_3*, OH*, and H(n=3) were profiled at three different values of $X_{C/\Sigma}$, and these spatial profiles are shown in fig. 4.3. All the data has been displayed so that the peak intensity from each emitting species has been normalized to unity. One common feature seen at each $X_{C/\Sigma}$ value is the z-dependent variation in the peak of the different species distributions. Emissions from CO* peak lowest in the plasma at around z=5 mm, followed by emission from H(n=3) at around z=7 mm. C_2*, C_3*, and OH* peak highest in the plasma, at z=10 mm. Model results predict that CO is one of the most abundant species in the plasma, and is distributed throughout the reactor. CO will therefore exist more in cooler regions than in hotter regions within the plasma. This is because it will diffuse away from hotter regions towards cooler regions of lower energy and explains emissions from CO at lower z than other

species. H Balmer-α emission will be a convolution of where the electron density is greatest, and where the plasma is hottest; dissociation of H_2 is primarily a thermally driven process forming H(n=1), which has to be further excited to H(n=3), where ΔE (n=3←n=1) = 12eV, before emitting to the H(n=2) level at 656 nm. Emissions from C_2*, C_3*, and OH* maximise in the hottest region of the plasma at z=10 mm as their formation is driven by thermal chemistry. According to the 2D(r,z) model, as described in chapter 3, n_e increases from the substrate to z=3 mm then remains relatively flat, decreasing at around z=13 mm. In profile (b) where $X_{C/\Sigma}$ = 0.495 however, emissions from CH* and C_2* expand to z>13 mm. Chemiluminescent reactions forming CH* and C_2* explain emission from these species in regions where there are no electrons to explain their excitation.[2]

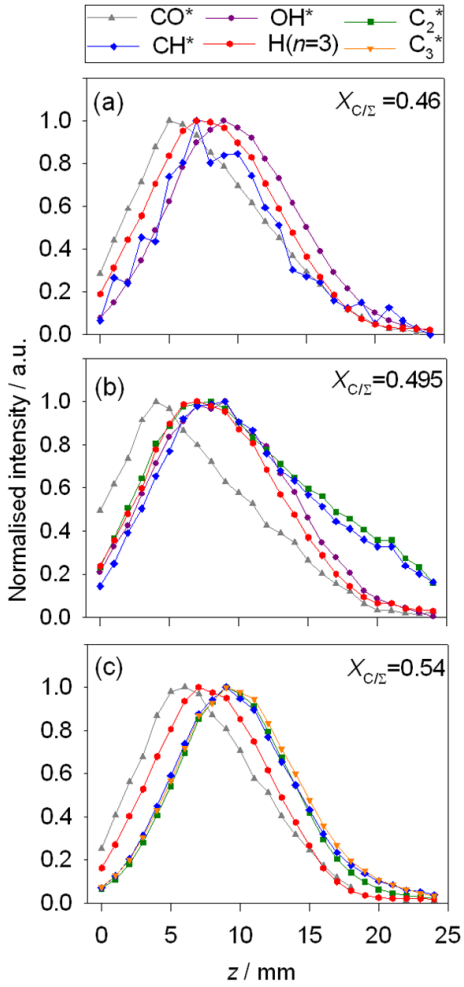

Fig. 4.3. Spatial profiles of CH*, C_2*, C_3*, OH*, CO* and H(n=3)*, at $X_{C/\Sigma}$= (a) 0.46, (b) 0.495 and (c) 0.54, where $X_0(H_2)$=0.3. The peak intensity of each species in the plots has been normalized to unity.

Changes in species emission with varying $X_0(H_2)$ are shown in fig. 4.4. The purpose of plots (a)→(e) is to show changes in the shape of the distribution displayed by emitting species H(n=3), CO*, OH*, CH* and C_2* at three different values of $X_0(H_2)$: 0.3, 0.6 and 0.95. The trends seen in (a)→(e) with regards to species emission with increasing $X_0(H_2)$ are shown in figure (f), and so plots (a) to (e) will only be referred to when considering the distribution of emitters.

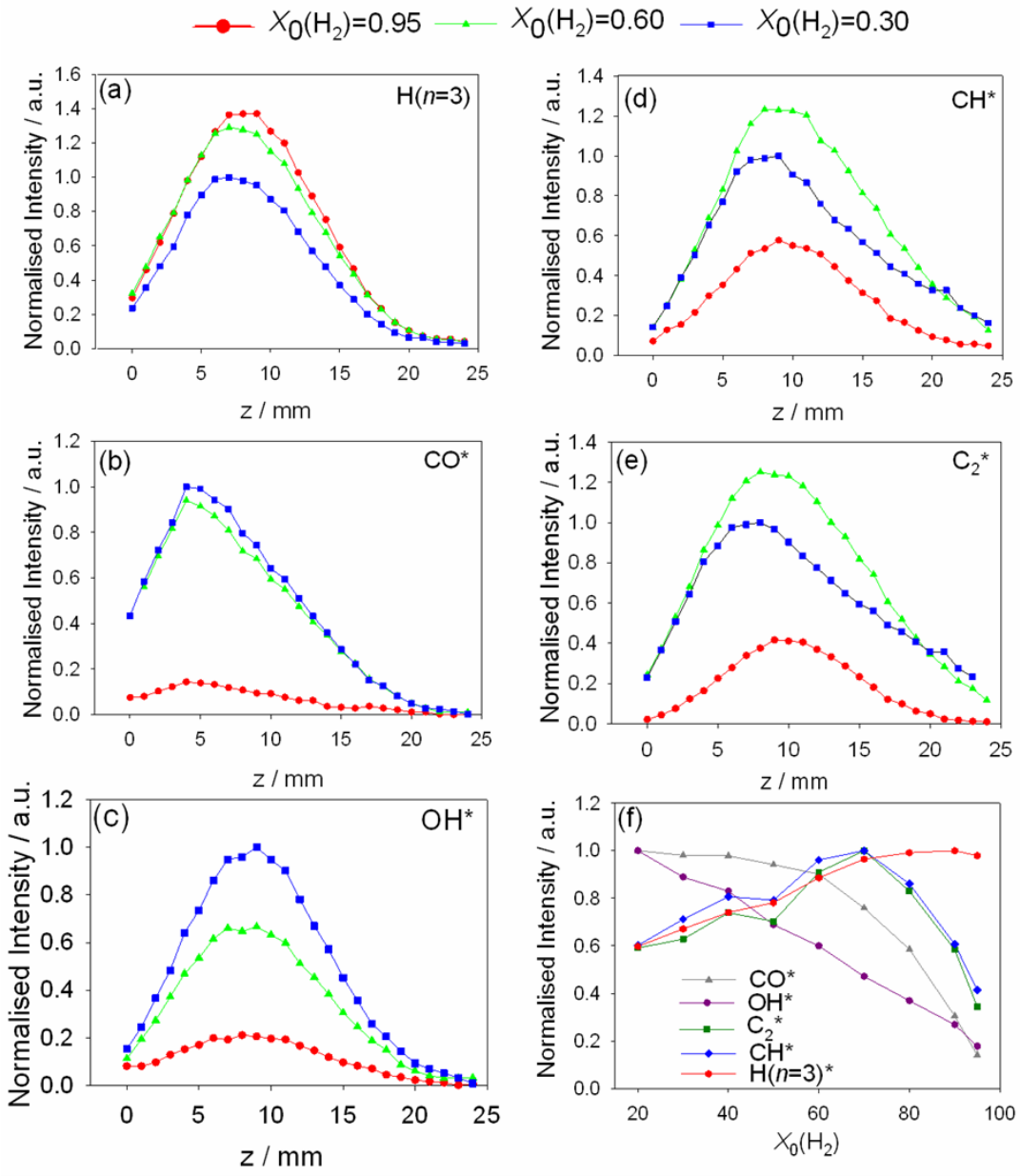

Fig. 4.4. Spatial profiles of emissions from: (a) H(n=3)*, (b) CO*, (c) OH*, (d) CH*, (e) C_2* normalized to unity with $X_{C/\Sigma}$= 0.495 and $X_0(H_2)$=0.95, 0.6 and 0.3. Plot (f) shows species emission from CH*, C_2*, C_3*, OH*, CO* and H(n=3) with increasing $X_0(H_2)$ at z=10mm, and base p and P.

With increasing $X_0(H_2)$, emissions from CH* and C_2* follow the same trends, and have the same spatial profiles. Emissions from C_2* and CH* increase gradually from $X_0(H_2)$=0.2→ $X_0(H_2)$=0.7 then decrease steeply towards $X_0(H_2)$=0.95. The 2D(r,z) model predicts that with increasing $X_0(H_2)$, T_e increases from 1.06 eV to 1.15 eV, and n_e more than doubles from 1.4 x 10^{11} to 3 x 10^{11} cm^{-3}. With regards to all emitting species, the spatial overlap between their respective ground states and the electron density distribution will determine the distribution of their emissions. It is partly for this reason that C_2* and CH* emissions decrease after $X_0(H_2)$=0.7; emissions increase with increasing T_e and n_e, but when $X_0(H_2)$ moves from 0.7→ 0.95 the plasma becomes more reminiscent of C/H plasmas and the peak in the electron density moves from r=2 mm to r=0 mm. The shift in [CH] and [C_2] moves from around the plasma edge at r=3.5 to r=0 in increasing $X_0(H_2)$,[2] fig. 4.4 (f) suggests that the best overlap between [CH] and [C_2] with n_e is at $X_0(H_2)\leq 0.7$. The other reason for the decrease in CH* and C_2* at high $X_0(H_2)$ is that with increasing $X_0(H_2)$, $X_0(C)$ in the plasma decreases, and [CH] and [C_2] decrease as shown in CRDS in chapter 3. With regards to the shape of CH* and C_2* distributions, in (d) and (e), it is clear that this is becoming broader from $X_0(H_2)$=0.3→0.95 which is a result of the increase of electron density and its distribution, since modelling results show that n_e moves from the peripheral regions of the plasma, to forming a ball shaped distribution in the centre.[2]

Emissions from OH* and CO* increase with decreasing $X_0(H_2)$. With regards to OH, considering the reaction OH + H_2 ↔ H_2O + H, this means that:

$$[OH] \approx \frac{[H]}{[H_2]}[H_2O] \qquad (4.1)$$

The above equation implies that [OH] should increase with decreasing [H_2], which does happen. However, the decrease in $X_0(H_2)$ from 1.0→0.2 should only create a 2-fold increase as seen in CRDS, and not a 5-fold increase as seen in emission. The fact that CO* emissions are also increasing with decreasing $X_0(H_2)$ implies that there may be an increased concentration of low lying excited states of CO, specifically the metastable $a^3\pi$ state since, as mentioned in chapter 3, the model predicts that 17.5% of the absorbed power goes into the CO ($a^3\pi \leftarrow X^1\Sigma^+$) transition. Quenching reactions between OH(X) and CO($a^3\pi$), as well as H atoms could account for the higher than

predicted emissions from OH* when compared to CRDS results. The CO distribution in the spatial profiles is about the same for $X_0(H_2)$=0.3 and 0.6, but is again broader for $X_0(H_2)$=0.95 due to the shift increase in electron density and electron density into the plasma centre. The decrease in both CO* and OH* emissions could also be due to the decrease in $X_0(O)$ with increasing $X_0(H_2)$ in the feed gas.

H(n=3) emissions increase in fig. 4.4 (f) as is to be expected with increasing $X_0(H_2)$. As with emission from all other species, the H(n=3) distribution of emissions in the spatial profiles becomes broader with increasing $X_0(H_2)$, which is indicative of a broadening of the n_e distribution.

Emissions for increasing $X_{C/\Sigma}$ at three different $X_0(H_2)$ values are shown in Fig. 4.5. These are in good accord with CRDS results.

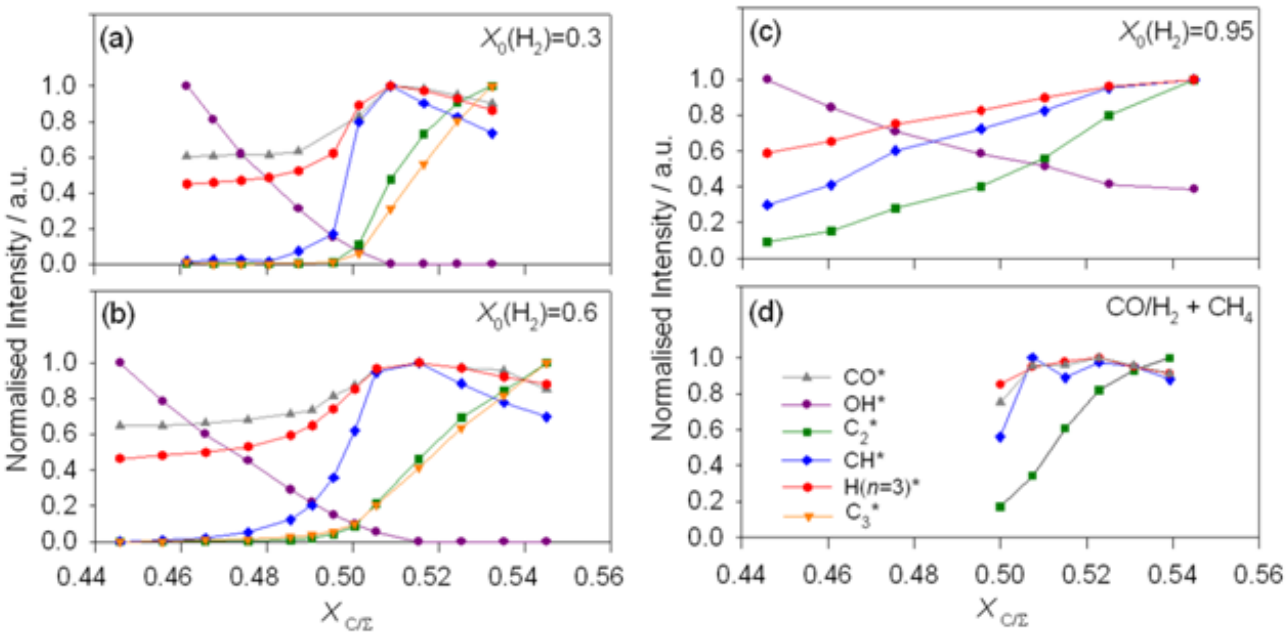

Fig. 4.5. Emission intensities from CH*, C_2*, C_3*, OH*, CO* and H(n=3) with increasing $X_{C/\Sigma}$, at $X_0(H_2)$= (a) 0.3 (b) 0.6 and (c) 0.95 at base p and P and z=10mm. Plot (d) shows a 41.2% CO/58.8% H_2 plasma increasing $X_{C/\Sigma}$ by progressively replacing CO by CH_4.

It is clear from fig. 4.5 that increasing $X_{C/\Sigma}$ results in an increase in emissions from carbon containing species: C_2*, CH* and C_3* with a slight increase in emissions from CO*, and a decrease in emissions from OH*. As shown in figs. 3.14 and 3.15 from the previous chapter, increasing $X_{C/\Sigma}$ results in an increase in the column densities of hydrocarbon species, and changes in their distribution i.e. CH and C_2 distributions

move from an annular region around the hot plasma region and into the center of the plasma. With increasing $X_0(H_2)$ from 0.3→0.6→0.95 the increase in C_2*, C_3* and CH* becomes much less sensitive to $X_{C/\Sigma}$. This is due to the shrinking of the plasma size with increasing $X_0(H_2)$ which results in the incomplete mutual conversion of C_xH_y and H_xO species into CO. This means that when $X_0(H_2)$=0.95 the immediate increase in C_xH_y species is not observed when crossing $X_{C/\Sigma}$=0.5 as when increasing $X_{C/\Sigma}$ at $X_0(H_2)$=0.3.

Fig 4.5 (d) shows emissions from CO*, CH*, C_2* and H(n=3) with increasing $X_{C/\Sigma}$ in a CO/H_2 plasma. These plasmas have been discussed in greater detail in chapter 3, using CRDS results. $X_{C/\Sigma} \geq 0.5$ since CO is the C and O source. $X_{C/\Sigma}$ was increased by successively replacing CO with CH_4 in the reactor. Due to the stability of CO in the plasma, and the difficulty in breaking the CO bond, emissions from OH* were immeasurable, and those from C_2* and CH* only increased with the addition of CH_4 into the reactor, which can be seen with an immediate increase in CH* emissions and a near linear increase in C_2* emissions.

Changes to species emissions when varying power and pressure are shown in fig. 4.6. When considering changes in pressure, there is an increase in T_{gas} with a decrease in T_e.[9,10] Changes in species emission and distribution with increasing p can be seen in fig. 4.6 (a)→(c). These differ somewhat with CRDS results. CRDS plots in fig. 3.13 show an increase in C_2 column density and a decrease in H(n=2) column densities with increasing p, whereas emission from C_2* and H(n=3)* both decrease with increasing pressure. This is most likely attributable to the overall decrease in T_e with increasing pressure.[9] That emission from CH*, C_2*, CO* and H(n=3)* should decrease, yet those from OH* should increase with increasing p reflects the fact that emission from these excited radicals and atoms is determined by the overlap between them and n_e, especially since OH column densities in CRDS show little changes in species distribution, as in fig. 3.13. In addition to this, the distribution of C_2* and CH* in (a) and (b) is indicative of a shift of the hot plasma region to lower z. Both C_2* and CH* emissions move from z=10 mm to around z=8 mm, which is representative of a decrease in the plasma size with increasing pressure. The extended distribution of C_2* and CH* in 4.6 (a) can again be attributed to the formation of these species by chemiluminescent reactions.

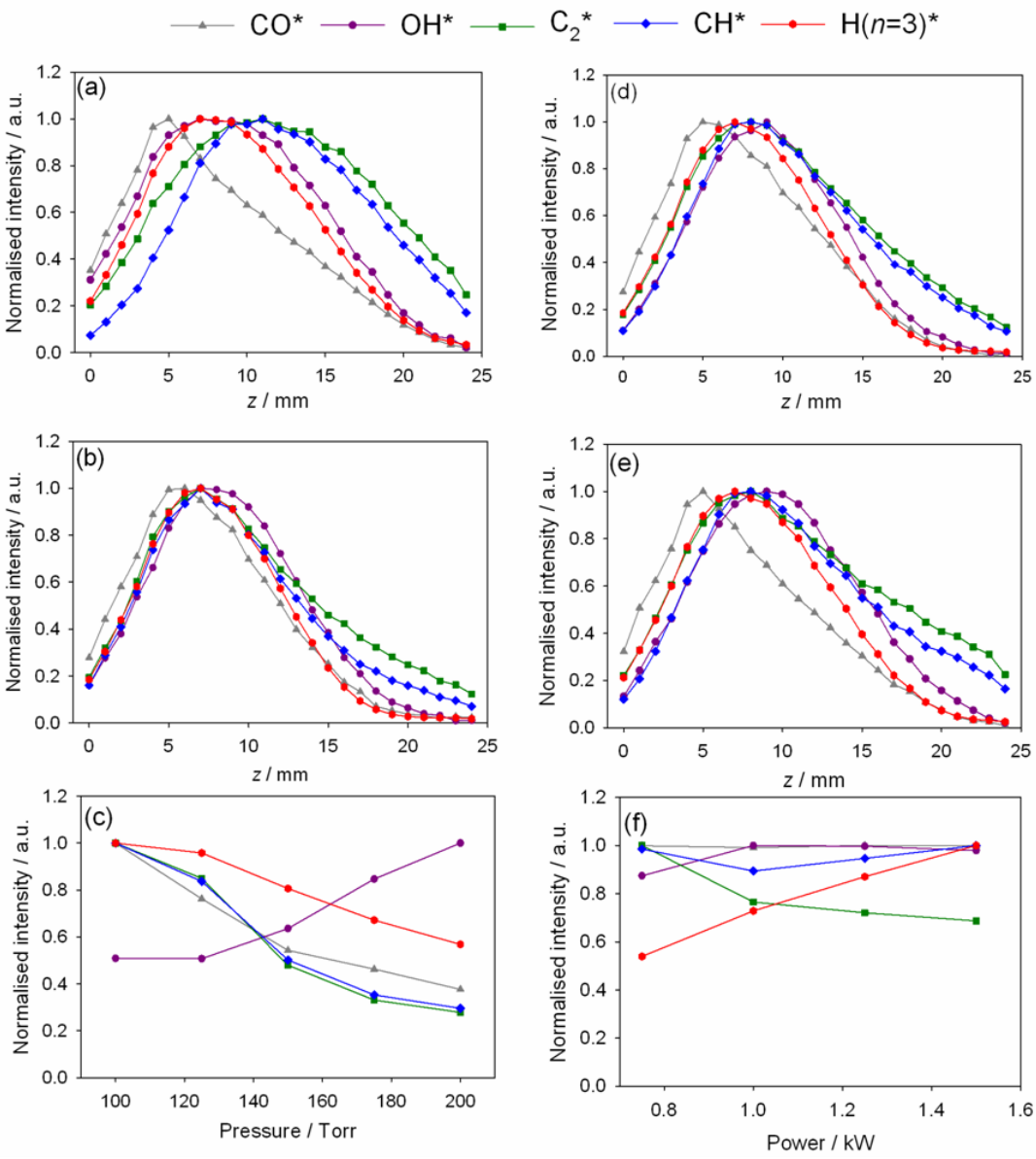

Fig. 4.6 Emission intensities from CH*, C_2*, C_3*, OH*, CO* and H(n=3) with increasing power and pressure. Plots (a), (b) are profiles taken at 100 and 200 Torr, and (c) shows trends in species emission with increasing p, where P=1.5 W, $X_{C/\Sigma}$= 0.495, $X_0(H_2)$=0.3 and z=10 mm. Plots (d) and (e) are profiles taken at0.8 and 1.4 kW, and (f) shows trends in species emission with increasing P, where p=15o Torr, $X_{C/\Sigma}$= 0.495, $X_0(H_2)$=0.3 and z=10 mm.

The effect of increasing P on species emission and distribution can be seen in fig. 4.6 (d)→(f). Increasing P causes an increase in the plasma power density,[10] Q, which means that more energy is consumed per unit time. When comparing CRDS results from fig. 3.13 (a) with fig 4.6 (f) there are clear differences. The observed changes in species emissions which are most obvious comes from the 2-fold increase in H(n=3)*,

and the 30% decrease in C_2* emission. CRDS results agree with the increase in H(n=2) column density, however the column density of C_2 increases. There is little change in OH* and CH* emission in OES, yet in CRDS there is a clear increase in CH and decrease in OH column densities. This difference between OES and CRDS results is yet again a reminder of the overlap required of selected species, and n_e if the excitation and emission from gas phase radicals and atoms is to match the trends given by their distribution in CRDS.

4.5 Conclusions

OES has proved a useful tool in investigating $CH_4/CO_2/H_2$ and CO/H_2 plasmas under conditions relevant to diamond CVD. Emissions from OH*, CO*, C_2*, C_3*, CH* radicals, H(n=3)* atoms and CO* molecules were recorded from the hot plasma region whilst varying plasma parameters.

When studying trends in species emission, it is clear that the excitation of species is dependent upon the overlap where number densities of ground state species are greatest, and n_e. Emission from OH* was is inconsistent with CRDS results with decreasing $X_{C/\Sigma}$, and this was attributed to energy exchange reactions between OH(X) and metastable CO($a^3\pi$). Since emission from H(n=3)* gives the best estimation of the electron density distribution, when C_2 and CH* deviate from this trend, emission from these species comes from chemiluminescent reactions. As with CRDS, results show a clear dependence of plasma composition to $X_{C/\Sigma}$ where emissions from C containing species increased, and those from OH decreased with increasing $X_{C/\Sigma}$. This again highlights the conditions which must be met in order to successfully grow films with C/H/O plasmas, with $X_{C/\Sigma}$ >0.5, although $X_{C/\Sigma}$ should not be too high, as this may need lead to graphitic impurities on grown films, as will be discussed in Chapter 6.

4.6 References

1. Bachmann, P. K., Leers, D. & Lydtin, H. Towards a general concept of diamond chemical vapour deposition. *Diam. Relat. Mater.* **1,** 1 (1991).

2. Richley, J. C., Kelly, M. W., Ashfold, M. N. R. & Mankelevich, Y. A. Optical emission from microwave activated C/H/O gas mixtures for diamond chemical vapor deposition. *J. Phys. Chem. A* **116,** 9447 (2012).

3. Bénédic, F. *et al.*. Spectroscopic Diagnostics of Pulsed Microwave Plasmas used for Nanocrystalline Diamond Growth. *Chem. Vap. Depos.* **14,** 173 (2008).

4. Ma, J., Richley, J. C., Davies, D. R. W. & Ashfold, M. N. R. Spectroscopic and modelling investigations of the gas phase chemistry and composition in microwave plasma activated $B_2H_6/CH_4/Ar/H_2$ mixtures. *J. Phys. Chem. A* **114,** 10076 (2010).

5. Elliott, M. A. *et al.*. Optical emission spectroscopic studies of microwave enhanced diamond CVD using CH_4/CO_2 plasmas. *Diam. Relat. Mater.* **9,** 311 (2000).

6. Gicquel, A., Chenevier, M., Hassouni, K., Tserepi, A. & Dubus, M. Validation of actinometry for estimating relative hydrogen atom densities and electron energy evolution in plasma assisted diamond deposition reactors. *J. Appl. Phys.* **83,** 7504 (1998).

7. Abdel-Rahman, M., Gathen, V. S. der, Gans, T., Niemi, K. & Döbele, H. F. Determination of the degree of dissociation in an inductively coupled hydrogen plasma using optical emission spectroscopy and laser diagnostics. *Plasma Sources Sci. Technol.* **15,** 620 (2006).

8. Coburn, J. W. & Chen, M. Optical emission spectroscopy of reactive plasmas: A method for correlating emission intensities to reactive particle density. *J. Appl. Phys.* **51,** 3134 (1980).

9. Ma, J., Ashfold, M. N. R. & Mankelevich, Y. A. Validating optical emission spectroscopy as a diagnostic of microwave activated $CH_4/Ar/H_2$ plasmas used for diamond chemical vapor deposition. *J. Appl. Phys.* **105,** 043302 (2009).

10. Mankelevich, Y. A., Ashfold, M. N. R. & Ma, J. Plasma-chemical processes in microwave plasma-enhanced chemical vapor deposition reactors operating with C/H/Ar gas mixtures. *J. Appl. Phys.* **104,** 113304 (2008).

Chapter 5 CRDS and OES investigations of N containing plasmas

5.1 Introduction

Nitrogen has proved to be an important addition to the process gas mixture for growing and doping synthetic diamond. The role of nitrogen in the growth of polycrystalline diamond (PCD), single-crystalline diamond (SCD) and ultrananocrystalline diamond (UNCD) films has been studied extensively.[1,2] Not only can the presence of nitrogen increase diamond growth rate[3] and favour the growth of the (100) reconstructed surface morphology,[4,5] it can also increase the electrical conductivity of UNCD films.[6–9] This introduction includes a review of gas phase diagnostics of nitrogen containing plasmas and the effect this can have on growth and properties of diamond. The mechanisms involved for N incorporation and possible structures of N inclusion within diamond will be discussed in Chapter 6.

Knowing the distribution of key radical species in the plasma is crucial to fully understanding the diamond growth process and the chemistry occurring just above the growing surface. Vandevelde *et al.* used OES to give a qualitative description of changes in species emission within the plasma with increasing N_2 in the $N_2/CH_4/H_2$ feed gas.[10–12] They report results as the intensity of emissions from radical species C_2, CH and CN as ratios I_{CH}/I_{C_2} and I_{CN}/I_{C_2}, and find that with increasing ppm of N_2 from 0→600, I_{CN}/I_{C_2} increases linearly, yet there is no change in I_{CH}/I_{C_2}. Alongside this, they note a 7 fold increase in the growth rate, and change in film morphology from (111) to (100) when increasing from 0 to 600 ppm N_2 content. Over several studies, Vandevelde *et al.* [10–12] attribute the increase in G to either surface reactions with CN acting as a catalyst to growth, or simply due to an increase in key growth species, such as CH_3, close to the growing surface. Chatei *et al.*[5] also use species emission to study changes within the plasma with varying parameters. This group used species emissions and actinometry to obtain quantitative number densities of CN and CH in C/H/N plasmas. Increasing N_2 until it reached up to 18% of the input feed gas,[5] actinometry returned results showing a linear increase in CN number densities with

increasing $\%N_2$, in agreement with Vandevelde *et al.*.[12] Using Raman spectroscopy, they summarize that film quality increases up to 400 ppm N_2, then decreases. The decrease in quality is evident due to an increase in sp^2 carbon from the sp^2 Raman peak at 1550 cm^{-1}.[5] In a similar study,[13] Chatei *et al.* stoped the flow of N_2 into their reactor. When doing this, they measured an increase in H(n=1) and CH number density, and speculate that CH must be involved in the formation of CN. These studies by the Vandevelde and Chatei groups have shown how diagnostic studies of species within plasmas for diamond CVD are useful in giving insight into which species may be responsible for growth, and changes in surface morphology when including N in the process gas mixture.

It is valuable to understand the gas phase chemistry in diamond CVD when there is an increase in G to enable potential advancements in the growth process. However, many studies with the primary focus to increase G do not include plasma diagnostics. The drive to increase G is to decrease cost, and any cost effective improvements such as the addition of small amounts of N_2 to the gas mixture have great value commercially. SCD is the purest form of synthetic diamond grown industrially, and the purity is important.[14,15] Grain boundaries/defects within the diamond can decrease properties such as thermal conductivity and optical transparency. Very high growth rates can be achieved for SCD diamond with the addition of nitrogen.[1,2] Yan *et al.*[1] report that the addition of 1-5% N_2/CH_4, can triple growth rates, varying from 50 to150 μm/h. As mentioned, high growth rates with minimal substitutional defects are preferred, however, N will incorporate into the diamond lattice as a defect, which in many applications could be a small price to pay for the huge increase in growth rate achieved. Yan *et al.* found less N defects at higher temperatures, and attribute this to the migration of N on the surface and the formation of N aggregates, which increases surface roughness, which is in agreement with other studies.[16,17]

As well as having an effect on the surface structure of films, nitrogen incorporation within grown diamond can change its properties. The addition of N to the growth environment has been known to increase electrical conductivity when growing UNCD films. In 2001 Achatz *et al.* grew UNCD diamond with the incorporation of nitrogen, where n-type conductivity was observed.[6] Achatz *et al.* agree with Zapol *et al.*[9], and find that quasi-metallic behavior observed in heavily doped films cannot be due to

variable range hopping between incorporated N atoms, and is mainly due to increased π-π* delocalization, and overlap of the wavefunctions of sp^2 bonded C atoms found in grain boundaries. Birrell *et al.*[18] also confirmed this, finding that N preferentially adsorbs into grain boundaries in UNCD films due to an increased local disorder, which results in an increase of sp^2 bonded carbon atoms in these regions.

From the studies in this brief review, it is clear that the addition of N_2 into the diamond growth environment has a clear effect on not only the rate of growing films, but also favors (100) growth over (111). However, the main species responsible for N incorporation is yet unknown, and the gas phase not fully understood. The following section provides a thorough description, both quantitative and qualitative, of how changing plasma parameters, such as the ratio of input feed gases, pressure and power, etc, can alter the distribution of key radical species in the hot plasma region within a microwave reactor. Experiments were run with using both NH_3 and N_2 as the N source, however N_2 is of greater interest industrially as it is both cheaper and safer to use.

5.2 CRDS investigations

5.2.1 Experimental

The MW reactor design and experimental set-up is the same as that described in section 3.2 and in fig. 3.3. In the present study, C_2, CH, H(n=2), NH and CN are monitored using CRDS via the following transitions: C_2 ($d^3\Pi_g$-$a^3\Pi_u$); CH($A^2\Delta$-$X^2\Pi$); H(n=2), NH($A^3\Pi$-$X^3\Sigma$) and CN($B^2\Sigma$-$X^2\Sigma$). Since there were additional CH($B^2\Sigma$-$X^2\Pi$) peaks in the CN spectra recorded under certain conditions, these were also used to calculate column densities at several points to validate the standard CH($A^2\Delta$-$X^2\Pi$) peaks used. The dyes used for NH($A^3\Pi$-$X^3\Sigma$) and CN($B^2\Sigma$-$X^2\Sigma$) measurements were: LDS 698, doubled with a potassium dihydrogen phosphate (KDP) crystal and Exalite 389.

Base conditions for this work were: p=150 Torr, P = 1.5 kW, F(tot) = 500 sccm. There were, however variations for F in base conditions, dependent upon which species was being measured. For N_2/H_2 and NH_3/H_2 plasmas: F(N_2)= 3sccm, (12000 ppm N), F(NH_3)=3 sccm, (6000 ppm N) and F(H_2)=497 sccm, unless stated otherwise. For N/C/H plasmas NH and H(n=2) data were plotted separately from CN, CH and C_2 plots due to the difficulty in recording NH spectra at high F(CH_4), which was required to record successful spectra for C containing species. For $N_2/CH_4/H_2$ and $NH_3/CH_4/H_2$ plasmas, when measuring NH and H(n=2): F(N_2/NH_3)=3 sccm, F(CH_4)=2 sccm and F(H_2)=495 sccm, unless stated otherwise. For $N_2/CH_4/H_2$ and $NH_3/CH_4/H_2$ plasmas, when measuring CH, CN and C_2: F(N_2/NH_3)=3 sccm, F(CH_4)=20 sccm and F(H_2)=477 sccm, unless stated otherwise.

5.2.2 Recorded CRDS spectra

The regions of spectra for C_2, CH and H(n=2) species are as described in section 3.3.1. NH spectra were recorded to determine NH column densities using the calculation described in section 3.3.2. The band head in the NH(A-X, 0,0) band is a set of overlapped Q branch transitions peaking at 29753 cm^{-1}. However, a section of

the most accessible unblended transitions are shown in fig. 5.1. These lines are P branch transitions from J levels 9 and 10. The closeness in energy of these initial J levels does not allow for an estimation of T_{gas} from recorded spectra.

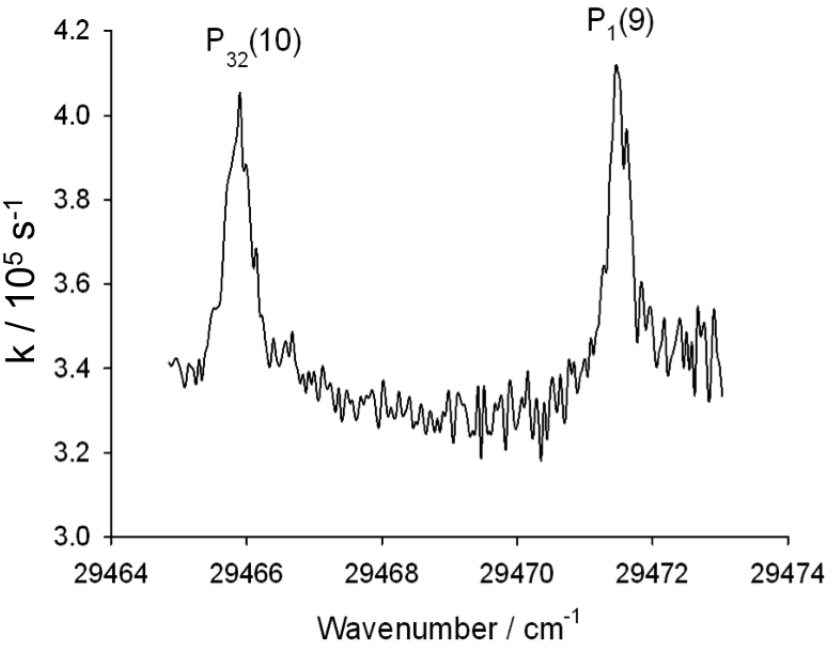

Fig. 5.1 Portion of the NH($A^3\Pi$-$X^3\Sigma$) (0,0) spectrum recorded by CRDS.

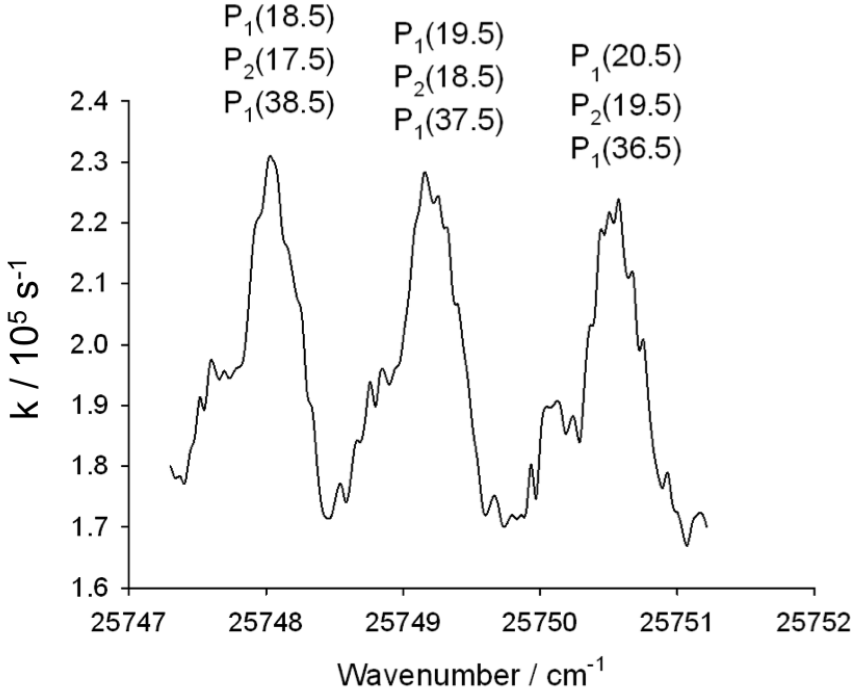

Fig. 5.2 Part of the CN ($B^2\Sigma$-$X^2\Sigma$) (0,0) spectrum recorded by CRDS.

The region of the CN ($B^2\Sigma$-$X^2\Sigma$) 0,0 band chosen for study is shown in fig. 5.2. The (0,0) band head for this transition is at 25773 cm^{-1}. Each line measured is a convolution of three P branch transitions from high J levels.

When measuring CN spectra, additional lines were observed. After careful consideration, these were attributed to the CH ($B^2\ \Sigma$-$X^2\ \Sigma$) (0,0) transition. Additional pgopher calculations were performed for the CH ($B^2\Sigma$-$X^2\Sigma$) (0,0) band. Part of the CH spectrum recorded is shown in fig. 5.3. The two peaks measured are R branch transitions.

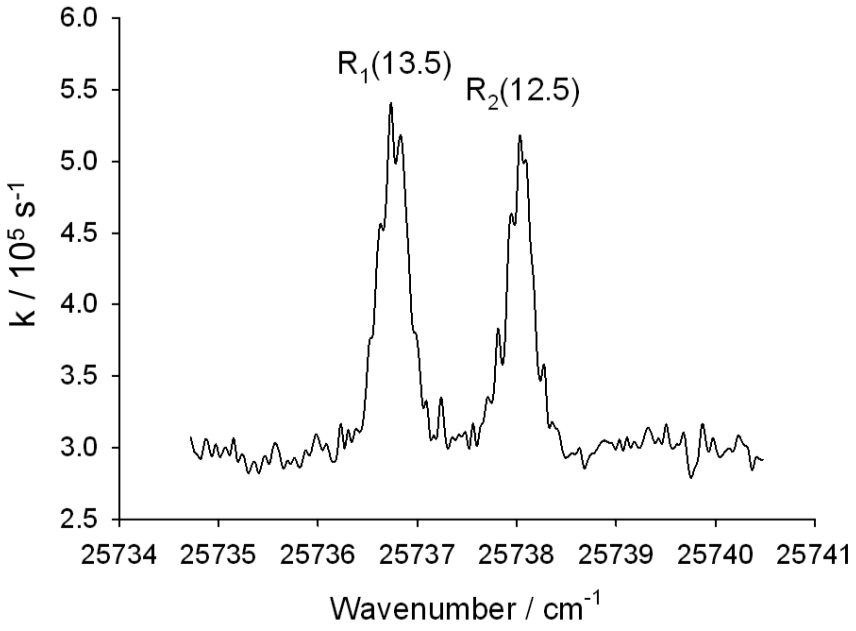

Fig. 5.3 Part of CH ($B^2\ \Sigma$-$X^2\ \Sigma$) (0,0) spectrum recorded by CRDS.

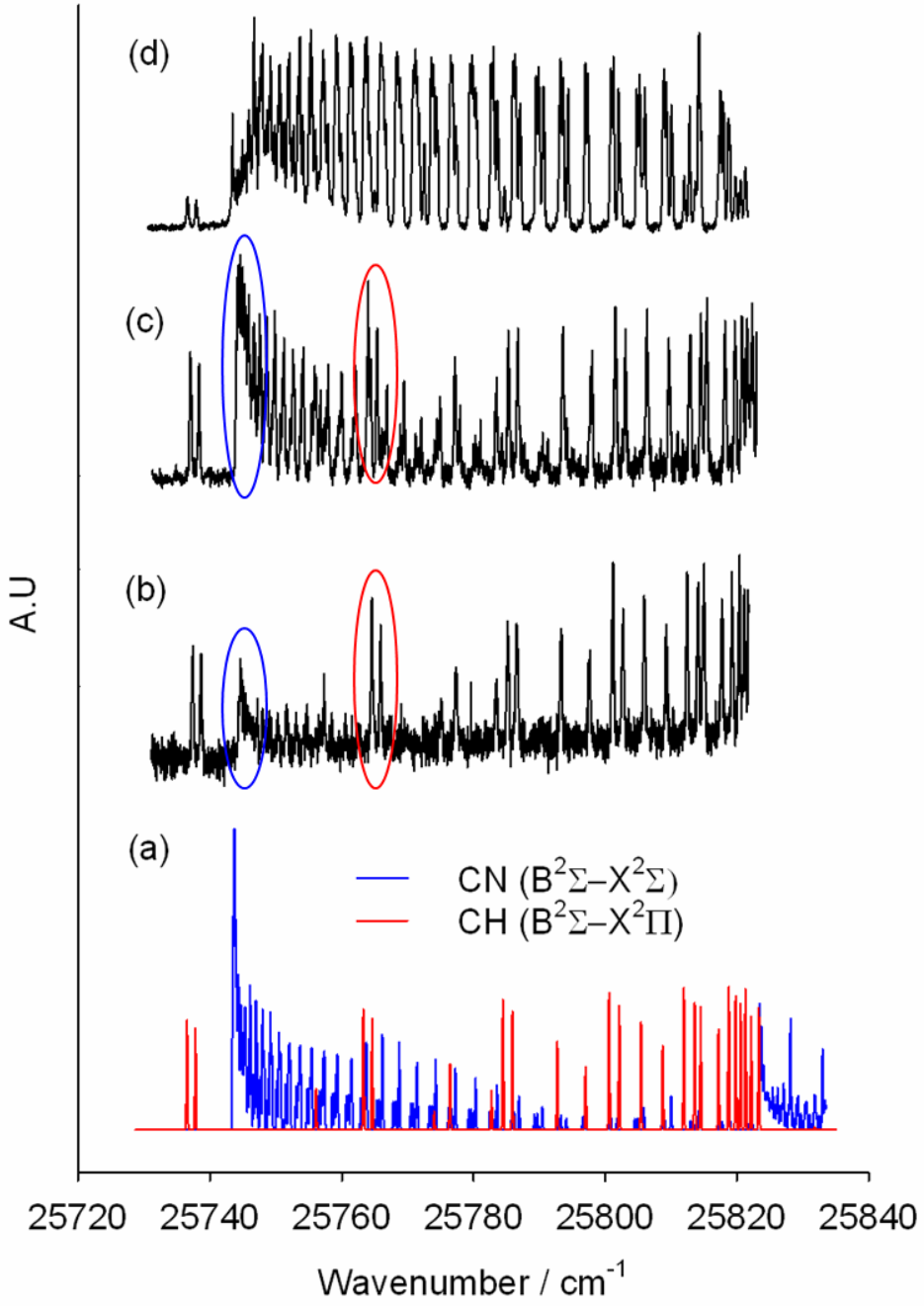

Fig. 5.4. Overlap of CN ($B^2\Sigma$-$X^2\Sigma$) (0,0) with CH ($B^2\Sigma$-$X^2\Sigma$) (0,0) transitions. Plot (a) is a Pgopher[19] simulation showing the overlap between CH and CN. The CN spectrum is blue, the CH is red. Spectra (b), (c) and (d) were all taken in N/C/H plasmas. Reactor conditions were: (b) F(1%N_2/H_2)=10 sccm (400 ppm N), F(CH_4)=20 sccm, F(H_2)=470 sccm p= 150 Torr, P=1.8 kW; (c) = F(1%N_2/H_2)=10 sccm (400 ppm N), F(CH_4)=20 sccm, F(H_2)=470 sccm p= 300 Torr, P=1.8 kW; (d) F(NH_3)=3 sccm (6000 ppm N), F(CH_4)=20 sccm, F(H_2)=477 sccm p= 150 Torr, P=1.5 kW. The same CH peaks have been circled in red in (b) and (c) but are not observable in (d). Circled in red are CH peaks, and those circled in blue are CN peaks.

5.2.3 Column density measurements

5.2.3.1 N/H plasmas - results

Profiling the plasma gives insight into the vertical distribution of species. Fig. 5.5 shows z-dependent profiles of NH radicals and H(n=2) atoms. Profile (a) is for an N_2/H_2 plasma, and (b) for an NH_3/H_2 plasma. In (a) and (b) $F(N_2)=F(NH_3)=3$sccm, however in terms of parts per million of nitrogen, N(ppm), in these plasmas, this corresponds to profile (a) = 12000 ppm N and (b) = 6000 ppm N. Profiles (a) and (b) both show that the H(n=2) column density peaks at z≈ 6 mm. The returned column densities for NH increase up to z≈ 8 mm and stretch to higher z than for H(n=2), making the NH profile broader than H(n=2) in both (a) and (b). The NH distribution in (b) is broader than that in (a) and remains constant with increasing z from z = 8→20 mm. The column densities of H(n=2) in both (a) and (b) are similar. NH column densities are different, those returned in (a) are lower than (b) even though the ppm of N is double; column densities in (a) are around 3/4 the size of those shown in (b).

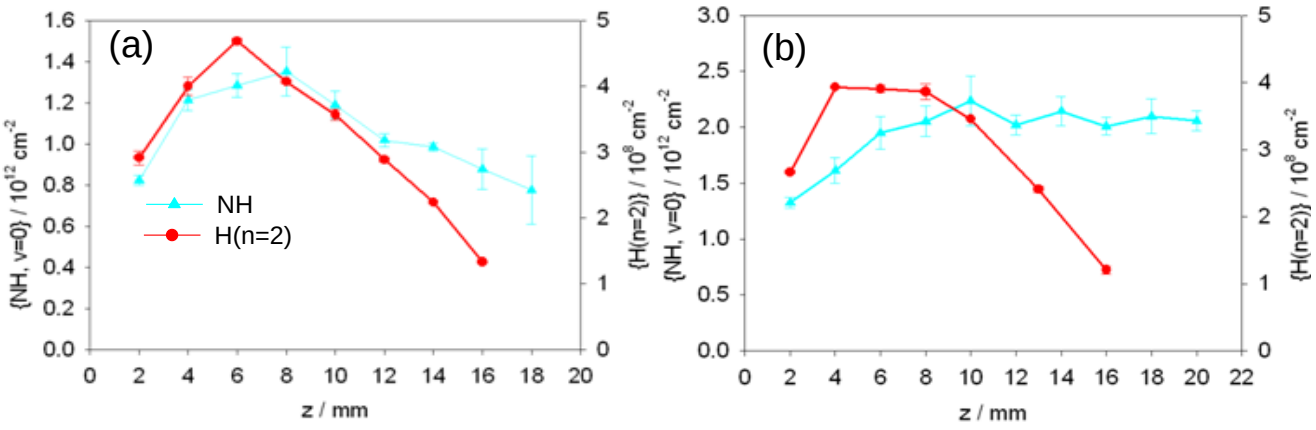

Fig. 5.5 z-dependent column density profiles of NH(X, v=0), H(n=2). In plots (a) and (b) $F_{(tot)}=500$sccm where $F(N_2)=F(NH_3)=3$ sccm and $F(H_2)=497$ sccm, P=1.5 kW, p = 150 Torr. In plot (a) N=12000 ppm, and in (b) N=6000 ppm. The legend for both plots is given in profile (a).

Fig 5.6 gives measured column densities whilst increasing N/ppm within the plasma. Plot (a) is for increasing $F(N_2)$ and (b) when increasing $F(NH_3)$. In both cases, H(n=2) column densities remain constant with increasing N, whereas NH column densities increase. Calculation of the gradients of these plots shows that the increase in NH is steeper in (b) than in (a). It must be noted that higher flow rates and levels of N could

only be reached flowing N_2, due to constraints of the MFC's. The maximum for $F(NH_3)$ was 10 sccm, which corresponds to 20000 ppm N, and $F(N_2)$ rises to 50000 ppm N which corresponds to $F(N_2)$=12.5 sccm. In plots (a) and (b), when moving from 4000→20000 ppm, the column density of NH increases. The calculated gradient of the increase in NH the NH_3/H_2 plasma is around 1.2 times that of the N_2/H_2 plasma and the NH column densities in (b) are twice those calculated in (a) at all comparable values.

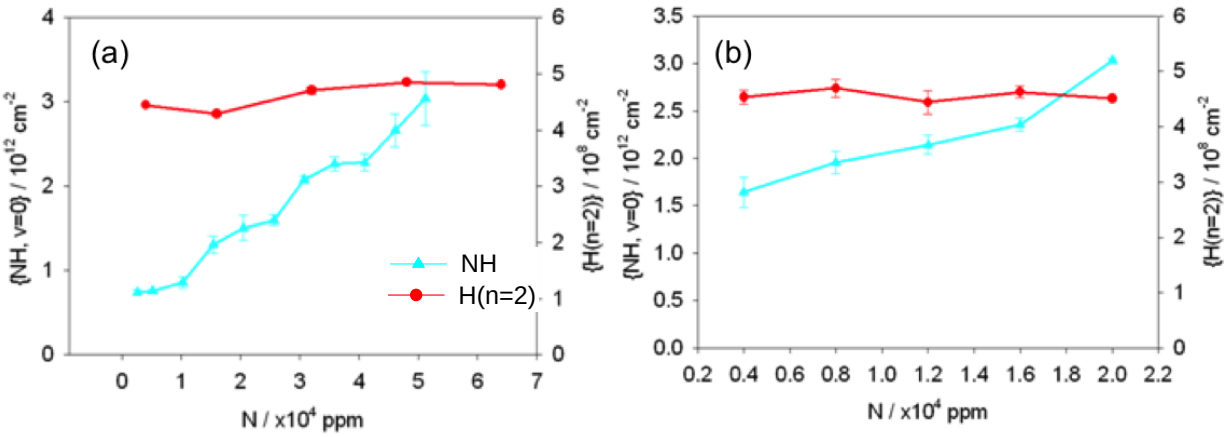

Fig. 5.6 Column densities of NH(X, v=0) and H(n=2) with increasing N. In plots (a) and (b) F_{tot}=500 sccm P=1.5 kW, p = 150 Torr, z=8 mm. $F_{(tot)}$ is kept constant by reducing $F(H_2)$ as $F(N_2)$ and $F(NH_3)$ are increased. In plot (a) the source gas in N_2, in (b) NH_3. The legend for both plots is given in profile (a).

Changes in column density for H(n=2) and NH with increasing power are shown in fig. 5.7. The H(n=2) column density increases linearly with power in an N_2/H_2 plasma (a), and an NH_3/H_2 plasma (b). When using an N_2/H_2 plasma, $F(N_2)$ was increased from 3 sccm (the base condition) to 6 sccm, (i.e. 12000→24000 N/ppm). This was due to difficulty in observing peaks at low powers. Even though N/ppm is four times that in (a) compared to (b), NH column densities in (a) only reach those derived in (b) when P=1.8 kW. There are also differences in NH column densities with increasing P when comparing (a) and (b); NH increases linearly with P in (a), but remains constant in (b).

Fig 5.8 shows how increasing the total pressure affects NH and H(n=2) column densities in an N_2/H_2 plasma, and shows both species increase near linearly with pressure.

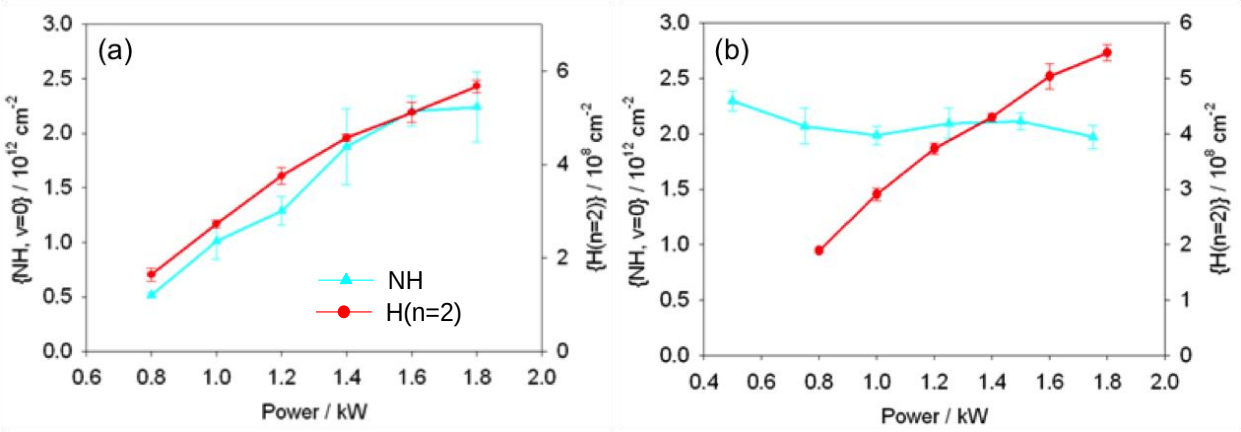

Fig. 5.7 Column densities of NH(X, v=0) and H(n=2) with increasing P. In (a) $F_{(tot)}$=500 sccm where $F(N_2)$ 6 sccm (24000 ppm N) and $F(H_2)$=494 sccm. In (b) F_{tot}=500 sccm where $F(NH_3)$ =3 sccm (6000 ppm N) and $F(H_2)$=497 sccm. In both (a) and (b) p = 150 Torr and z=8 mm. The legend for both plots is given in profile (a).

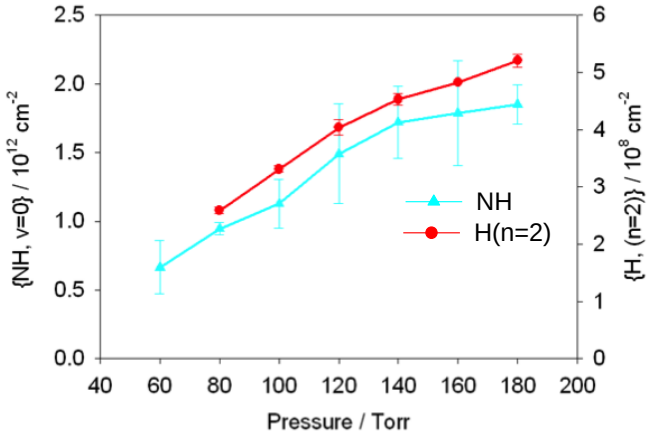

Fig. 5.8 Column densities of NH(X, v=0) and H(n=2) with increasing p. F_{tot}=500 sccm where $F(N_2)$ 6sccm (24000 ppm N) and $F(H_2)$=494 sccm.

5.2.3.2 N/C/H plasmas – results

The following shows results with the inclusion of CH_4 in the gas mixture creating an N/C/H plasma. NH and H(n=2) plots have been plotted separately from those for C containing species because $F(CH_4)$ had to be low in order to observe NH peaks, and higher to observe CH, C_2 and CN peaks. H(n=2) has been plotted with NH to make comparison easier to section 5.2.3.1.

Fig. 5.9 shows z-dependent profiles for NH and H(n=2) in both (a) $N_2/CH_4/H_2$, and (b) $NH_3/CH_4/H_2$ plasmas. $F(N_2)$ had to be increased to 8 sccm, N=32000 ppm in order to record reasonable spectra for plot (a). When comparing both plots, H(n=2) column densities in (a) are around 1.5x larger than (b), and in both plasmas peak at z≈6 mm, as in N/H plasmas. The spatial distribution of NH in 5.9 (a) and (b) is in agreement with fig. 5.5 (a) and (b); it is broader than H(n=2) in both cases, and remains constant to higher z when using NH_3. NH column densities shown in fig. 5.9(a) with an $N_2/CH_4/H_2$ plasma are less than half those in an N_2/H_2 plasma as seen in fig. 5.5 (a). A better comparison, however can be made from the C/N ratio plot fig. 5.6(a), in order to match N/ppm. On this plot, when N=32000 ppm the NH column density corresponds to 2 x 10^{12} cm^{-2}. This means that in the case of an $N_2/CH_4/H_2$ plasma, the addition of CH_4 reduces the NH column density at z=8 mm by 70%. NH column densities recorded by comparison with fig.5.9 (b) with an $NH_3/CH_4/H_2$ plasma are only around 30% less than those from an NH_3/H_2 plasma as seen in fig. 5.5 (b). When comparing fig. 5.9 (a) and (b), NH column densities are almost 3x lower in (a) than (b), even though N/ppm is 5x greater. These trends will be discussed in more detail later in the chapter.

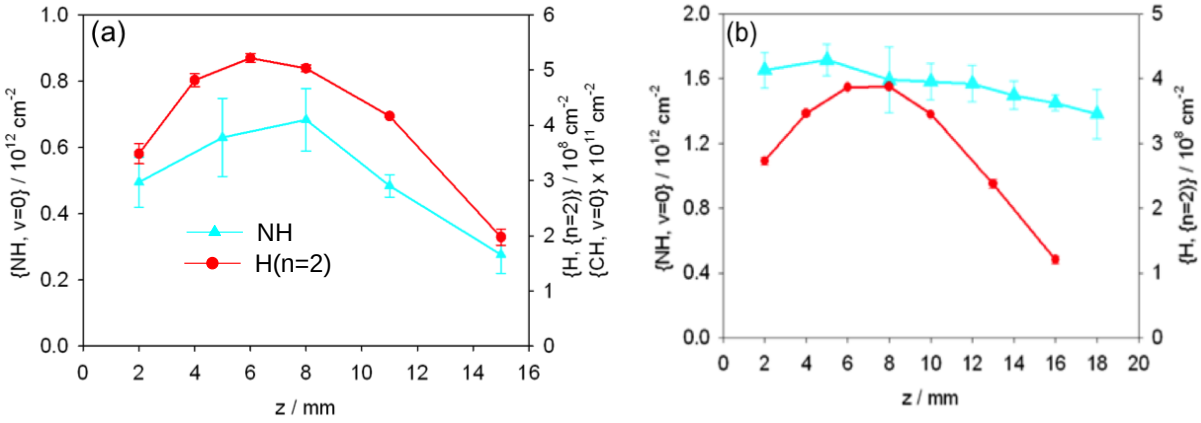

Fig. 5.9, z-dependent column densities of NH(X,v=0) and H(n=2). In (a) F_{tot}=500 sccm where $F(N_2)$=8 sccm (32000 ppm N), $F(CH_4)$=2 sccm and $F(H_2)$=490 sccm. In (b) F_{tot}=500 sccm where $F(NH_3)$ 3 sccm (6000 ppm N), $F(CH_4)$=2 sccm and $F(H_2)$=495 sccm. In both (a) and (b) P=1.5 kW, p = 150 Torr. The legend for both plots is given in profile (a).

Fig 5.10 (a) and (b) show z-dependent profiles for CH, CN, and C_2 in N/C/H plasmas. In both (a) $N_2/CH_4/H_2$ and (b) $NH_3/CH_4/H_2$ plasmas, CH, CN and C_2 column densities all peak at z≈8 mm. This is consistent with previous studies of CH_2/H_2 plasmas in this same reactor.[20] When comparing C_2 and CH column densities it is clear that they are

higher in (a). When comparing CN column densities however, these are considerably different; those shown in fig. 5.10 (b) are around 5x higher than those in (a).

The increase in NH and H(n=2) column density with increasing N/ppm is shown in fig. 5.11. As in fig. 5.6 (a) and (b) for N/H plasmas, H(n=2) remains constant with increasing N in both (a) $N_2/CH_4/H_2$ and (b) $NH_3/CH_4/H_2$. The NH column density in NH is more pronounced with increasing NH_3 in (b) compared to N_2 (a); NH column density increases by 2.5 $x10^{12}$ cm^{-2} with an increase in N of 1.2 x 10^4 ppm in (b), compared to an increase of around 1.2 $x10^{12}$ cm^{-2} in (a), over the same range.

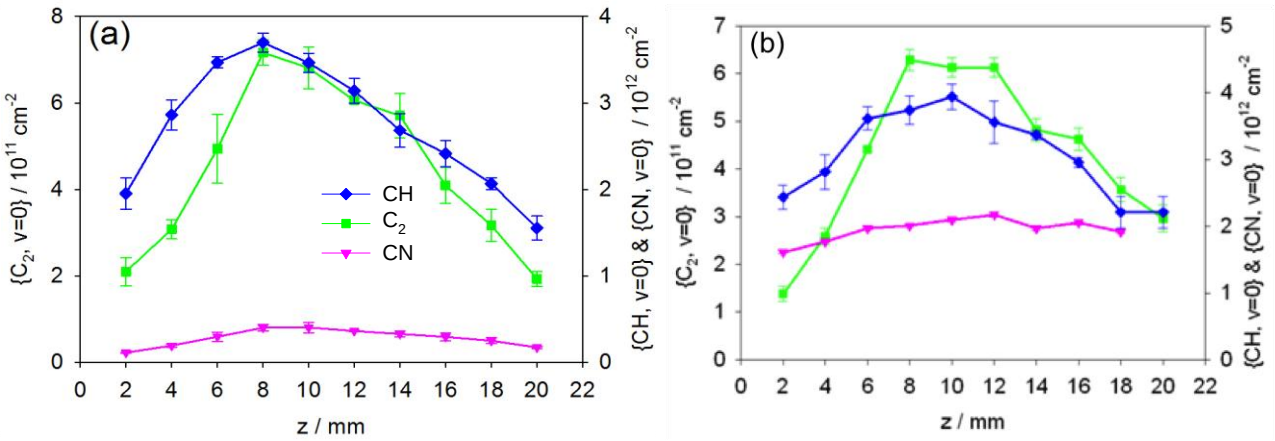

Fig. 5.10. z-dependent column densities of CH(X,v=0) C_2(a,v=0) and CN(X,v=0) in (a) $N_2/CH_4/H_2$ and (b) $NH_3/CH_4/H_2$ plasmas. In both cases F_{tot}=500 sccm where $F(N_2)=F(NH_3)$=3 sccm, $F(CH_4)$=20 sccm and $F(H_2)$=477 sccm; p=150 Torr; P=1.5 kW. The legend for both plots is given in (a).

The change in column densities for CH, C_2 and CN with increasing N/ppm is shown in fig. 5.12. In (a) for an $N_2/CH_4/H_2$ plasma, both C_2 and CH column densities increase slightly with an increase in N, and there is a clear linear increase in CN column density. CN column density also increases in (b) for an $NH_3/CH_4/H_2$ plasma, however this increases at a faster rate than in (a).

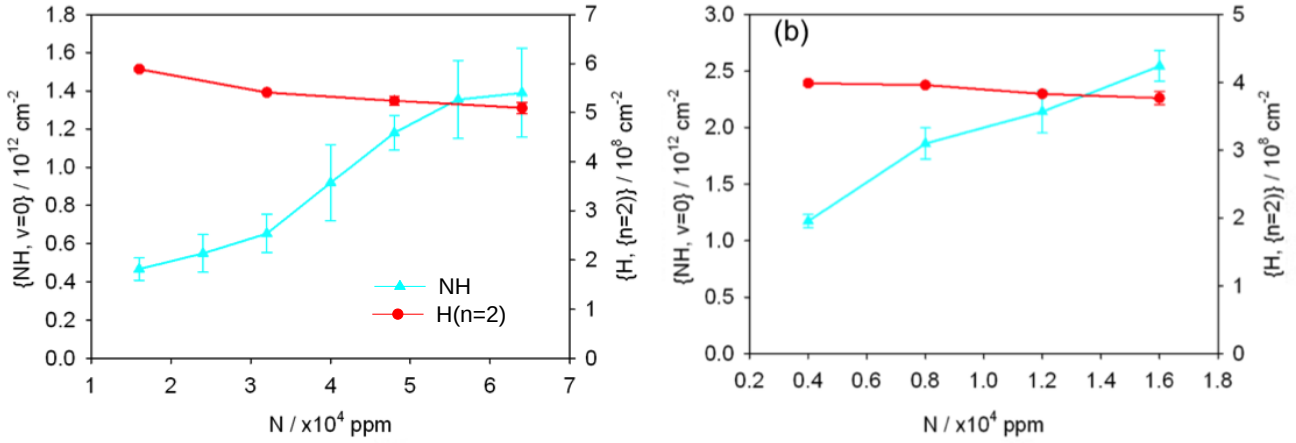

Fig. 5.11 Column densities of NH(X, v=0) and H(n=2) with increasing N. In plots (a) $F(N_2)$ is increased and in (b) $F(NH_3)$ is increased. In both plots F_{tot}=500sccm $F(CH_4)$=2 sccm, P=1.5 kW, p = 150 Torr, z=8 mm. F_{tot} is kept constant by reducing $F(H_2)$ as $F(N_2)$ and $F(NH_3)$ are increased. Plot (a) is for N_2, and (b) NH_3, where in (a) N=12000 ppm, and in (b) N=6000 ppm. The legend for both plots is given in panel (a).

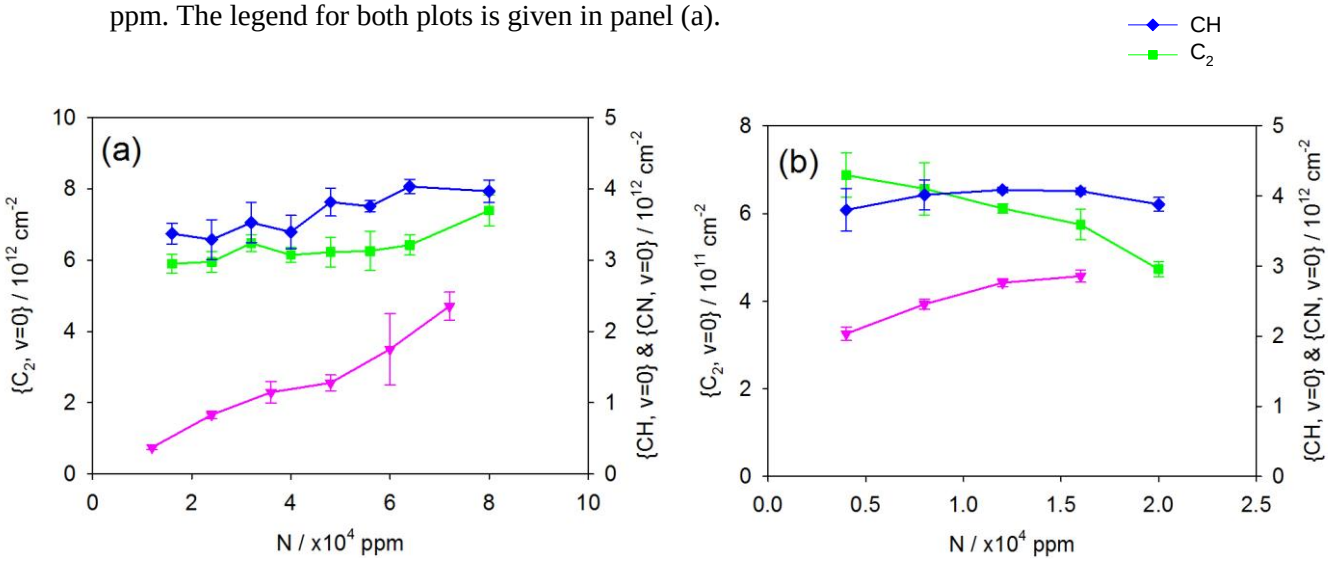

Fig. 5.12 Column densities of CH(X,v=0) C_2(a,v=0) and CN(X,v=0) with increasing N/ppm. In plots (a) and (b) $F_{(tot)}$=500 sccm, $F(CH_4)$=20 sccm, P=1.5 kW, p = 150 Torr, z=8 mm. F_{tot} is kept constant by reducing $F(H_2)$ as $F(N_2)$ and $F(NH_3)$ are increased. In plot (a) N=12000 ppm, and in (b) N=6000 ppm. The legend for both plots is given in panel (a).

Profiles for C_2 and CH were measured to check the the species distributions with increasing N for both N_2 and NH_3 containing N/C/H plasmas. These z-dependent profiles are given in fig. 5.13. Plots (a) and (b) show CH profiles at two different N_2 and NH_3 flow rates. There is a slight increase in CH column density with increasing $F(N_2)$ from N = 12000 → 80000 ppm in (a), and no change in CH column density with increasing $F(NH_3)$ from N=6000 → 20000 ppm in (b). Profiles shown in (c) and (d) are for C_2. These show a slight increase in C_2 with increasing $F(N_2)$ from N=12000

→ 80000 ppm, and around a 25% decrease in C_2 column density with increasing $F(NH_3)$ from N=6000 → 20000 ppm, but the shapes of these profiles are insensitive to these small variations in the total gas mixture.

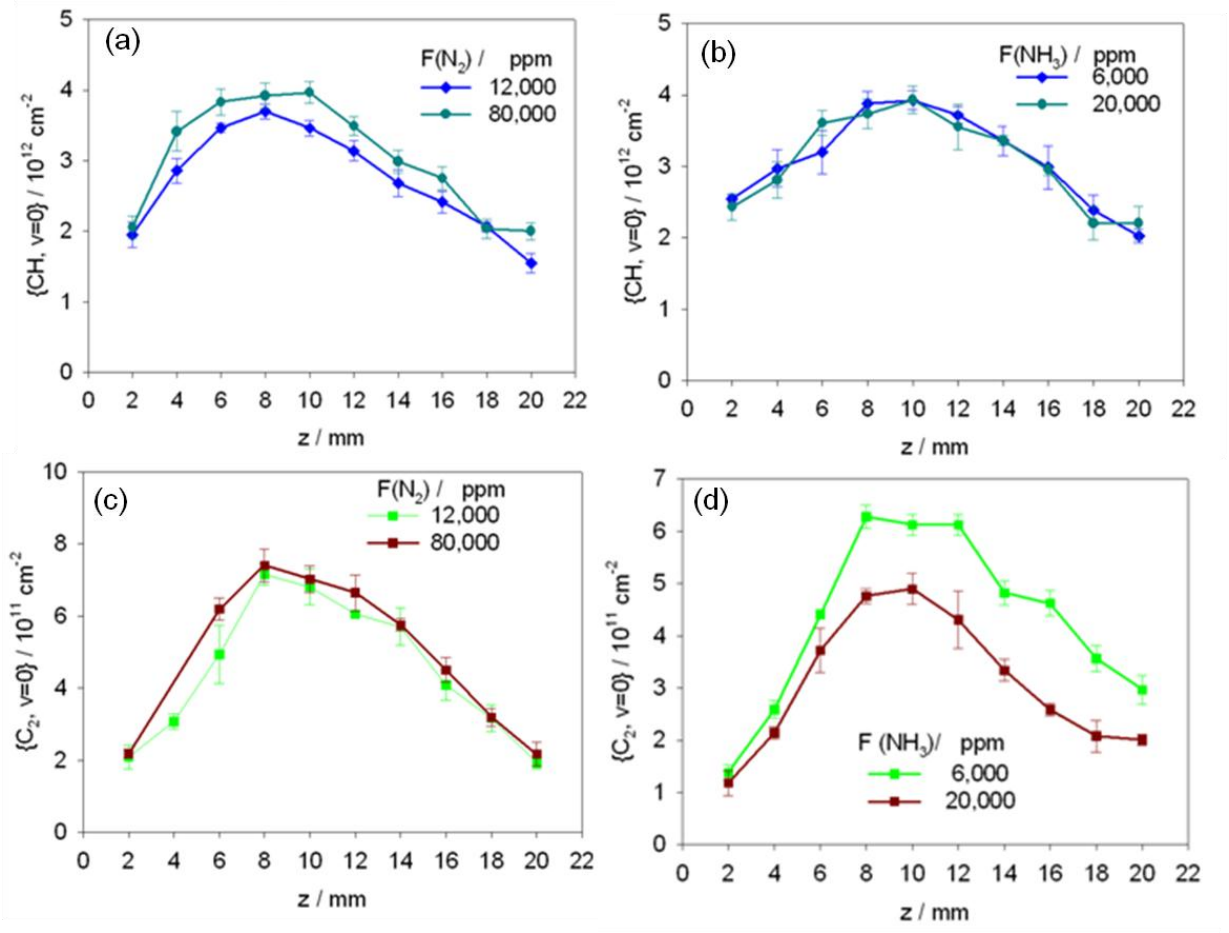

Fig 5.13. Profiles for C_2 and CH column densities with increasing N/ppm. z-dependent column densities for CH are shown in (a) and (b) and C_2 shown in (c) and (d). Both (a) and (c) show species distribution with increasing N(ppm) by increasing $F(N_2)$ from 3 sccm → 20 sccm, and (b) and (d) show species distribution with increasing N(ppm) by increasing $F(NH_3)$ from 3 sccm → 10 sccm. In all cases: P=1.5 kW, p=150 Torr, F_{tot}=500 sccm, $F(CH_4)$=20 sccm and $F(H_2)$ was altered to keep F_{tot} constant.

Changes in column densities of CN, CH, C_2 and H(n=2) whilst increasing pressure at P=1.8 kW are shown in fig. 5.14. These measurements were taken using N_2 at lower concentrations than previously in this chapter, with N=400 ppm. CH column density increases linearly with increasing p, whereas the measured CN column density does not increase until p>200 Torr. The C_2 and H(n=2) column densities increase up to p≈200 Torr, and then begin to level off.

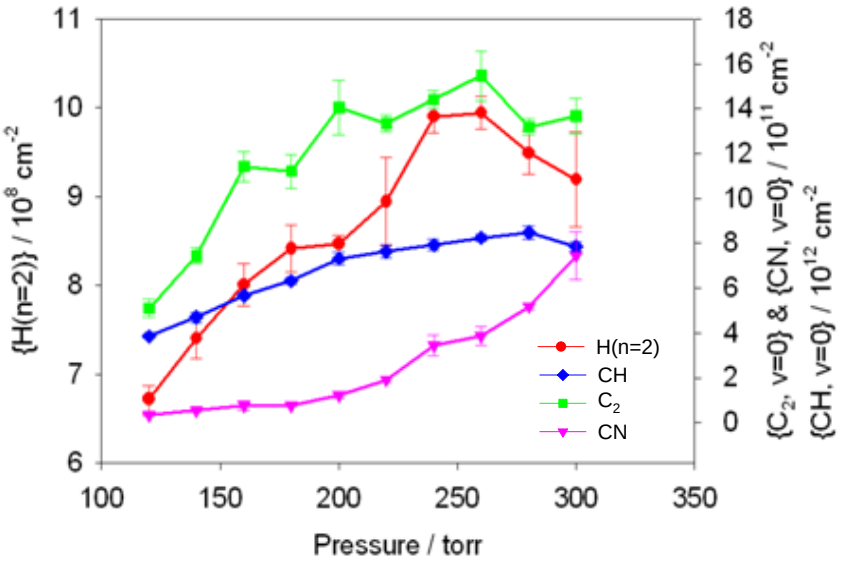

Fig. 5.14 Column densities of CH(X,v=0), C_2(a,v=0), CN(X,v=0) and H(n=2) with increasing p. In this plot: F_{tot}=500 sccm, F(CH_4)=20 sccm, F(1%N_2/H_2)=10 sccm, N=400 ppm, P=1.8 kW, z=8 mm.

Additional CH measurements were taken using lines from the CH($B^2\Sigma$-$X^2\Sigma$) band. These measurements were taken using F(CH_4)=20 sccm and F(N_2)=3 sccm. These measurements save to validate the previous CH measurements (taken on the alternative $A^2\Pi$-$X^2\Sigma$ band). As fig. 5.15 shows, the two profiles are reassuringly consistent.

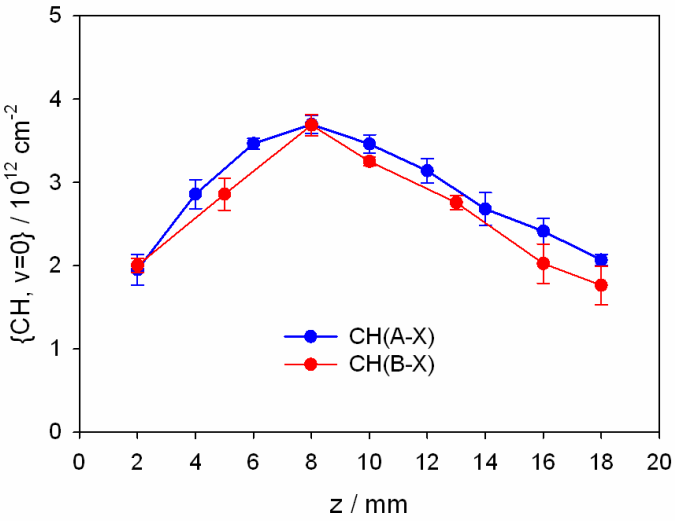

Fig 5.15. z-dependent profiles showing CH column densities derived from CRDS measurements on the CH($B^2\Sigma$-$X^2\Sigma$) and CH($A^2\Pi$-$X^2\Pi$) transitions. F_{tot}=500 sccm where F(N_2)=3 sccm, F(CH_4)=20 sccm and F(H_2)=477 sccm.; P=1.5 kW; p = 150 Torr and z=8mm.

5.2.4 Discussion of CRDS results

The results presented show clear differences in NH and CN distributions measured with N_2 and NH_3 containing N/H and N/C/H plasmas. When comparing z-dependent profiles in N/H plasmas, fig. 5.5 (a) and (b), NH column densities stretch to higher z in an NH_3/H_2 plasma than in an N_2/H_2 plasma. This observed trend indicates that NH forms more easily in an NH_3 plasma, at cooler T_{gas}. This is plausible, since NH production only requires the breakage of N-H bonds compared to the N≡N triple bond. The N_2 bond strength is around 10 eV, which makes dissociation of this species possible via electron impact dissociation in regions of high n_e. T_e=10eV is also the energy required to form H(n=2), so this is perfectly plausible. It may be possible however, that the breakage of N_2 also occurs via thermal dissociation. The abundance of H within the reactor, however will make the sequence of simple H-abstraction reactions moving from $NH_3 \rightarrow NH_2 \rightarrow NH$ occur with ease, in larger volumes of the reactor including volumes where T_{gas} is cooler. This is also seen in profiles taken in N/C/H plasmas as in fig. 5.9, where NH stretches to cooler regions of the NH_3 containing plasma.

As well as differences in species distribution when comparing CN and NH profiles in NH_3 and N_2 containing plasmas, differences are also seen when comparing their column densities. In an N_2/H_2 gas mixture, the NH column density is around 1.5x lower than in NH_3/H_2 plasmas, despite the higher [N] in source gas as shown in fig. 5.5. This again highlights the ease of forming NH from NH_3 rather than N_2. The addition of CH_4 depletes NH and therefore reduces NH column densities in both NH_3 and N_2 plasmas. NH column densities recorded in 5.9 (a) with an $N_2/CH_4/H_2$ plasma are less than half those recorded from an N_2/H_2 plasma as seen in fig. 5.5 (a). This comparison should be made with care, however, since N/ppm is different in both cases, due to the need to increase it when studying CH_4 containing plasmas. A better comparison can be made from the C/N ratio plot fig. 5.6(a). On this plot, when N=32000 ppm, NH $\approx 2 \times 10^{12}$ cm^{-2}. This means that in the case of an $N_2/CH_4/H_2$ plasma, the addition of CH_4 reduces the NH column density at z=8 mm by 70%, since the NH column density moves from 2×10^{12} $cm^{-1} \rightarrow 0.6 \times 10^{12}$ cm^{-1}. In comparison, when adding CH_4 to an $NH_3/CH_4/H_2$ plasma, NH column densities shown in fig. 5.9 (b) are only around 30% less than those from an NH_3/H_2 plasma as seen in fig. 5.5 (b).

In both N_2 and NH_3 containing plasmas, the addition of CH_4 is expected to deplete NH_x (x=0-3) species, from reactions with C containing radicals to form species such as CN and CNH etc. A possible reason for the larger 70% decrease in NH when adding CH_4 to the N_2 plasmas could be because [NH] in these plasmas is less to begin with. Therefore, with the addition of CH_4, NH depletion is more evident when [NH] is less due to reactions with C species. These assumptions remain speculative at this stage, and cannot be confirmed until 2-D model results are complete.

CN production is greater in NH_3 containing plasmas; CN column densities are 5x greater in the $NH_3/CH_4/H_2$ plasma compared to the $N_2/CH_4/H_2$ plasma in fig. 5.10(a) and (b), even though, in the latter, [N] is greater. From the gradient of the increase in CN column density with increasing N/ppm, it is clear that CN is increasing at a faster rate in the $NH_3/CH_4/H_2$ plasma, as in fig. 5.12. This can also be attributed to the ease of breaking an NH bond over the N≡N bond, creating more reactive species available to form CN through reaction with C containing species. Fig. 5.13 shows changes in C_2 and CH profiles with increasing N/ppm by increasing N_2 and NH_3. The only substantial change is for the C_2 profiles when increasing NH_3; C_2 decreases with increasing F(NH_3). This decrease is also seen in fig. 5.12 (b). The decrease in C_2 here helps account for the observed increase in CN column density in an $NH_3/CH_4/H_2$ plasma, which is not observed to the same extent in a $N_2/CH_4/H_2$ plasma.

Increasing the power has the effect of increasing T_e as well as the power density within the given plasma volume, and T_{gas}.[21,22] Fig. 5.7 (a) and (b) confirm that increasing T_e and T_{gas} in an N_2 plasma increases the NH column density. However, in the NH_3/H_2 plasma, no observed change in NH column density is measured. This suggests that there is already enough energy in the latter plasma to break the N-H bond, and the further increase in P shifts the net equilibrium from NH_3 further towards N, with no significant increase in NH column densities. The enhanced reactivity within NH_3 plasmas is also observed with the addition of CH_4 to N/H gas mixtures when observing CN z-dependent profiles in fig. 5.10; the CN distribution is broader in the $NH_3/CH_4/H_2$ plasmas compared to the $N_2/CH_4/H_2$ plasma. This again indicates that there are more reactive N containing species at higher z in NH_3 containing plasmas, than in N_2 containing plasmas, which are available to react with C containing radicals and form CN. Increasing P is also seen to increase the H(n=2)

column densities. This is because the increase in T_{gas} increases thermal dissociation of H_2 and the increase in T_e increases the population excitation to H(n=2).

The effect of increasing p was shown in fig. 5.14, where N=400 ppm. Increasing p causes an increase in T_{gas} and $n_{e,}$ which comes from a decrease in plasma volume and increase in power density, Q, but also an decrease in T_e.[21] The decrease in T_e is evident when following H(n=2) column density, which increases up to 250 Torr at 1.8 kW, then begins to decrease. This is because the decrease in T_e has an effect on the excitation probability to H(n=2), even though H(n=1) is expected to increase with increasing p and $T_{gas.}$ An interesting result, however is the CN column density, which does not increase until p>200 Torr, and is the only species still increasing at 300 Torr. The delayed increase in CN here may be due to a lack of reactive N species in the N_2 plasma until T_{gas} is great enough for dissociation of the N_2 bond. In C/N/H plasmas, only $N_2/CH_4/H_2$ gas mixtures have been investigated so far, as these are most relevant to industrial diamond growth conditions.

Although gas phase modelling of the C/N/H plasmas discussed in this chapter has yet to be completed, it is still important to consider the gas phase chemistry involved within the plasma. An important sequence of reactions to study in N/H containing plasmas is the H-addition/abstraction reactions with N. Some H-transfer reactions between N and H are given below, along with the activation energies (E_a) and reaction rate for the forward reactions,

	E_a (kJ mol^{-1})	k (cm^3 mol^{-1} s^{-1})
$NH_3 + H \leftrightarrow NH_2 + H_2$	42.4	3.8×10^{12} ref 23
$NH_2 + H \leftrightarrow NH + H_2$	29.3	2.7×10^{13} ref 23
$NH + H \leftrightarrow N + H_2$	25.0	2.2×10^{12} ref 24

where T_{gas} = 2000 K, these rates of reactions indicate that both forward and reverse reactions are in fast equilibrium in the hot regions of the gas, meaning that NH_x species will form with ease.

When introducing CH_4 into the feed gas, the same H-transfer reactions will exist as discussed in chapter 1. There will, however be additional reactions between C and N containing species, examples of which are shown below,

	E_a (kJ mol^{-1})	k (cm^3 mol^{-1} s^{-1})
$CH_4 + NH_2 \leftrightarrow CH_3 + NH_3$	55.0	1.0×10^{12} ref 25
$C_2H_2 + NH_2 \leftrightarrow H_2CCNH + H$	67.4	1.4×10^{12} ref 26

where again T_{gas}=2000 K, the rates and barriers given for forward reactions indicate that these reactions will occur with ease under typical reactor conditions used in this thesis.

With the production of $C_xN_yH_z$ species, H-transfer reactions will also occur, such as in the reaction sequence below. These are simple examples of H abstraction reactions with amines, which are likely to exist in the plasma. Equation 5.5 shows the formation of CN species.

$$CH_3NH_2 + H \leftrightarrow CH_2NH_2/CH_3NH + H_2 \quad (5.1)$$

$$CH_2NH_2/CH_3NH + H \leftrightarrow CHNH_2/CH_2NH/CH_3N + H_2 \quad (5.2)$$

$$CHNH_2/CH_2NH/CH_3N + H \leftrightarrow CNH_2/CHNH/CNH_2 + H_2 \quad (5.3)$$

$$CNH_2/CHNH/CNH_2 + H \leftrightarrow HCN/HNC + H_2 \quad (5.4)$$

$$HCN/HNC + H \leftrightarrow CN + H_2 \quad (5.5)$$

5.3 OES investigations

5.3.1 Experimental

The experimental set-up for these OES experiments is as explained in Chapter 4.2. When acquiring OES data, for measuring H(n=3), CN*, C_2* and CH* the same grating, exposure and accumulation times were used. When recording NH* and N_2* spectra a diffraction grating was used which captured a smaller spectral region than previously used. This allowed for greater accuracy, and was important due to the size of the NH and N_2 peaks relative to others.

Base conditions for this work were: p=150 Torr, P = 1.5 kW, F = 500 sccm. For N_2/H_2 and NH_3/H_2 plasmas: F(N_2/NH_3)= 3 sccm, (12000 ppm N), F(NH_3)=3 sccm, (6000 ppm N) and F(H_2)=497 sccm, unless stated otherwise. For $N_2/CH_4/H_2$ and $NH_3/CH_4/H_2$ plasmas: F(N_2)=3 sccm, F(CH_4)=20 sccm and F(H_2)=477 sccm, unless stated otherwise.

5.3.2 Recorded OES spectra

Examples of spectra recorded from N/C/H containing plasmas are shown in fig. 5.16. This shows peaks used in the measurement of CN*, C_2*, CH*, H(n=3), NH* and N_2* emissions for observing different trends in N/H and N/C/H containing plasmas. When progressing from spectra (a) → (c), the spectral range decreases, allowing observation of a greater number of spectral features at higher resolution. Spectrum (a) shows emissions from CN(B-X), CH(A-X), Hα, H_β, and C_2(d-a). Spectrum (b) shows emissions from the CN(B-X) transitions over an expanded spectral range. This shows the Δv = 0, +1 and -1 progressions. The largest peaks observable in the Δv =0 sequence, are the (0,0), (1,1) and (2,2) transitions. Those in the Δv = -1 sequence are at higher wavelength, and from biggest to smallest sized peaks are : (0,1), (1,2), (2,3) and (3,4). CN (B-X) emissions from the Δv = +1 sequence are at lower wavelength and overlap with emissions from N_2 and NH, as can be seen in (c). Fig. 5.16 (c) also shows peaks given by emissions from NH(A-X) and N_2(C-B).

When measuring trends in NH* and N_2*, recorded spectra were fitted to simulated spectra in Pgopher, which also allowed for the estimation of T_{gas} via the rotational temperature used in the fitting routine.To allow estimation of trends in T_e with changes in process conditions, emissions from Ar were measured, as these rely strongly upon electron chemistry due to the large energy gap between ground and excited states. A recorded spectrum showing Ar emissions is displayed in fig. 5.17, which shows three Ar* lines at 750, 763 and 811 nm.

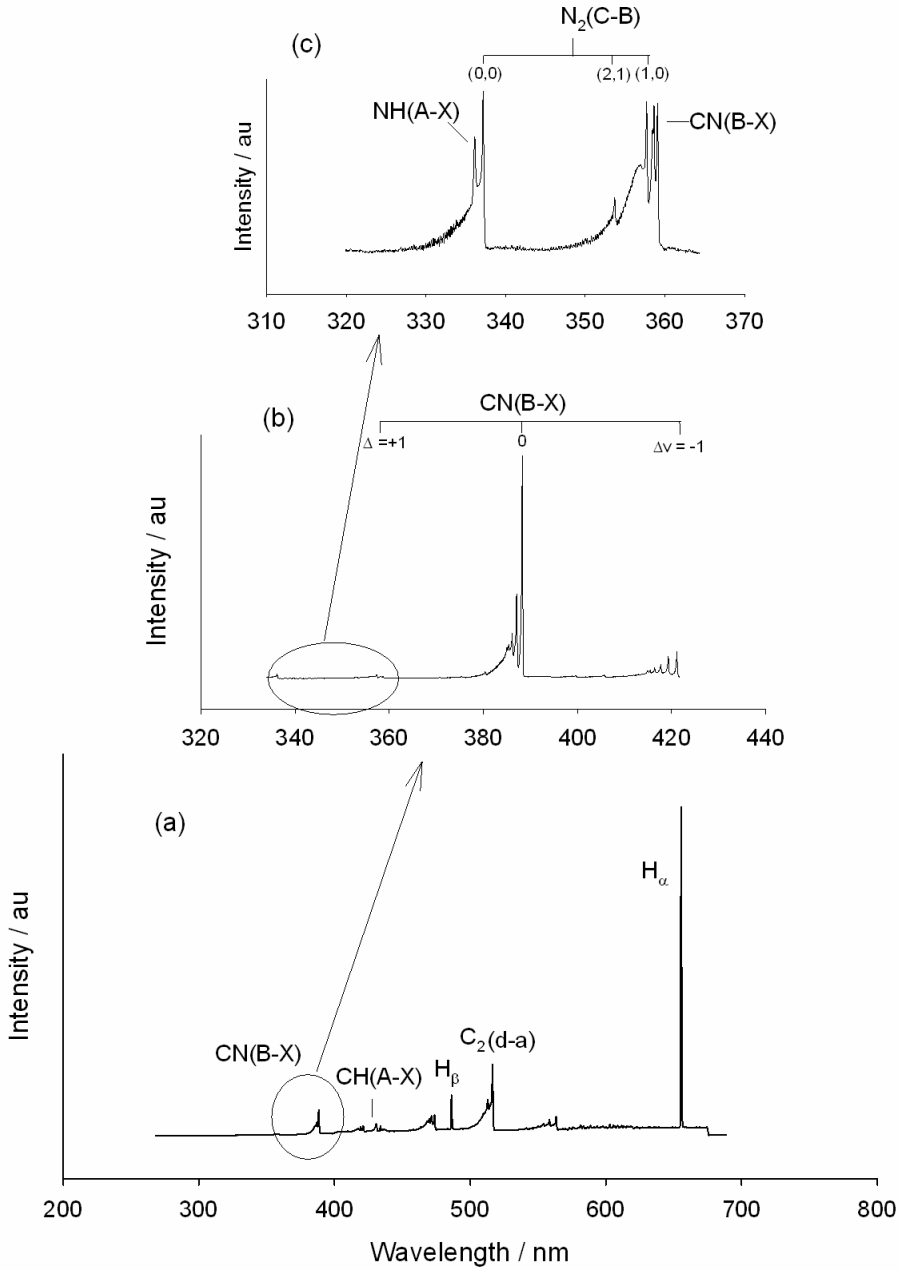

Fig. 5.16 OES spectra recorded for an $N_2/CH_4/H_2$ plasma, where p=150 Torr, P = 1.5 kW $F(N_2)$=3sccm, $F(CH_4)$=20 sccm $F(H_2)$=477 sccm. Spectra (a) → (c) show successively expanded spectral ranges, corresponding to the circled areas on the spectrum below.

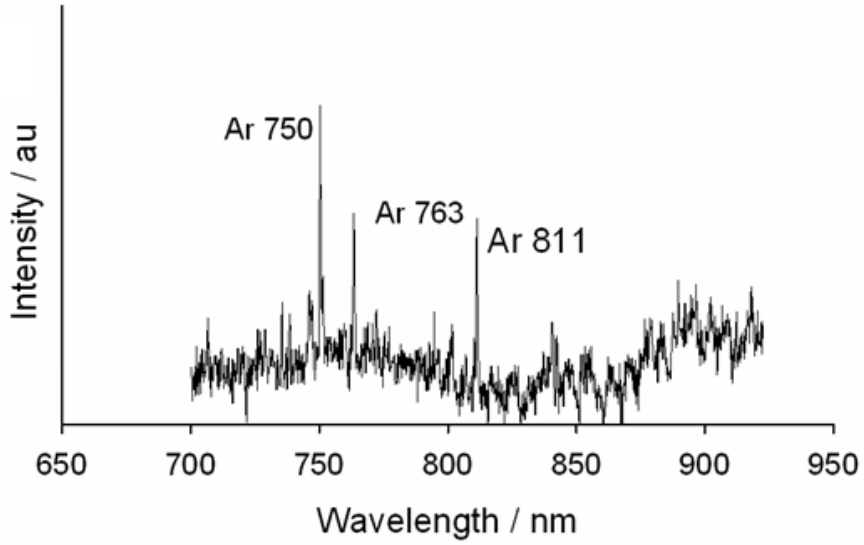

Fig 5.17. Recorded spectrum showing emissions from Ar*.

5.3.3 OES measurements

5.3.3.1 N/H plasmas – results

The following section displays OES results, which will be discussed throughout the chapter, and where appropriate these are compared to CRDS results from 5.2.2.2. This research is still ongoing, and there are no 2-D model results to include in the discussion at this stage.

Z-dependent profiles in fig. 5.18 show emissions from NH*, H(n=3) and N_2*. Plot (a) shows emissions from an N_2/H_2 plasma, and (b) from an NH_3/H_2 plasma. In (a), emissions from NH* peak at z≈8 mm, emissions from H(n=3) at 7mm and emissions from N_2* peak at z≈6 mm. In (b), NH* and H(n=3) emissions peak at z=8 mm, and N_2* emission was immeasurably small.

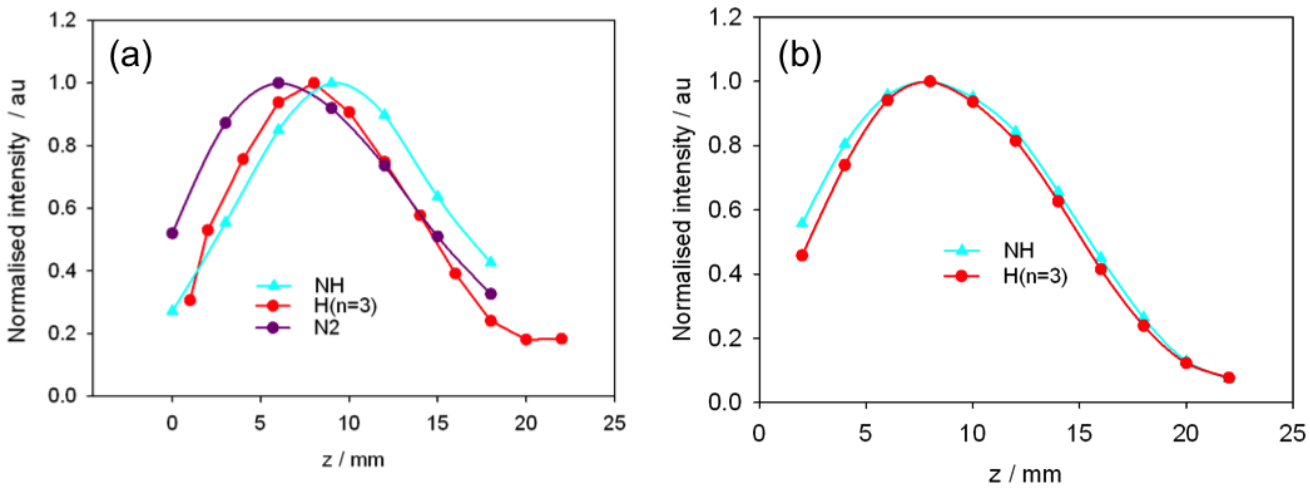

Fig. 5.18 OES plots showing z-dependent profiles for (a) an N_2/H_2 plasma, and (b) an NH_3/H_2 plasma. In both cases F_{tot}=500 sccm, where $F(NH_3)=F(N_2)$=3 sccm, $F(H_2)$=497 sccm.; P=1.5kW; p=150 Torr. Emissions from all species have been normalised so that the maximum intensity (I_{max}) for each species = 1.0.

With regards to species emissions, these are a convolution of n_e and the distribution of species in their respective ground states. 2-D modelling of previous studies of C/H plasmas has shown that n_e peaks at $z\approx5$ mm.[21] In fig. 5.18 (a) for an N_2/H_2 plasma, the distribution of NH* and H(n=3) is similar to that in (b) for an NH_3/H_2 plasma, yet when comparing these results to column densities measured by CRDS in fig. 5.5 (a) and (b), there are discrepancies; NH stretches to higher z in both N_2 and NH_3 plasmas measured by CRDS. This is because there are less and less electrons with increasing height in the plasma to create the excited states from which emission can be measured. An interesting result from fig. 5.18 (a) is that N_2 emissions peak at lower z than NH emissions.

Fig. 5.19 shows emissions from NH*, H(n=3) and N_2* with increasing power. From both (a) and (b) it is evident that emissions from all species measured are increasing with power. This is because increasing power increases T_e and T_{gas},[22] which is shown in fig. 5.20 (a) and (b). The increase in T_{gas} shown in 5.20 (a) comes from fitting recorded emission spectra to the spectral simulation program Pgopher, with increasing P. The increase in T_e shown in fig. 5.20 (b) comes from measuring emissions from Ar* at 750nm, and is also seen to increase with power. Ar* is an excellent indicator of changes in T_e due to the large energy gap between its ground and excited states, Ar* formation is dependent upon collision with high energy electrons, ie. Ar + e → Ar* +

e . H(n=3) is also included in (b) as the formation of this species is also dependent upon highly energetic electrons.

Discrepancies arise when comparing trends in species emission with absolute column densities measured in an NH_3/H_2 plasma. Fig 5.7 (b) showed that the column density of NH does not change in an NH_3/H_2 plasma between 0.6 and 1.8 kW, which can be attributed to the weakness of the N-H bond. However, in fig. 5.19 (b) emissions increase with increasing power, reflecting the increase in T_e and n_e. The NH column density and emissions from NH* in an N_2/H_2 plasma shown in fig. 5.7(a) and 5.19 (a), however, both increase with power.

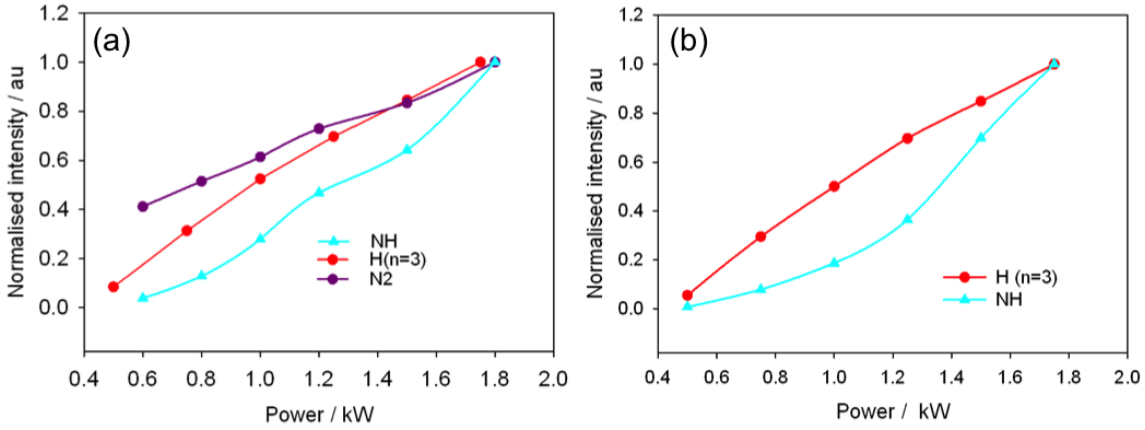

Fig. 5.19 OES plots showing emission from NH*, N_2* and H(n=3) with increasing P for (a) an N_2/H_2 plasma, and (b) an NH_3/H_2 plasma. In both cases $F_{(tot)}$=500 sccm, where $F(NH_3)=F(N_2)$=3 sccm, $F(H_2)$=497 sccm.; p=150 Torr and z=8 mm. Emissions from all species have been normalised so that I_{max} for each species = 1.0.

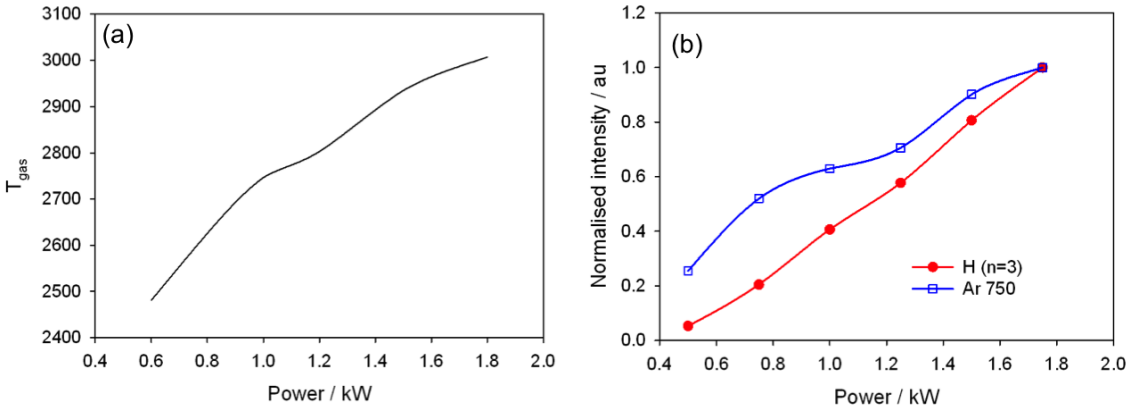

Fig 5.20. This plots shows (a) increase in T_{gas}, and (b) increase in Ar 750 nm and H(n=3) emissions as a function of power. $F_{(tot)}$=500 sccm, where $F(N_2)$=3 sccm, $F(H_2)$=497 sccm.; p=150 Torr and z=8 mm. Plot (b) has been normalised so that I_{max} for each species = 1.0.

Dissociation of N_2 with increasing power can be seen in Fig. 5.21, which shows the NH/N_2 emission intensity ratio as I_{NH}/I_{N_2}. From this plot it is clear that emissions from NH are increasing at a greater rate than those from N_2 with increasing power.

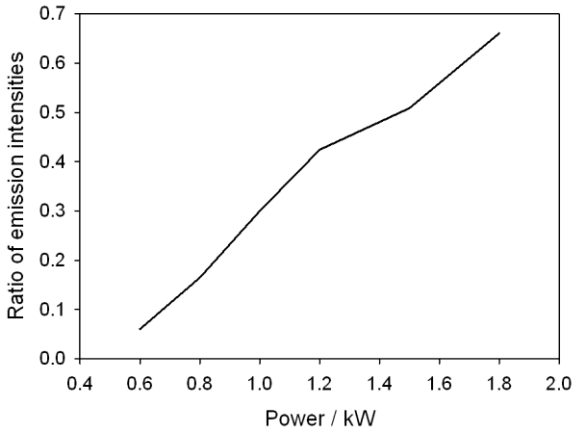

Fig 5.21. Ratio of NH to N_2 emissions in an N_2/H_2 plasma, showing I_{NH}/I_{N_2} as a function of power. $F_{(tot)}$=500 sccm, where $F(N_2)$=3 sccm, $F(H_2)$=497 sccm.; p=150 Torr and z=8 mm. Data taken from fig. 5.19 (a)

5.3.3.2 N/C/H plasmas – results

Fig 5.22 shows z-dependent profiles for emissions from C_2*, CH*, CN*, NH*, N_2* and H(n=3). In both (a) and (b), for $N_2/CH_4/H_2$ and $NH_3/CH_4/H_2$ plasmas respectively, C_2* and CH* both peak in emission intensity at z≈10 mm. In (a) N_2 peaks lowest in the plasma at z=6 mm, however in comparison with fig. 5.18 (a) in an N_2/H_2 plasma, emissions from NH have moved to lower z. This may be a reflection of a slightly flatter distribution of NH at z<8 mm with the addition of CH_4 to an N_2/H_2 plasma, as seen when comparing CRDS results fig. 5.5(a) and 5.9(a). This results in NH emissions being greatest where there is the greatest spatial overlap between NH in its ground state and n_e.

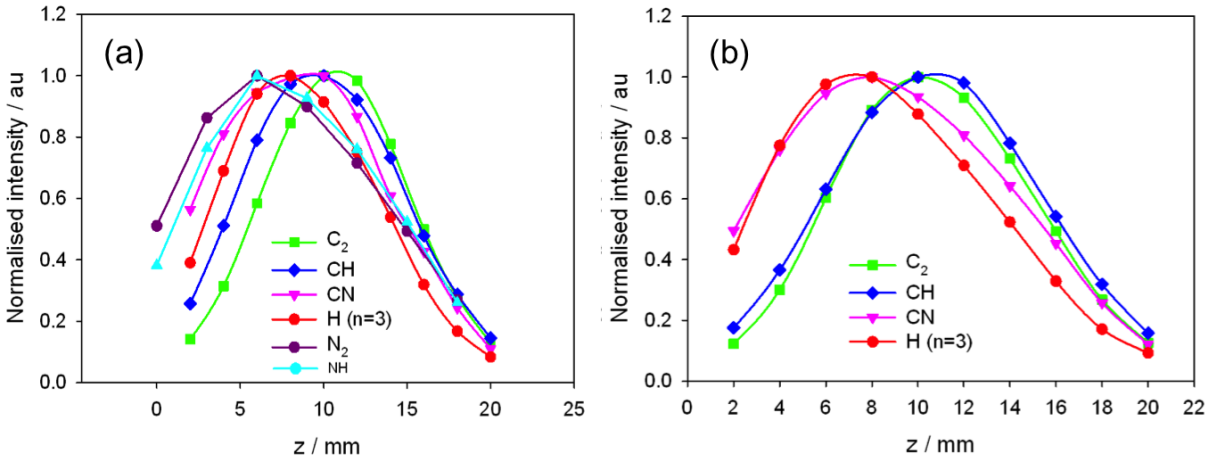

Fig. 5.22 OES plots showing z-dependent profiles for (a) an $N_2/CH_4/H_2$ plasma, and (b) an $NH_3/CH_4/H_2$ plasma. Emissions from C_2*, CH*, CN*, NH*, N_2* and H(n=3) are shown. In both cases $F_{(tot)}$=500 sccm, where $F(NH_3)=F(N_2)$=3 sccm, $F(CH_4)$=20 sccm, $F(H_2)$=477 sccm.; P=1.5kW; p=150 Torr. The peak emission from all species have been normalised to unity.

When comparing the $N_2/CH_4/H_2$ plasma in (a) with the $NH_3/CH_4/H_2$ plasma in (b), the distribution of both H(n=3) and CN* move from (a) z≈9 mm to (b) z≈7 mm. The distribution of CN column density shown in fig. 5.10 in an $NH_3/CH_4/H_2$ plasma is relatively flat. This has the effect of allowing the distribution of CN emissions to peak at slightly lower z where the overlap between CN in its ground state and n_e is greatest. As previously discussed, H(n=3) emissions also peak below the hot central region of the plasma where n_e is greatest, as its formation is dependent upon highly energetic electrons (T_e>10eV).

Fig. 5.23 shows changes in species emission with increasing CH_4 /ppm at constant: (a) $F(N_2)$ and (b) $F(NH_3)$. This has the effect of increasing the C/N ratio within the reactor. In both (a) and (b) for $N_2/CH_4/H_2$ and $NH_3/CH_4/H_2$ plasmas, the addition of CH_4 causes all C containing species emissions to increase. In (a) and (b), the increase in CN* and CH* emissions is steeper than for C_2*, which increases linearly with CH_4. This is more than likely because with CH_4 addition C_2 increases linearly, and CH increases less steeply, which is consistent with previous model results which show the dependencies as $[CH_4]$~$[C_2]$ and $[CH_4]^{0.5}$~[CH].[21] In (a), NH* emissions decrease sharply with the addition of a small amount of CH_4 to the plasma then remain relatively flat

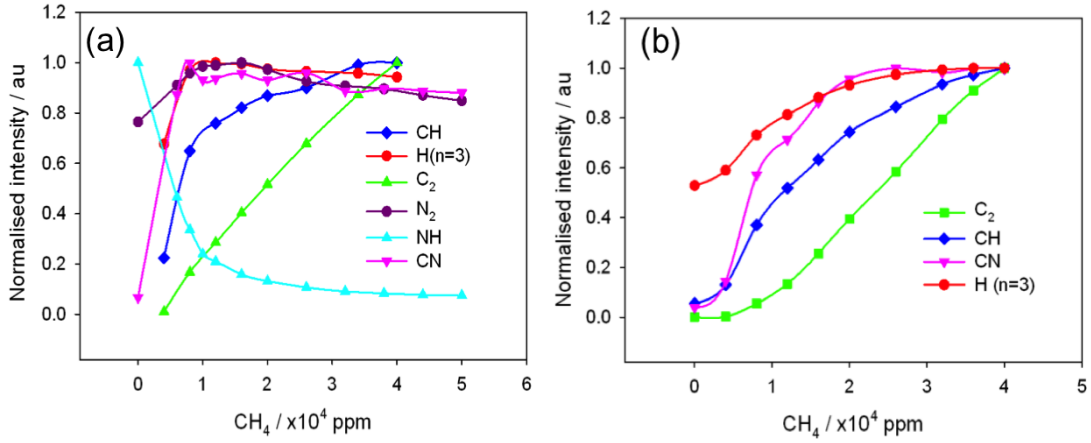

Fig. 5.23 OES plots showing changes in species emission with increasing CH_4 (ppm) in (a) a $N_2/CH_4/H_2$ and (b) an $NH_3/CH_4/H_2$ plasma. Emissions from C_2*, CH*, CN*, NH*, N_2* and H(n=3) are shown. In both cases $F_{(tot)}$=500 sccm, where $F(NH_3)=F(N_2)$=3 sccm, $F(H_2)$=477 sccm.; P=1.5kW; p=150 Torr.; z=8 mm. Peak emissions from all species have been normalised to unity.

A plot showing T_{gas} vs CH_4/ppm is shown in 5.24 (a). This shows an immediate decrease in T_{gas} with the addition of CH_4 to an N_2/H_2 plasma, which then remains constant. Fig 5.24 (b) shows the changes in emissions as ratios for an $N_2/CH_4/H_2$ plasma. The I_{CN}/I_{NH} ratio is seen to increase with increasing CH_4, which make sense since this should increase with the C/N ratio. The I_{NH}/I_{N_2} ratio however, is seen to decrease then remain constant.

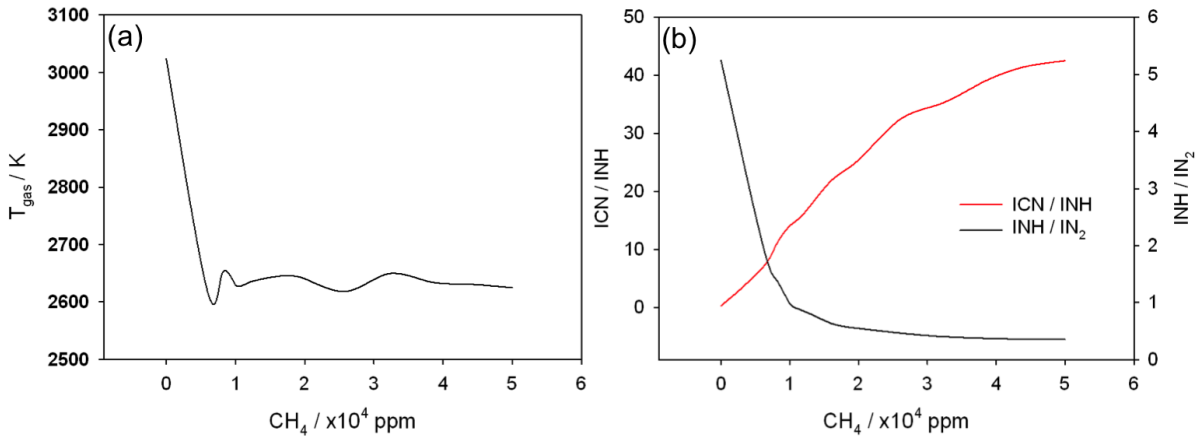

Fig. 5.24. Shows (a) changes in T_{gas} with increasing CH_4 /ppm by fitting recorded spectra into the spectral simulation program Pgopher, and (b) the ratios of I_{CN}/I_{NH} and I_{NH}/I_{N_2} with increasing CH_4 /ppm at z=8 mm. I_{CN}/I_{NH} follows the left hand y-axis, and $I_{NH}/_{N_2}$ the right hand axis. Data recorded from the $N_2/CH_4/H_2$ plasma in 5.23 (a).

Fig. 5.25 shows trends in species emission with increasing power. In both (a) and (b), for $N_2/CH_4/H_2$ and $NH_3/CH_4/H_2$ plasmas, emissions from all species increase with

power. With regards to CN emissions, the steepest increase in these in the $N_2/CH_4/H_2$ plasma is not seen until P>1.5 kW, whereas in the $NH_3/CH_4/H_2$ plasma, the CN emission increases linearly with P. This may be because CN formation is dependent upon reactive N species within the plasma, which are not in great enough abundance in the N_2 containing plasma until there is enough energy for N_2 dissociation. In both (a) and (b) CH increases almost linearly with P, but C_2 emissions do not increase until P>1 kW.

Fig. 5.26 shows the ratios of species emission for I_{CN}/I_{NH} and I_{NH}/I_{N_2} in an $N_2/CH_4/H_2$ plasma. The I_{CN}/I_{NH} ratio increases with increasing power. As power increases, so does T_e and T_{gas}, as explained in the earlier data discussed in fig. 5.19, and this is likely to result in increased dissociation of the N_2 bond, and an increase in reactions of C containing radicals with N containing radicals, therefore increasing CN formation and the probability of e-impact excitation to yield CN* emissions.

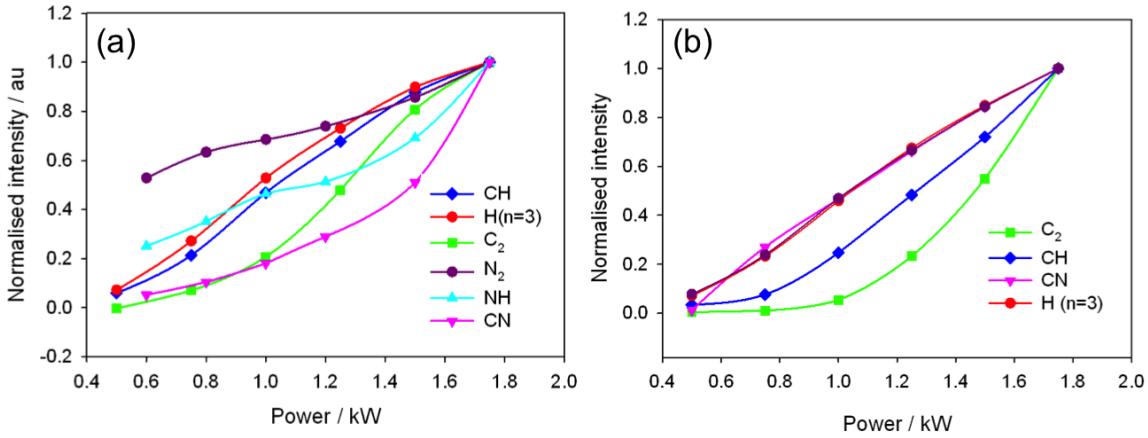

Fig. 5.25 OES plots showing changes in species emission with increasing power in (a), an $CH_4/N_2/H_2$ plasma, and (b) an $CH_4/NH_3/H_2$ plasma. Emissions are shown from C_2*, CH*, CN*, NH*, N_2* and H(n=3). In both cases $F_{(tot)}$=500 sccm, where $F(NH_3)=F(N_2)$=3 sccm, $F(CH_4)$=20 sccm and $F(H_2)$=477 sccm.; p=150 Torr and z=8mm. Peak emissions from all species have been normalised to unity.

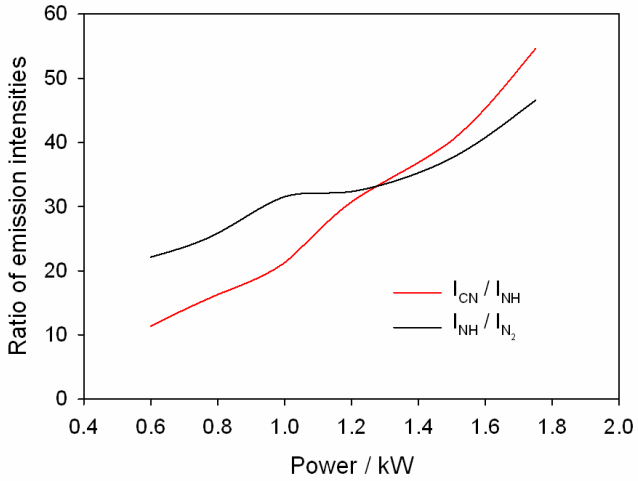

Fig 5.26 The ratio of I_{CN}/I_{NH} and I_{NH}/I_{N2} with increasing power in an $N_2/CH_4/H_2$ plasma, taken from 5.25 (a).

Fig. 5.27 shows results for increasing pressure in (a) $N_2/CH_4/H_2$ and (b) $NH_3/CH_4/H_2$ plasmas. Plot (a) was run at 400ppm in order to compare to the CRDS results in fig. 5.14. In fig. 5.14, the column densities of both C_2 and CH increase with pressure. In fig 5.27 (a), however, C_2* and CH* emissions follow the same trend as CN*. The discrepancy between trends in column density and emission from C_2 and CH may come from a change in the overlap of these radicals in their ground states with n_e. Emissions from CN*, however, do not increase until P>200 Torr, which is in agreement with the column densities shown in fig. 5.14. H(n=3) emissions are seen to increase with increasing p, followed by a decrease, shown by a flattening out of the H(n=3) curve in fig. 5.27 (a). This is because, with increasing p, H_2 dissociation to H(n=1) also increases on account of the increase in T_{gas}. Emissions from H(n=3) decrease with increasing p because of the decrease in T_e.[22] The decrease in T_e with increasing p can be seen in fig. 5.28, which shows emissions from Ar* and H(n=3).

Fig. 5.27 (b) shows changes in species emission with increasing pressure in an $NH_3/CH_4/H_2$ plasma. The short range measured is only equivalent to half the increase in pressure plotted in (a), however emissions from CH*, C_2*, CN* and H(n=3) are all seen to increase. In (b) CN* emissions increase at lower p than in (a). An explanation for this could be the increased NH concentration in an NH_3 plasma available to react with C containing species. Again, H(n=3) emissions begin to level out with increasing p.

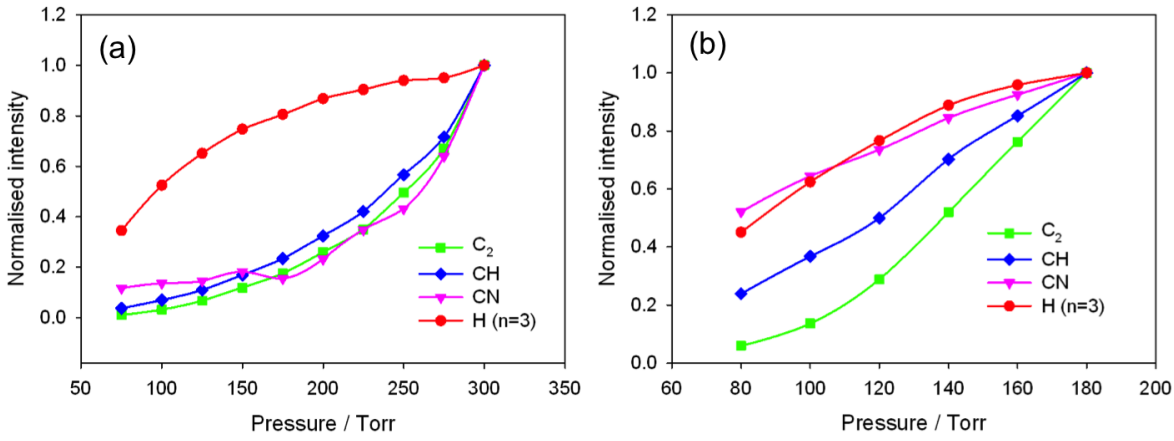

Fig. 5.27 OES plots showing changes in species emission with increasing pressure in (a) $CH_4/N_2/H_2$ plasma, and (b)$CH_4/NH_3/H_2$ plasmas. Emissions are shown from C_2*, CH*, CN*, NH*, N_2* and H(n=3). In (a) $F_{(tot)}$=500 sccm, where $F(1\%N_2/H_2)$=10 sccm, $F(CH_4)$=20 sccm and $F(H_2)$=470 sccm; P=1.8 kW. In (b) $F(NH_3)$=3 sccm, $F(CH_4)$=20 sccm and $F(H_2)$=477 sccm; P=1.5 kW. In both plots z=8 mm. Peak emissions from all species have been normalised to unity.

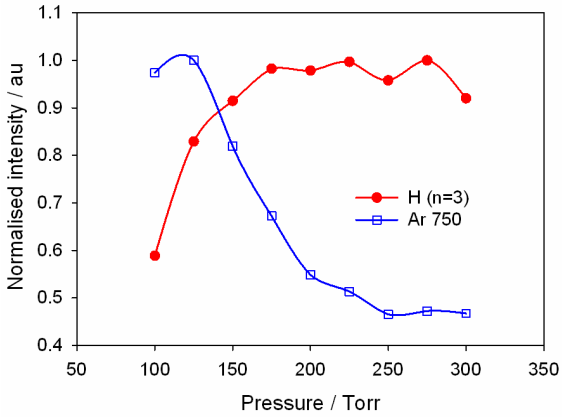

Fig. 5.28. Changes in H(n=3) and Ar emissions with increasing pressure.

5.4 Conclusions

The concentrations of both NH and CN depend strongly on the concentration of N containing species available in the plasma. Thus their respective column densities in N_2 containing plasmas, due to the greater strength of the N_2 triple bond, are much lower than when using NH_3 as the source gas. The inclusion of CH_4 also has the effect of lowering NH column densities on addition to both N_2/H_2 and NH_3/H_2 plasmas, as a

result of (a) a reduction in T_{gas} (at least in the case of N_2 containing plasmas), and (b) NH_x (x=0-3) loss by reaction with C containing species.

In the presented results and discussion, the results which are most relevant to conditions used industrially when growing diamond films are those with 400 ppm N in the source gas mixture. The results from increasing pressure in a plasma with 400 ppm N at 1.8 kW showed that an increase in measured CN column densities is not achieved until p>200 Torr, whereas column densities from C_2, CH and H(n=2) increased once p>120 Torr. This becomes relevant if CN is assumed to play a part in the increase in growth rate observed when including N in the source gas mixture. NH column densities were not measurable under these conditions, however this does not mean CN and NH are not present in the plasma, just that only CN was measurable with CRDS.

Results from OES experiments are difficult to interpret without conclusions from 2-D modelling of various C/N/H gas mixtures. This is because model results give a good estimation of n_e and species distribution. However, OES can tell us when T_{gas} (from fitting to pgopher simulation), and T_e (from Ar* emission intensities) are increasing. Under these conditions I_{NH}/I_{N_2} increases, which is consistent with an increased probability of N_2 dissociation in the case of N_2/H_2 and $N_2/CH_4/H_2$ plasmas.

Due to the difficulty in observing CN peaks under conditions for recording NH, and vice versa, no direct comparison between the two species can be made without use of 2-D modelling results. However, under conditions relevant to industrial diamond growth (400 ppm N in an $N_2/CH_4/H_2$ plasma) indicate that CN may be of greater column density than NH above the growing surface. This is because NH was immeasurable when increasing p in fig. 5.14 with 400 ppm N in an $N_2/CH_4/H_2$ plasma. Nonetheless, it is clear that both species will be present in the vicinity of the growing surface. The next chapter explores possible ways in which either or both species could interact with, and be accommodated at, a diamond surface.

5.5 References

1. Yan, C. S. Very high growth rate chemical vapor deposition of single-crystal diamond. *Proc. Natl. Acad. Sci.* **99,** 12523 (2002).

2. Chayahara, A. *et al.*. The effect of nitrogen addition during high-rate homoepitaxial growth of diamond by microwave plasma CVD. *Diam. Relat. Mater.* **13,** 1954 (2004).

3. Müller-Sebert, W., Worner, E., Fuchs, F., Wild, C. & Koidl, P. Nitrogen induced increase of growth rate in chemical vapor deposition of diamond. *Appl. Phys. Lett.* **68,** 759 (1996).

4. Jin, S. & Moustakas, T. D. Effect of nitrogen on the growth of diamond films. *Appl. Phys. Lett.* **65,** 403 (1994).

5. Chatei, H., Bougdira, J., Remy, M. & Alnot, P. Mechanisms of diamond films deposition from MPACVD in methane-hydrogen and nitrogen mixtures. *Surf. Coatings Technol.* **98,** 1013 (1998).

6. Achatz, P. *et al.*. Effect of nitrogen on the electronic properties of ultrananocrystalline diamond thin films grown on quartz and diamond substrates. *Phys. Rev. B* **74,** 155429 (2006).

7. Bhattacharyya, S. *et al.*. Synthesis and characterization of highly-conducting nitrogen-doped ultrananocrystalline diamond films. *Appl. Phys. Lett.* **79,** 1441 (2001).

8. Bhattacharyya, S. Mechanism of high n-type conduction in nitrogen-doped nanocrystalline diamond. *Phys. Rev. B* **70,** 125412 (2004).

9. Zapol, P., Sternberg, M., Curtiss, L., Frauenheim, T. & Gruen, D. Tight-binding molecular-dynamics simulation of impurities in ultrananocrystalline diamond grain boundaries. *Phys. Rev. B* **65,** 045403 (2001).

10. Vandevelde, T., Nesladek, M., Quaeyhaegens, C. & Stals, L. Optical emission spectroscopy of the plasma during CVD diamond growth with nitrogen addition. *Thin Solid Films* **290,** 143 (1996).

11. Vandevelde, T. *et al.*. Correlation between the OES plasma composition and the diamond film properties during microwave PA-CVD with nitrogen addition. *Thin Solid Films* **340,** 159 (1999).

12. Vandevelde, T., Nesladek, M., Quaeyhaegens, C. & Stals, L. Optical emission spectroscopy of the plasma during microwave CVD of diamond thin films with nitrogen addition and relation to the thin film morphology. *Thin Solid Films* **308,** 154 (1997).

13. Chatei, H., Bougdira, J., Remy, M. & Alnot, P. Optical emission diagnostics of permanent and pulsed microwave discharges in H_2–CH_4–N_2 for diamond deposition. *Surf. Coatings Technol.* **116,** 1233 (1999).

14. Plamann, K., Fournier, D., Anger, E. & Gicquel, A. Photothermal examination of the heat diffusion inhomogeneity in diamond films of sub-micron thickness. *Diam. Relat. Mater.* **3,** 752 (1994).

15. Achard, J., Tallaire, A., Sussmann, R., Silva, F. & Gicquel, A. The control of growth parameters in the synthesis of high-quality single crystalline diamond by CVD. *J. Cryst. Growth* **284,** 396 (2005).

16. Catledge, S. A. & Vohra, Y. K. Effect of nitrogen addition on the microstructure and mechanical properties of diamond films grown using high-methane concentrations. *J. Appl. Phys.* **86,** 698 (1999).

17. Cao, G. Z., Schermer, J. J., van Enckevort, W. J. P., Elst, W. A. L. M. & Giling, L. J. Growth of {100} textured diamond films by the addition of nitrogen. *J. Appl. Phys.* **79,** 1357 (1996).

18. Birrell, J. *et al.*. Bonding structure in nitrogen doped ultrananocrystalline diamond. *J. Appl. Phys.* **93,** 5606 (2003).

19. Western, C. M. PGOPHER, a program for simulating rotational structure. *Univ. Bristol* (2007).

20. Ma, J., Richley, J. C., Ashfold, M. N. R. & Mankelevich, Y. A. Probing the plasma chemistry in a microwave reactor used for diamond chemical vapor deposition by cavity ring down spectroscopy. *J. Appl. Phys.* **104,** 103305 (2008).

21. Mankelevich, Y. A., Ashfold, M. N. R. & Ma, J. Plasma-chemical processes in microwave plasma-enhanced chemical vapor deposition reactors operating with C/H/Ar gas mixtures. *J. Appl. Phys.* **104,** 113304 (2008).

22. Ma, J., Ashfold, M. N. R. & Mankelevich, Y. A. Validating optical emission spectroscopy as a diagnostic of microwave activated CH_4/Ar/H_2 plasmas used for diamond chemical vapor deposition. *J. Appl. Phys.* **105,** 043302 (2009).

23. Song, S., Hanson, R. K., Bowman, C. T. & Golden, D. M. A Shock Tube Study of the Product Branching Ratio of the NH_2 + NO Reaction at High Temperatures. *J. Phys. Chem. A* **106,** 9233 (2002).

24. Xu, Z.-F., Fang, D.-C. & Fu, X.-Y. Ab Initio Studies on the Dynamical Properties of the Reaction $NH(X^3\Sigma^-) + H \rightarrow N(^4S) + H_2$. *J. Phys. Chem. A* **101,** 4432 (1997).

25. Song, S. *et al.*. A shock tube study of the reaction $NH_2 + CH_4 \rightarrow NH_3 + CH_3$ and comparison with transition state theory. *Int. J. Chem. Kinet.* **35,** 304 (2003).

26. Moskaleva, L. V. & Lin, M. C. Theoretical Study of the NH_2+ C_2H_2 Reaction. *J. Phys. Chem. A* **102,** 4687(1998).

Chapter 6 Theoretical investigations for the reaction of O and N containing species on a diamond surface.

6.1. Reactions of O containing species on a diamond surface

6.1.1 Introduction

As has previously been discussed in this thesis, CH_3 radicals and H atoms are the main species responsible for diamond growth. This has been found experimentally, and with modelling.[1–4] The modelling of growth from gas phase carbon species onto a growing diamond surface in the presence of atomic H is therefore of great relevance to diamond CVD. The (100) 2x1 reconstructed surface describes the arrangement of C atoms on a flat diamond surface. The (100) 2x1 reconstructed surface forms after the relaxation of 2 C atoms on the (100) 1x1 surface forming a C-C bond. Both of these surface arrangements are shown in fig. 6.1 (a) and (b).

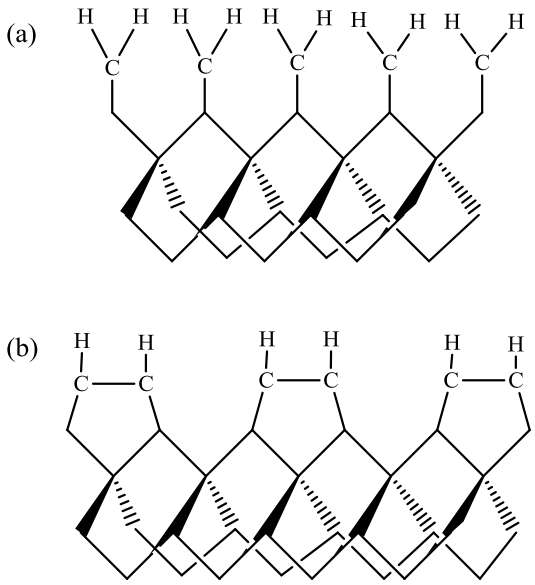

Fig. 6.1. Structures (a) and (b) represent the diamond (100) 1x1 unreconstructed and the (100) 2x1 reconstructed surfaces.

The surface C atoms in fig. 6.1 are H-terminated. H-termination is the preferred arrangement for the surface C-atoms, and gives the surface a negative electron

affinity.[5] The surface atoms will however undergo H-abstraction reactions forming surface radical sites at a rate of around 10^4-10^7 s^{-1}.[1] This then provides the surface radical sites to which gas phase radicals may adsorb. Many models have been proposed for the incorporation of carbon onto diamond radical sites. One idea proposed by Harris *et al.*, then by Butler involves the incorporation of carbon species into a trough[6,7] between 2 C-C dimers. Frenklach *et al.* also explored the possibility of C_2H_2 addition onto a diamond surface[8,9] but eventually proposed that the primary steps for growth on a (100) 2x1 reconstructed surface are most likely to proceed via addition of CH_3 onto a radical site on the C_2 surface dimer.[10,11] This brought about the standard growth model for diamond. A potential energy surface (PES) for this mechanism was investigated by Cheesman *et al.* and is shown in fig. 6.2.[12] Fig. 6.2 shows the elementary steps leading to the incorporation of a CH_2 group. The structures for the steps in the mechanism are labelled in fig. 6.2 as **1-7**, and all energies are quoted in kJ mol^{-1}. In this mechanism H atoms activate the diamond surface by the removal of a H atom, as seen between structures 1 and 2. This creates a dangling bond to which a gas phase CH_3 radical may adsorb as in structure **3**. If another gas phase H atom were to abstract a H atom from this chemisorbed CH_3 group as in structure **4**, this creates a surface CH_2 group which may then incorporate into the diamond lattice via the breaking of a C-C dimer bond, and subsequent formation of a C-C-C bridge, as between structures **5** and **6**.

Most of the steps involved in the incorporation of a CH_2 group into a C-C dimer bond in Cheesman's study were in agreement with other publications involving growth mechanisms of a similar nature on the diamond surface, involving CH_x addition to a pre-existing radical site.[13,14] Richley *et al.* investigated the direct insertion of C and CH and CH_2 (CH_x) groups into both C-H and C-C bonds.[15] It was found that the insertion of these H_x groups into a C-H bond is effectively a barrierless process, whereas the insertion into a C-C bond presents much higher barriers in comparison. However, the incorporation of carbon into diamond is more likely to proceed via a stepwise process, as in fig. 6.2. As well as the addition of groups to the surface, an important sequence of steps involved in diamond growth is in the migration of C_xH_y groups.

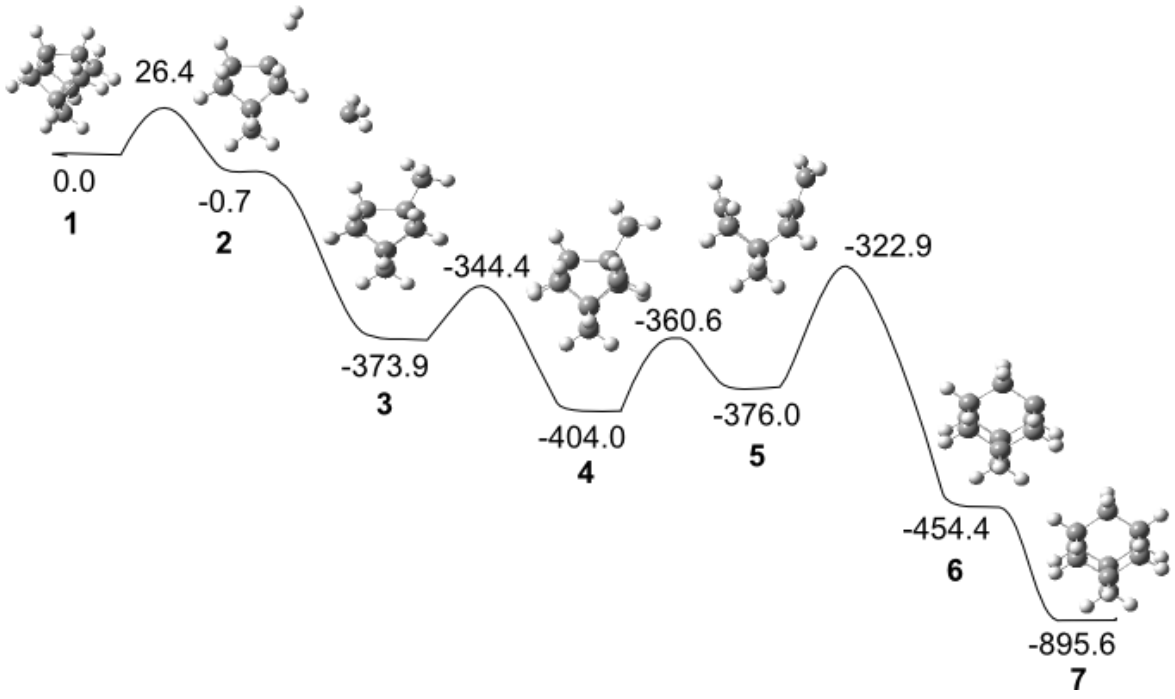

Fig. 6.2 The elementary steps leading to the incorporation of a CH_2 group on a diamond surface[12]. Energies (B3LYP QM/MM, 6-311G**) quoted in units of kJ mol^{-1}.

The migration of hydrocarbon groups is thought to be an important mechanism in CVD diamond growth and in the formation of a smooth diamond surface. Cheesman *et al.* investigated the migration of a CH_2 group along a dimer chain on the 2**x**1 (100) reconstructed H-terminated diamond surface,[12] in line with previous work by Frenklach *et al.*.[16] They found that, starting with a bridging CH_2 group, as **6** in fig. 6.2, this group can move along the surface dimer rows via a sequence of surface rearrangements. They also studied the migration of the CH_2 group across a dimer row, finding that this follows a lower energy path than for migration along the row. A diagram to show the direction of movement both along and across a (100) 2x1 reconstructed surface is shown in fig. 6.3. Tsuda *et al.*[17]l also mapped the PES for the migration both along and across a reconstructed diamond 2x1 (100) surface and found that migration across dimer rows also occurs at a lower energy than migration along the dimer row. A study by Larsson *et al.*[18] comparing different migrating groups also suggests CH_2 as the most likely migrating species on a diamond (111) rearranged surface. Larsson also emphasizes CH_3 as being the most likely radical for surface adsorption. Other theoretical migration studies include those for boron,[19] suggesting

that B and/or BH incorporation into diamond will proceed via steps similar to those for CH_2 as in fig. 6.2. However, there is still very little in the literature to explore PES's for the incorporation and migration of oxygen species on a diamond surface.

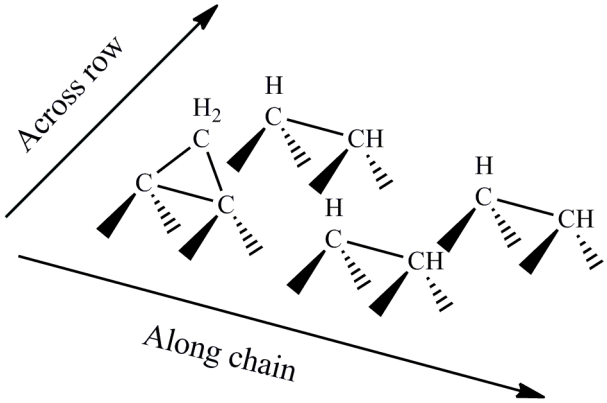

Fig. 6.3. The direction of movement for a CH_2 group along a dimer row vs across, on a (100) 2x1 reconstructed diamond surface.

When modelling surface reactions from C/H/O plasmas, it is important to consider which species are most likely to be interacting with the surface. The presence of OH radicals in $CH_4/CO_2/H_2$ gas mixtures means it is reasonable to assume that they should interact in some way with the growing diamond surface. Vandebulcke *et al.* used MBMS to study C/H/O plasmas and speculated that the lack of OH radicals in the gas phase vicinity of the growing surface indicates that it is incorporating into the diamond film.[20] Using the same technique, Petherbridge *et al.* attributed the lack of OH radicals to them simply being in low abundance, and undetectable at the surface. This may be due to the OH radical reacting to form other species such as H_2O. As discussed in Chapter 3, OH is calculated to be in reasonable abundance above the surfaced (100 x less than CH_3), and may therefore incorporate into diamond since it is analogous to the CH_3 radical electronically. Experimentally, EPR studies have only hinted at the presence of O in diamond,[21.22] however there is surprisingly little O incorporation within films grown with C/H/O plasmas. An attempt to model the mechanisms involved in O incorporation, and removal of O from the surface is given in this chapter.

6.1.2 Computational Methods

In this chapter, quantum mechanical (QM) and quantum mechanical/ molecular mechanical (QM/MM) calculations have been performed in order to determine the energies involved for the incorporation of O into a growing diamond surface. A C_9H_{14} cluster was used to represent a section of the (100) 2x1 reconstructed diamond surface. This was used as the base structure upon which to build upon, and calculate the potential energies of optimized geometries for the incorporation of O. An example of the cluster used is shown below in fig. 6.4.

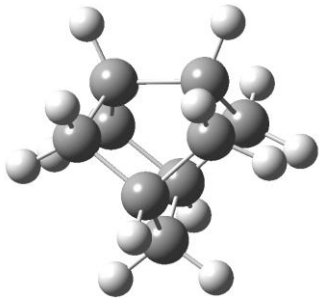

Fig. 6.4. C_9H_{14} cluster used for QM calculations. Calculated using B3LYP functional, 6-311G(d,p) basis set.

The geometries of structures at their minimum potential energies were obtained along the reaction coordinate using the Gaussian 09 program[23] and density functional theory (DFT). The B3LYP density functional was used with the 6-31G(d) basis set, and final energies come from higher basis set calculations using the larger basis set 6-311G(d,p). Whether a stationary point was calculated to be a transition state (TS) or not was confirmed by the calculation of vibrational frequencies. Vibrational frequencies also give the zero-point correction (ZPC). Single point energies were also calculated using the 6-311G(d,p) basis set. Single-point energies were also corrected using the ZPE. All energies are given in kJ mol^{-1}. As a guideline, reactions with calculated E_a<100 kJ mol^{-1} are considered to be feasible and potentially significant at the relevant substrate temperature (T_{sub}=1100-1200 K)

For QM/MM calculations, the QM region is embedded in a region calculated by MM. The MM region consists of a 5x9x4 slab with regards to bonds. The peripheral atoms of the slab are held frozen. The QM/MM framework is shown in fig. 6.5. Energies

returned by the QM/MM hybrid are more representative of reactions on the diamond surface. This is because the MM region prevents the small QM cluster region from minimizing to any unphysical geometry by virtue of the strain this would impose on neighboring MM atoms. Calculations on the QM region were performed using Jaguar,[24] and geometry optimization and energy of the MM region was calculated using TINKER.[25] The jobs for QM and MM regions were run using QoMMMa,[26] which also calculates the total QM/MM energy. Approximate transition states were calculated by following the energy along a reaction coordinate whilst changing either one or two bond lengths. The TS was the highest energy calculated along the reaction coordinate.

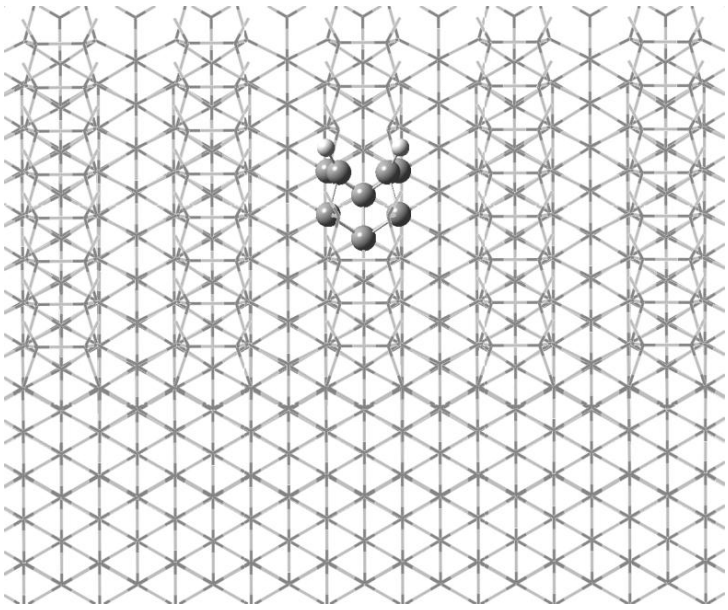

Fig. 6.5. C_9H_{14} cluster embedded in a 5x9x4 slab used for QM/MM calculations. Calculated using B3LYP, with a 6-311G(d,p) basis set.

6.1.3 Results and discussion

The purpose of this study is to model reactions of O containing species on a diamond surface. In order to relate this modelling to experimental work discussed with regards to $CH_4/CO_2/H_2$ plasmas in chapters 3 and 4, the OH radical is used to bind to the surface radical site, since this was studied by CRDS and companion 2-D modelling, which calculated the OH radical to be 100x less than CH_3 at the growing diamond surface. This can be seen in fig. 6.6 which is a mechanism showing reactions of O and OH on a (100) 2x1 reconstructed diamond surface using QM, DFT calculations, with

all energies quoted in kJ mol^{-1}. Activation of the surface in fig.6.6 was achieved using an OH radical, as opposed to a H atom. The addition of OH to the surface is analogous to the CH_3 radical addition step **3-4** in fig. 6.2, and is shown in fig. 6.6 between steps **2→3**. This is an energetically favourable process (ΔE=-401 kJ mol^{-1}). The initial H-abstraction reaction is exothermic (ΔE=-47 kJ mol^{-1}) and is calculated as a barrierless process. This sequence of steps leads to the adsorption of OH onto the surface as in fig. 6.6 structure **3**.

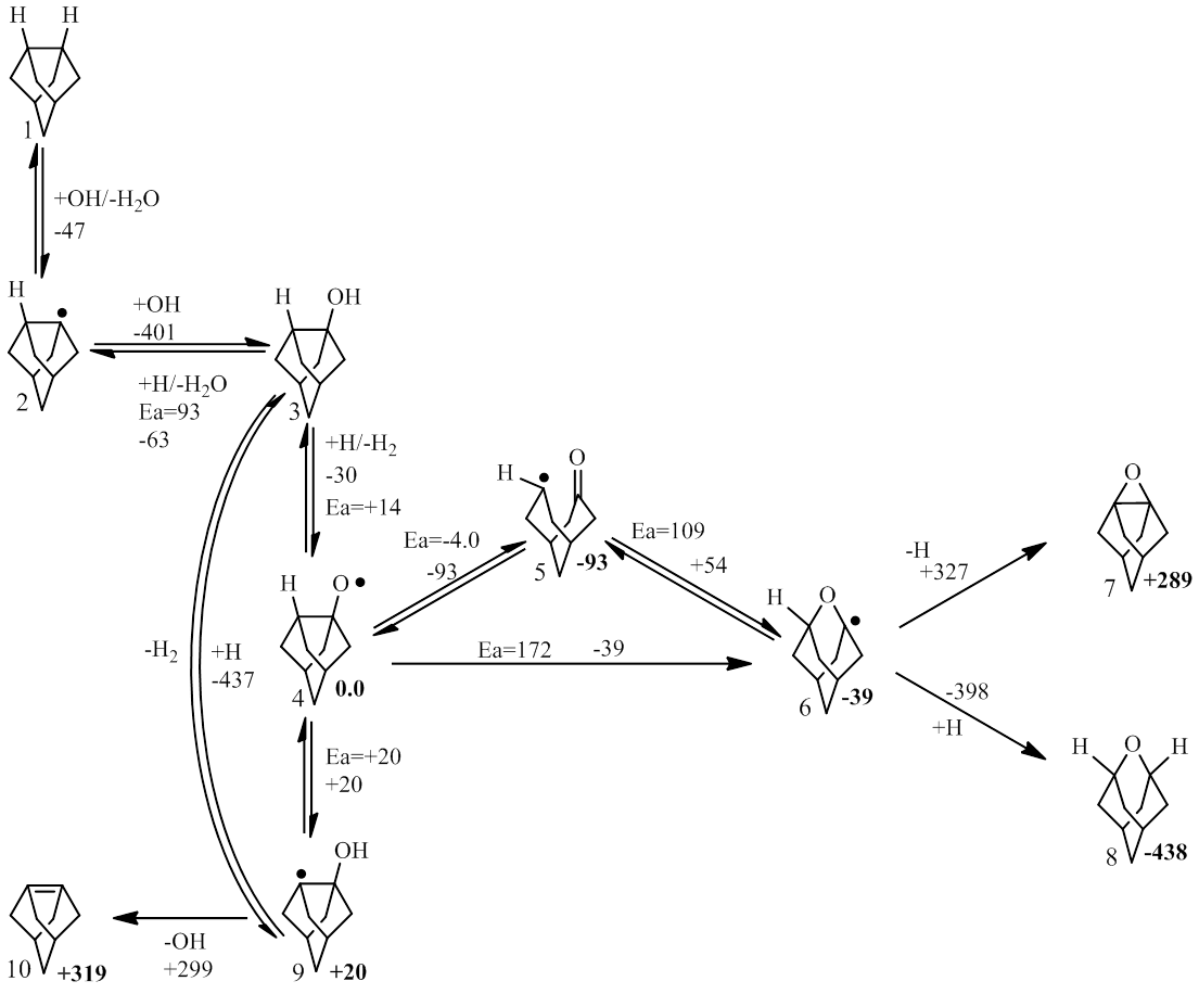

Fig.6.6 Reaction pathways calculated for the addition/loss and incorporation of an OH radical onto the diamond (100) surface calculated using QM, B3LYP, with a 6-311G(d,p) basis set. The structures are labelled with numbers to their bottom left. The numbers beneath the structures written in bold show calculated energies in kJ mol^{-1}, relative to the surface bound O radical. Reaction energies, and any activation energies (E_a) are included next to arrows linking reactants and products between each step.

The surface bound OH group in **3** can then either lose a H atom via reaction with a gas phase H atom and form structure **4**, or lose a H-atom from the surface C to (ΔE=-20 kJ mol^{-1}) to form structure **9**. Reaction **3→4** is exothermic, and has a small barrier (ΔE=-30 kJ mol^{-1}, E_a=14 kJ mol^{-1}). This reaction will only be dependent upon the H atom concentration above the surface and/or the unimolecular dissociation of H from the surface bound O radical. The dissociation of H was calculated to have ΔE=+400 kJ mol^{-1}, and is therefore extremely unlikely at surface temperature of 1200 K. The rate of a reaction can be estimated using an Arrhenius equation assuming a pre-factor of 10^{13} s^{-1} (for a molecular vibration) as ≈ 4 **x**10^{-4} s^{-1}. Once structure **9** is reached it will easily gain a H from the gas phase, or rearrange to form structure **4**. On formation of structure **4**, a series of rearrangements may take place; moving from structures **4→6** there is ring opening to form a ketone **(5)**, followed by ring closing to form a surface C-O-C group. The only substantial barrier in the ring opening/closing mechanism from the surface bound O radical is when moving from structure **5→6** with E_a=109 kJ mol^{-1} and ΔE=54 kJ mol^{-1}. However, this value is sufficiently close to 100 kJ mol^{-1} that it may be reasonable to be deemed a feasible process. Structure **6** may also be reached from structure **4**, however this was calculated to have a large barrier (E_a=172 kJ mol^{-1}) so is not seen as being energetically feasable. The addition of H to the ring closed cluster **6** then completes the reaction sequence to the incorporation of O into diamond. The equivalent ring closing step with boron is barrierless (ΔE = -121.5 kJ mol^{-1})[18] and that for CH_2 has a barrier at almost half the size, and is also exothermic (ΔE =
-78 kJ mol^{-1}, E_a = 50 kJ mol^{-1}) suggesting that, in comparison to B and C, O may be less likely to ring close and form the surface ether group. It may therefore be more favourable for the surface O to exist in the ring opened ketone group, although an equilibrium will exist between the O radical, ketone and surface ether structures.

The energetics for O incorporation were also calculated using QM/MM. The minimum energy reaction path for this is shown in fig. 6.7, where all energies are quoted in kJ mol^{-1}. For this reaction mechanism a H atom was used to activate the surface. Where energies are quoted in brackets, TS's have not yet been found and energies are quoted from QM calculations. Finding these TS's will be part of the future work section. Where there are no barriers present, the energy of the TS is below the energy of the starting reactant. Comparing with fig. 6.2, it is clear that the

QM/MM results are similar to those returned by QM calculations, in that the elementary reaction steps are still mainly exothermic, however the energies involved in surface rearrangements are lower. When moving from structure **4→5** in fig. 6.7, this has ΔE =-54.5 kJ mol^{-1}, whereas this step in fig. 6.6 using QM is around ΔE =-93 kJ mol^{-1}. Another difference comes from moving between **5→6**, where QM/MM calculates ΔE =+20 kJ mol^{-1}, whereas QM results show ΔE =+54 kJ mol^{-1}. These differences come from the influence the MM region has on the QM region. Without the MM framework, the QM region allows the 2 C atoms involved in the ring-opening mechanism between **4** and **5** to open further to ~ 2.98 Å than when using QM/MM (where the distance between the 2 C atoms is 2.51 Å). This means that the QM cluster embedded in the MM framework is in a preferable position for ring-closing and formation of the C-O-C group as in fig. 6.7 structure **6**, where the distance between the 2 C atoms in both cases closes to ≈ 2.3 Å. The energy given in brackets comes from QM calculations as this was not yet achieved using QM/MM.

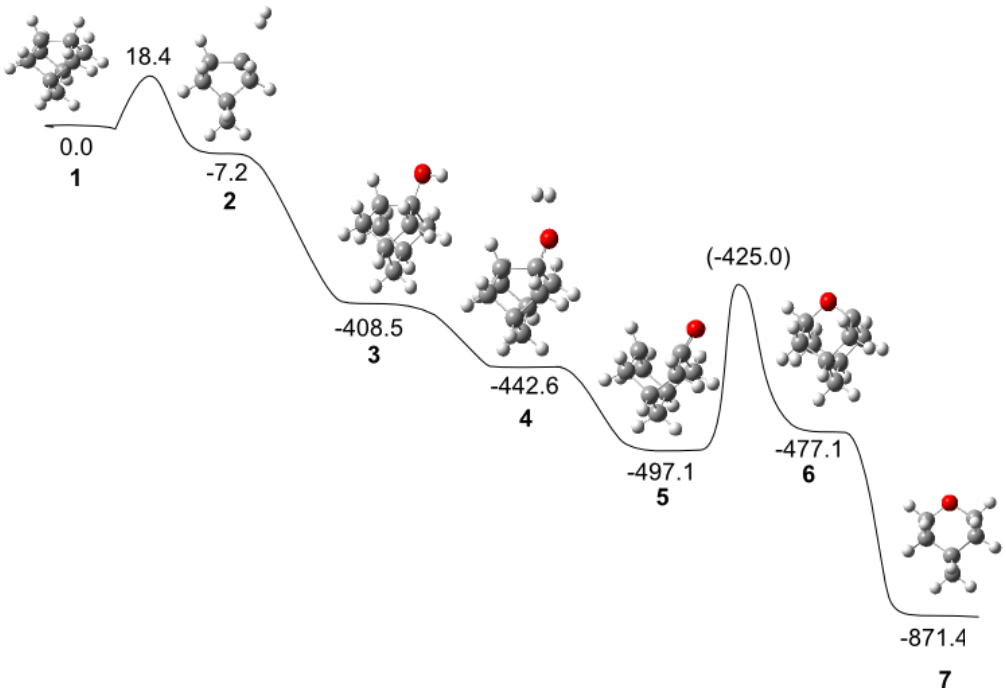

Fig. 6.7 The elementary steps leading to the incorporation O onto a diamond surface.[11] Energies (B3LYP QM/MM, 6-311G**) quoted in units of kJ mol^{-1}.

Although the present calculations suggest that O should incorporate into diamond, albeit with higher barriers in places than the analogous C and B insertion mechanisms, O is not found in abundance within diamond grown in C/H/O plasmas. This is

surprising considering the concentration of O containing species in the plasma. O must therefore be leaving the surface via one or more loss processes. These would be expected to be at lower energy than comparable loss processes for a surface bound CH_2, to account for the preferential incorporation of C relative to O.

The lack of O incorporation suggests that perhaps either one or several dominant loss processes occur before O has a chance to undergo the series of rearrangement steps which lead to its incorporation into diamond, as suggested by fig's. 6.6 and 6.7. Calculations show that a surface bound OH group may react with a gas phase H atom followed by the subsequent dissociation of H_2O, leaving a surface radical site. This process is entropically favorable and exothermic (ΔE=-63 kJ mol^{-1}), however calculations show an activation energy of E_a=86 kJ mol^{-1}. The PES for this process is shown in fig. 6.8, where all energies were calculated using DFT, and a QM $C_9H_{13}OH$ cluster, and are quoted in kJ mol^{-1}.

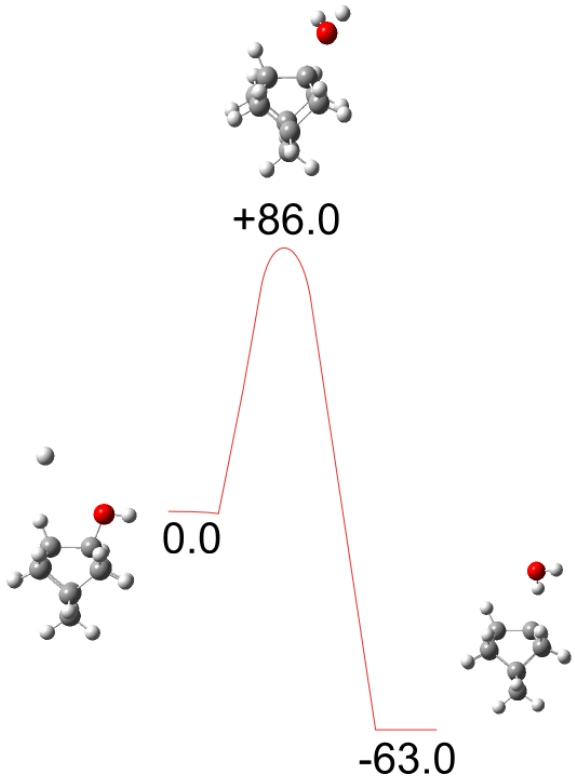

Fig. 6.8. $C_9H_{13}OH$ cluster QM calculation for the removal of OH from a (100) 2x1 reconstructed surface by a H atom. Energies are calculated using the DFT B3LYP, 6-311G(d,p) basis set and values quoted are in kJ mol^{-1}.

The competing reaction to this is shown in fig. 6.6, where the approaching H atom is involved in the abstraction of H from OH, creating the surface bound O radical. This

has a smaller barrier (E_a=14 kJ mol^{-1}), but does not have the same exothermicity, and will not be as entropically favorable.

6.2 Reactions of N containing species on a diamond surface

6.2.1 Introduction

Nitrogen is the most common defect found in natural diamond films, and is also prevelant in synthetically grown films. In the growth of synthetic films via CVD, the involvement of N in the gas phase has the ability to increase growth rate.[27,28] With regards to why the presence of N in the gas phase catalyzes growth, various models have been proposed.[29-31] There are two mechanisms which need discussion. The first involves the adsorption of an N containing species to the surface, and whether this may catalyse growth. Several groups have speculated that CN is involved in the growth process and is responsible for the increase in diamond growth rate,[32-34] although some propose that it is the adsorption of NH which that is important.[35,36] The second approach involves the incorporation of N into the diamond lattice below the H-terminated surface, and exploring how this may affect reactions on the surface.

One such model giving a possible explanation to the increase in growth rate due to the inclusion of N in a C/H growth environment was proposed by Butler *et al.*.[29] The proposed model is for growth on a (111) surface. They relate the increase in growth rate to the formation of a four-atom island with one CN group, and three CH_2 groups, in the nucleation of a new diamond layer. An example of this is shown in fig. 6.9. Structure **1** represents a section of a (111) surface, with the atoms involved in the formation of the island labeled **1→4**. Structures **2→7** represent the formation of the 4-atom island on a (111) surface, where energies for each process are quoted in kJ mol^{-1}. The addition of CN between structures **1** and **2** is exothermic (ΔE=-512.6 kJ mol^{-1}). Steps **3→4** and **5→6** both involve the addition of CH_3 groups and are also exothermic. Step **5→6** however is not as energetically favorable as step **3→4** due to steric hindrance imposed by the bridging NH group. The formation of the NH bridging group is the only endothermic step in the process (ΔE=+5.4 kJ mol^{-1}). This

island formation mechanism is dependent upon two CH_3 groups binding to the surface next to a CN group, or by CH_2 groups migrating towards it. A competing pathway would be H-atom adsorption to the surface bound CN group followed by a β-scission reaction resulting in the dissociation of CN. Adding to this however, they propose that a CN group on the surface will have a longer lifetime than a CH_2 group as it is most likely exempt from the beta-scission dissociation reaction. This would increase the lifetime of an adsorbed CN group, and provides a plausible explanation to the increase in growth rate on a (111) surface. Growth then occurs from migrating methyl radicals which may add to this island, resulting in growth outwards from the island, expanding the new layer.

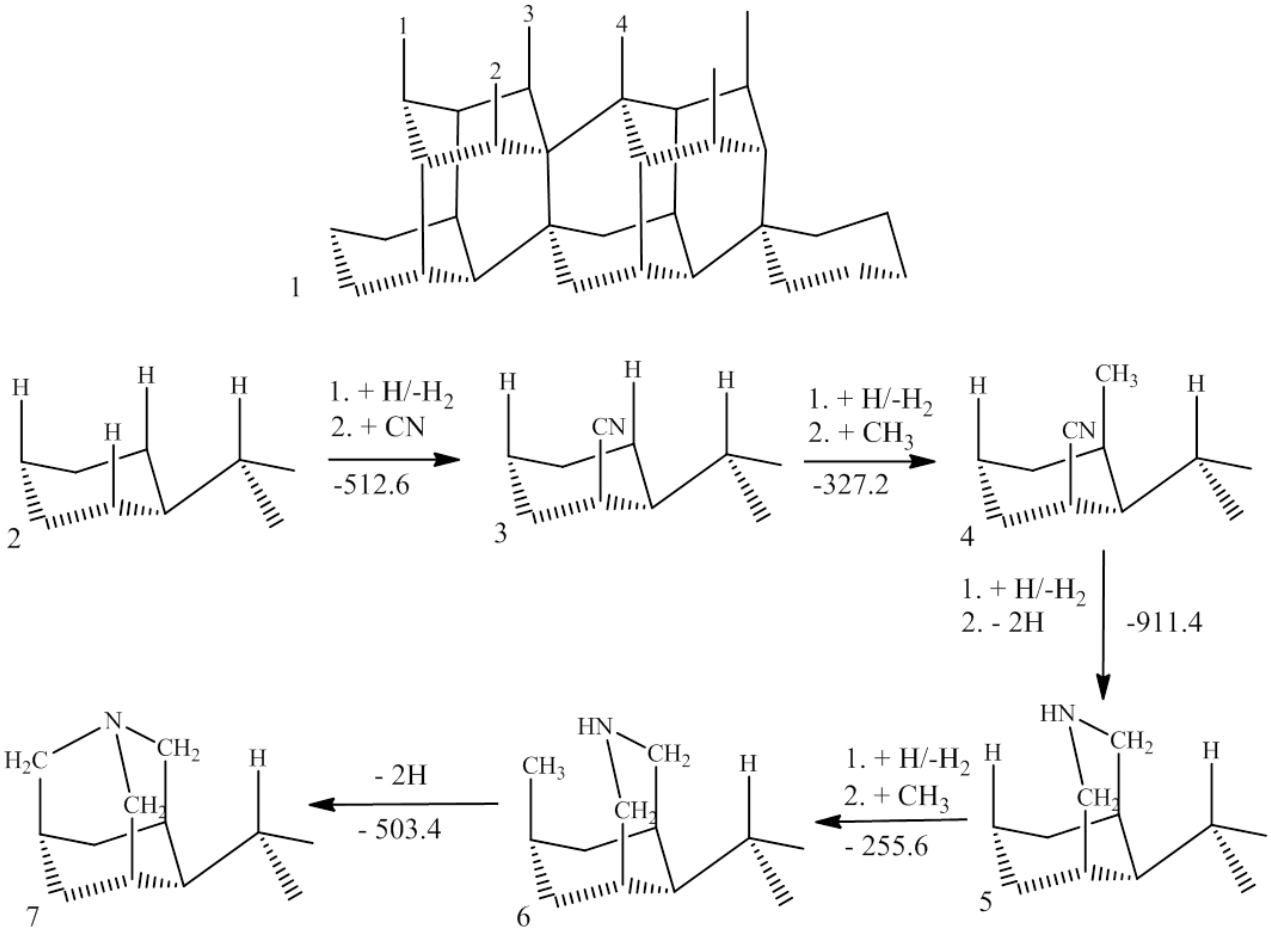

Fig. 6.9. Nucleation of a new diamond layer by formation of a 4 atom island[29]. Structure 1 represents a (111) surface connected to the layer beneath. Structures **2→7** give a mechanism for the formation of the 4-atom island. Energies calculated by DFT and quoted in kJ mol^{-1}.

A recent study by Yiming *et al.*[30] investigates N incorporation within the second layer below the H-terminated surface using DFT. They find that since N has 5 valence

electrons, it may form 4 bonds to neighbouring C atoms, but the extra electron will occupy an antibonding orbital, which results in breakage of the N-C bond. The extra electron density from the nitrogen is shown to be distributed amongst the top layer of C-H bonds which serves to weaken the C-H bond and remove any barriers to H-abstraction. An illlustion of the additional electron density between the C-H bond with an N atom (blue) in the 2nd layer below C (grey) is shown in fig. 6.10. On removal of the C-H bond, the extra electron can form a surface electron pair, and the N-C bond can re-form.

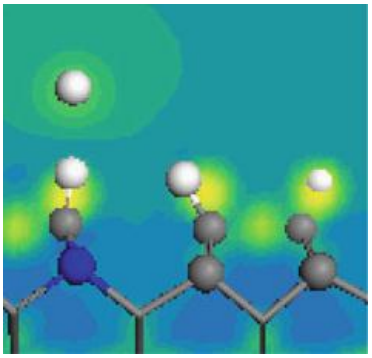

Fig 6.10. Illustration of the additional electron density between the C-H bond with an N atom (blue) in the 2nd atomic layer below C (grey) with an approaching H atom (white).[30]

Frauenheim *et al.*[31] propose a mechanism similar to Yiming *et al.* for the increase in growth rate for growth on a (100) surface; proposing a model for how the incorporation of N in diamond may increase growth rate, by decreasing the energetics involved in the growth process. They propose that an N sitting below the surface catalyses (100) growth by transferring an electron into a reconstructed surface C-C bond. This then lengthens the C-C bond, and makes it more attractive to CH_x adsorption. After adsorption, the lengthened surface C-C dimer encourages the adsorbed CH_2 group to form a bridge, where the dimer bond breaks. The dopant electron then saturates the C-C-C bridge, and is transferred to the next C-C dimer in the row, and the process continues.

From the growth mechanism proposed by Yiming *et al.*[30] and Frauenheim *et al.,*[31] using nitrogen to increase the growth rate of diamond should not be achieved without the incorporation of N into substitutional sites within the diamond lattice. It has been

proposed that the substitution of a nitrogen atom in place of a carbon atom in diamond should be 3-fold coordinate.[37,38] Zapol *et al.*[38] propose that N is more likely to substitute into grain boundaries (GB) rather than in the bulk due to an increased local disorder. This makes it easier for the N to move out of plane of the sp^3 diamond framework and allows substitution to occur at a lower energy.

Kajihara *et al.* calculated the energy of a N defect in the (111) direction[39] as shown in fig. 6.11. They calculated that the substituted nitrogen lone pair and the carbon dangling bond repel each other, and that there is an increase in bond length of up to 25% between the nitrogen and carbon. The original positions of these atoms are where the 'x' labels are. Deviations from the atom's original positions can be seen by the sketched positions of the white atoms (which represents N) and the black atoms opposite (which represents C).

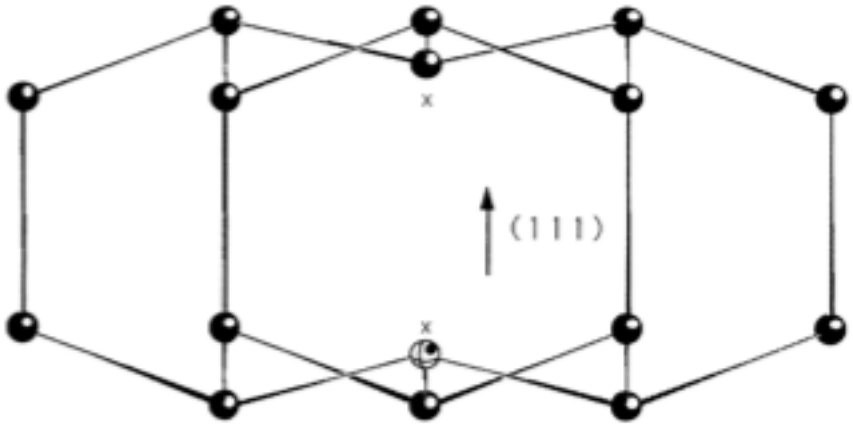

Fig. 6.11. Diagram showing relaxation around the substitutional N in the (111) direction, of both N and C atoms, due to repulsion between the N lone pair and the C dangling bond. The white atom represents nitrogen and the black atoms represent carbon. The 'x' labels represent the positions the nitrogen and carbon atoms were in before relaxing. The increase in bond length is 25%.[39]

In the present study, the energetics involved for reactions of both NH and CN on a diamond (100)-reconstructed surface have been calculated. This has given insight into the most likely routes for N incorporation, and indicates which species are most likely to influence the growth rate with the addition of N.

6.2.2 Results and Discussion

In a plasma environment containing C/H/N, there will be many different nitrogen containing species. Possible gas phase species above the growing surface are CN, HCN, CNH, N and NH_x (x=1-3). The PES's for the addition and incorporation of some of these species into diamond are explored in the following section. The calculations are QM and use DFT with the same methodology as described for QM calculations in section 6.1.2.

As CH_x radicals are the main species responsible for the incorporation of C and growth of diamond, it is reasonable to assume that NH_x species may be a source for the incorporation of N into diamond. Fig. 6.12 shows reaction mechanisms for the addition of N, NH and NH_2 to a diamond surface radical site. Energies are quoted in kJ mol^{-1}, and the structures are labeled with numbers written in bold. Activation of the surface by atomic H is an exothermic process with a small barrier. Three pathways are then calculated for the addition of N, NH and NH_2 radicals to the surface. The addition of N from structures **2→7** being most exothermic (ΔE=-612.1 kJ mol^{-1}), followed by NH from **2→4** (ΔE=-559.7 kJ mol^{-1}) and NH_2 from structures **2→3** (ΔE=-354.9 kJ mol^{-1}). These surface bound species can then undergo H-addition/abstraction reactions with H atoms, for which the energies are given when moving between structures **3**, **4** and **7**. Both the addition and abstraction of H atoms to these structures are exothermic, and so an equilibrium will exist between the adsorbed N, NH and NH_2 species, with atomic H present in the gas phase. Reaction mechanisms for the incorporation of N via the ring opening and closing mechanism are given for both N and NH species.

The surface-bound NH_2 species will undergo a H-abstraction to form the surface radical required to incorporate into the growing surface. Incorporation via a surface bound NH radical is given from structures **4→5→6→11** in fig. 6.12. The first ring opening reaction from **4→5** has no change in energy and a small barrier (E_a=+25.6 kJ mol^{-1}). The ring-closing step between **5→6**, although exothermic (ΔE=-19.0 kJ mol^{-1}), has a large barrier (E_a=205.2 kJ mol^{-1}). Since reaction involving abstraction energies above 100 kJ mol^{-1} can be viewed as being impossible at surface

temperatures of 1200 K, this reaction is not favorable. The barrier for direct ring opening/closing between **4→6** is also large (E_a=256.6 kJ mol^{-1}) and therefore this is also an unlikely process. This eliminates the surface NH radical species as a likely species for N incorporation

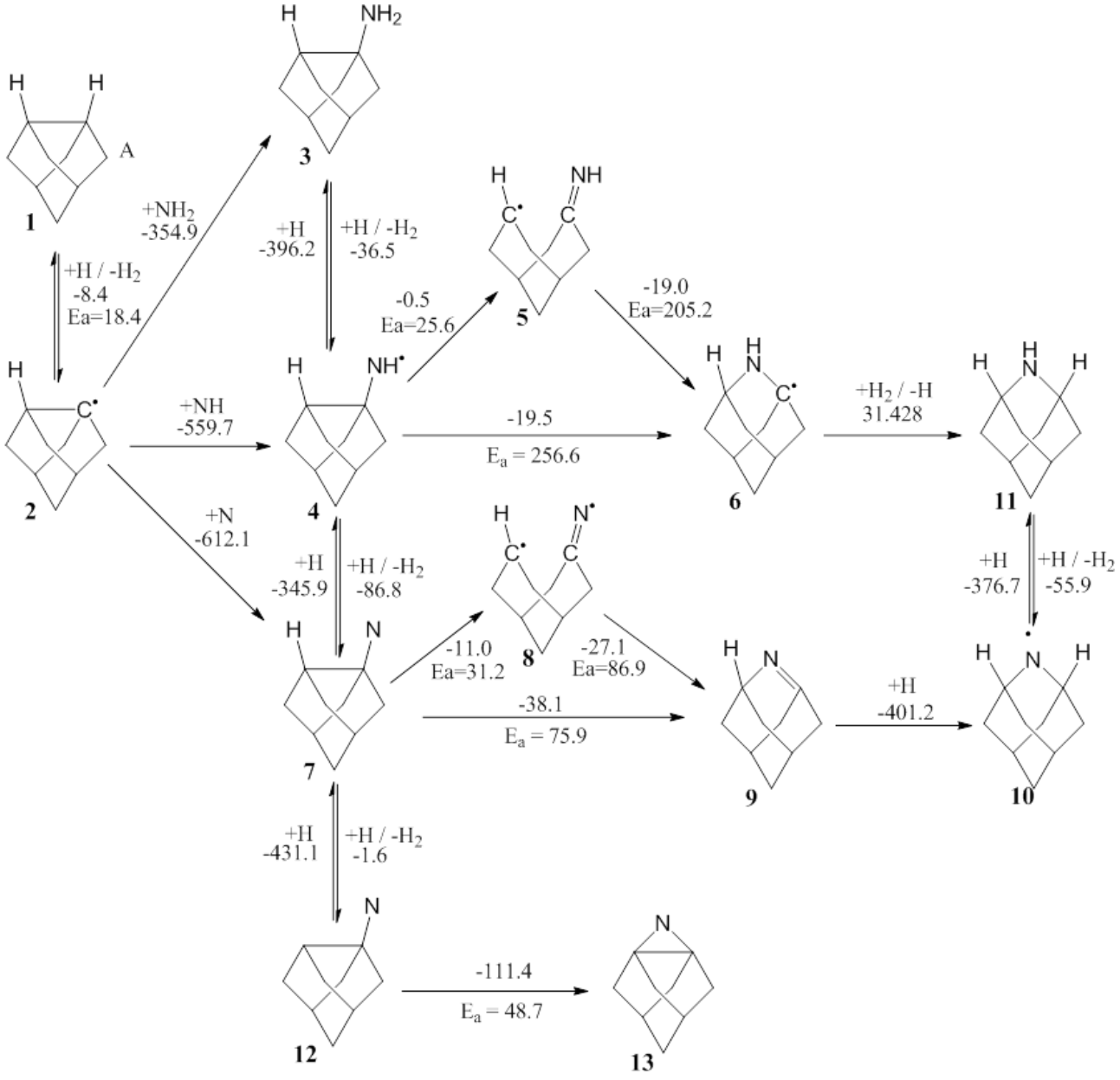

Fig. 6.12 Reaction pathways calculated for the incorporation of NH_x species onto the diamond (100) 2x1 rearranged surface, calculated using QM, B3LYP, with a 6-311G(d,p) basis set. The structures are labeled with numbers to their bottom left. Reaction energies, and any activation energies (E_a) are included next to arrows linking reactants and products between each step. All energies are quoted in kJ mol^{-1}.

The energetics involved for the incorporation of a surface bound N diradical species is shown in fig. 6.13 between structures **7→8→9→10→11**. The ring opening step from structures **7-8** is mildly exothermic (ΔE=-11.0 kJ mol^{-1}) with a small barrier (E_a=31.2 kJ mol^{-1}). The ring closing step from structures **8→9** is also exothermic with a barrier (ΔE=-27.1 kJ mol^{-1}, Ea=86.9 kJ mol^{-1}). The direct ring opening/closing step between structures **7→9** is also energy favourable with a barrier (ΔE=-38.1 kJ mol^{-1}, E_a=75.9 kJ mol^{-1}). Both barriers for the incorporation of N are below 100 kJ mol^{-1} and can therefore be expected to occur under typical CVD growth conditions. There will be an equilibrium between structures **7**, **8**, and **9** on the surface. Addition of 2H atoms over the C=N bond in structure **9** moving towards structure **11** results in the complete incorporation of NH. The process for N incorporation is exothermic, and its PES can be seen in fig. 6.13. Fig. 6.13 shows the exothermicity of the process, which has only three small barriers. All energies are quoted in kJ mol^{-1}. Surface activation occurs from **1→2** followed by N addition in **3**. Moving from **7→8→9** shows the energy favorable ring opening/closing steps. Structures **10** and **11** show the addition of 2xH atoms for the final inclusion of NH. Incorporation of nitrogen via NH_x species from these QM calculations can now be viewed in terms of rearrangements of a surface N radical species. There are, however, other species which exist above the growing surface that may have the ability to react and incorporate N into diamond, such as CN, HCN and C.

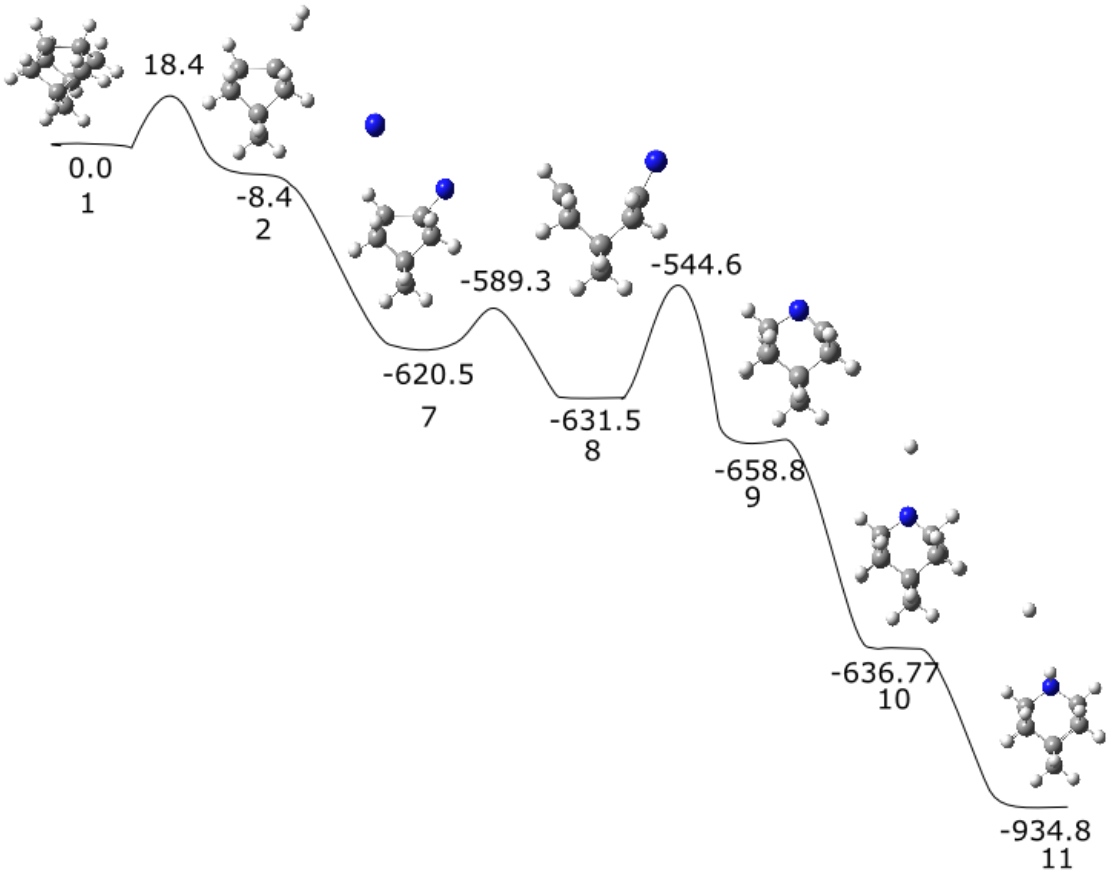

Fig. 6.13. PES for incorporation of N into the diamond (100) 2x1 rearranged surface calculated using QM, B3LYP, with a 6-311G(d,p) basis set. All energies are quoted in kJ mol^{-1}.

In a C/H/N plasma, HCN is expected to be one of the most stable species. H-abstraction from HCN gives CN, which will exist in the plasma. Another species that can be derived from HCN is the CNH isomer. An equilibrium will exist between these two species, however due to its stability this equilibrium is expected to sit strongly in favor of HCN. A detailed mechanism showing the incorporation of CN and CNH/HNC species is shown in fig. 6.14. These QM calculations use DFT, and the B3LYP functional with a 6-311G (d,p) basis set, and all energies are quoted in kJ mol^{-1}. The structures are labeled **1-12**. Structure **2** is reached after surface activation with a H-atom from structure **1**. This creates a radical site, for which the energy favorable adsorptions of CN and CNH have been calculated to form structures **3** and **8** (ΔE=-517.8 kJ mol^{-1} and -104.9 kJ mol^{-1}). From structure **3**, structure **6** can be reached (ΔE=-4.5 kJ mol^{-1}) for which the direct ring closure to form an

incorporated CN group without a ring opening step is highly endothermic and has a large barrier, so is not expected to occur (ΔE=132.2 kJ mol^{-1}, E_a=411.8 kJ mol^{-1})

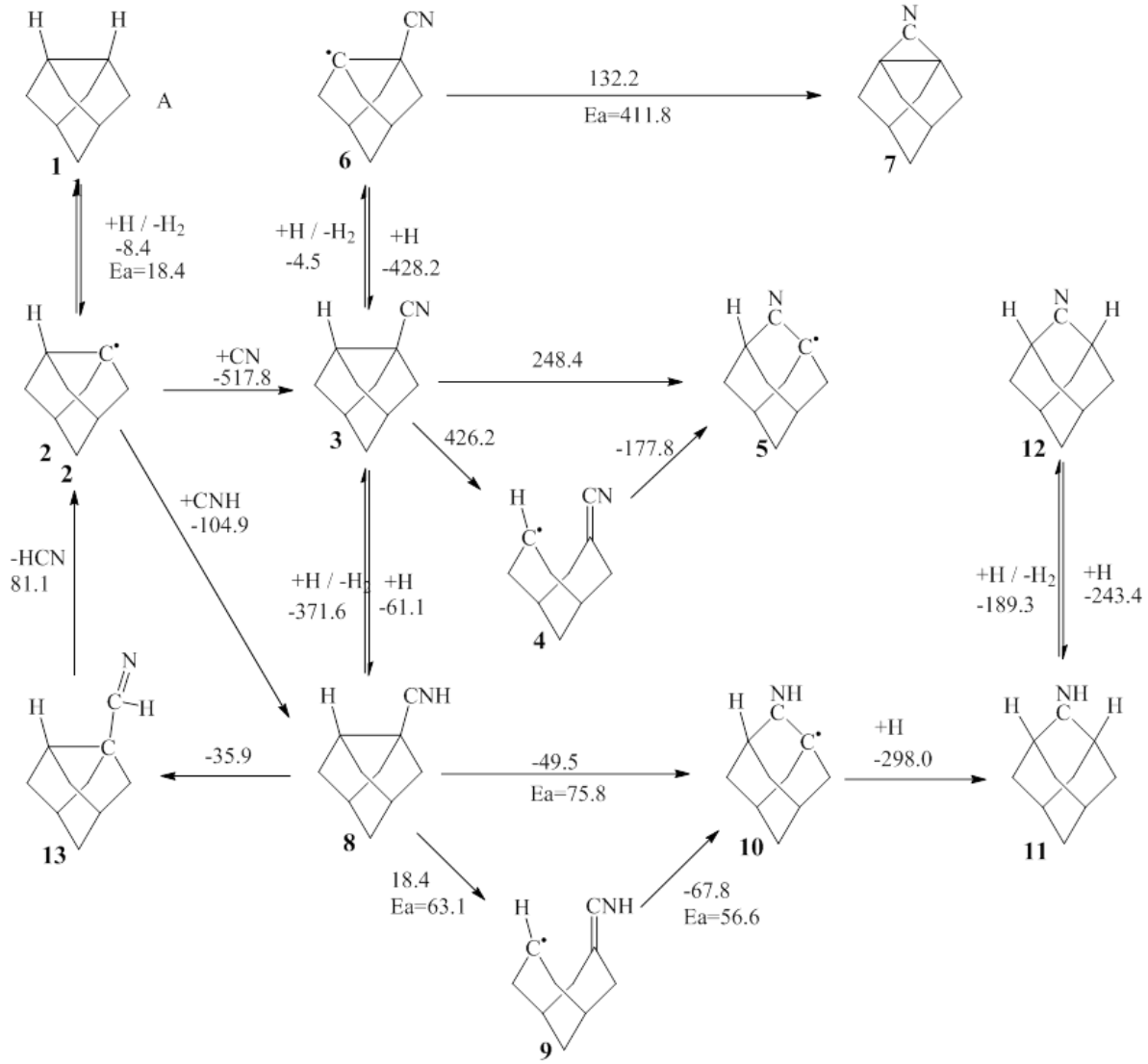

Fig. 6.14 Reaction pathways calculated for the incorporation of CN and CNH species onto a diamond (100) 2x1 rearranged surface, calculated using QM, B3LYP, with a 6-311G(d,p) basis set. The structures are labeled with numbers to their bottom left. Reaction energies, and any activation energies (E_a) are included next to arrows linking reactants and products between each step. All energies are quoted in kJ mol^{-1}.

After the succesful adsorption of a CN radical to the surface, calculations show that it is unlikely to undergo ring opening and closing steps which would lead to its incorporation. This is because the ring opening step, moving between structures **3→4** is highly endothermic (ΔE=426.2 kJ mol^{-1}) which restricts the formation of the ring opened structure **4**. The energy for the direct opening and closing step was also

calculated to be endothermic (ΔE=248.4 kJ mol^{-1}). Since the rate of surface interactions with H atoms are expected to be 10^4-10^7 s^{-1}, the adsorbed CN is likely to interact with a gas phase H atom to form a surface CNH group. The addition of an H atom as when moving from structures **3** to **8** is calculated to be an exothermic process with ΔE=-61.1 kJ mol^{-1}. After formation of the surface CNH group, the ring-opening step between structures **8→9** is only mildly endothermic, and has a barrier below 100 kJ mol^{-1} (E_a=63.1 kJ mol^{-1}). The ring-closing step between structures **9→10** is exothermic, and also presents a small barrier (ΔE=-67.8 kJ mol^{-1}, E_a=56.6 kJ mol^{-1}). The addition of a H atom to the C radical in structure **10** forms structure **11**, of which the removal of a H atom is seen to be an exothermic process (ΔE=-189.3 kJ mol^{-1}). Structure **8** can also be reached by exothermic reaction of structure **2** with a gas phase CNH species. However, the CNH radical is expected to be in extremely low abundance in the gas phase, as there will be an equilibrium: CNH ↔ HCN, which will lie strongly in favour of the stable HCN molecule.

A competing reaction pathway to **8→12** is when considering reaction **8→13** with the transfer of the H from the N to the C of the CN group in the formation of a surface bound CHN group. The desorption of this is an endothermic process when moving from structure **13-2** (ΔE=81.1 kJ mol^{-1}), which makes this pathway plausible. However, due to steric hinderance, the H atom is most likely to prefer being attached to N. The PES for stages **1→2→3→8→9→10→11** is shown in fig. 6.15. This specific pathway has been chosen because CN is likely to be in abundance at the growing surface, however incorporation via adsorption of the CNH species is also energetically favorable. The route which involves CN adsorption therefore offers a low energy route to adding the CNH species to a surface radical site. All energies in fig. 6.15 come from fig. 6.14, calculated using QM methods with DFT, and are quoted in kJ mol^{-1}. This PES serves to illustrate how this process is feasible.

The successful formation of structure **12** in fig. 6.14 from CN species provides an N atom which sits above the growing layer. If the CN group were to become incorporated as shown, the N atom above the new plane could provide the source needed for nucleation of the next layer if say, a migrating CH_2 group were to bind to it and form an island similar to that proposed by Butler *et al.*[29] as in fig. 6.9.

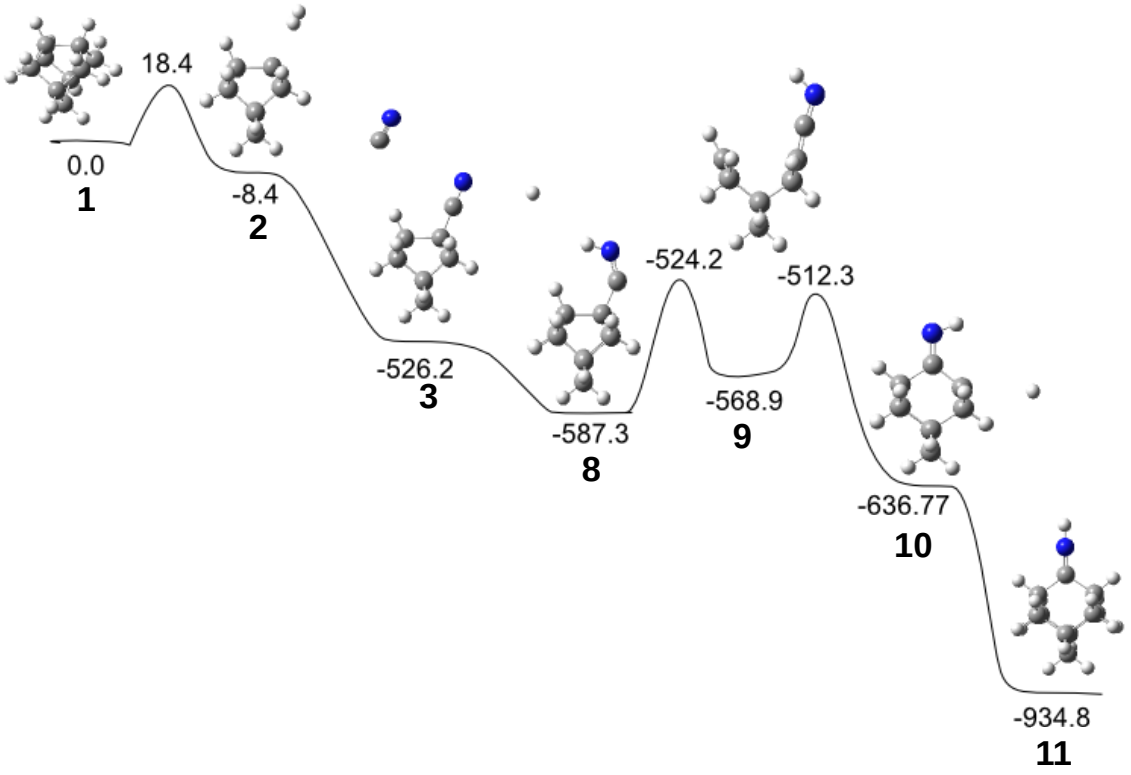

Fig. 6.15. PES for incorporation of CN into the diamond (100) 2x1 rearranged surface calculated using QM, B3LYP, with a 6-311G(d,p) basis set. All energies are quoted in kJ mol^{-1}.

6.3 Conclusions

Reaction mechanisms have been calculated for the incorporation of O and N containing species onto a (2x1) reconstructed (100) diamond surface. Calculations show that there are energetically plausible pathways for incorporation of these species at surface temperatures of 1200 K. Experimentally, however N is found in grown films yet there is little evidence for the presence of O. Pathways for the removal of O from the surface have been explored, but the calculated pathways suggest that O should incorporate into diamond. None of the surface reactions present a low enough energy pathway to account for the lack of O found experimentally.

With regards to N containing species, pathways have been found which may lead to its incorporation into films via surface bound CNH and N species. The CN route found for N incorporation provides an N atom which sits 1-atom above the growing layer, which could provide the atom necessary for triggering nucleation of subsequent layers. The recent study by Yiming *et al.*[30] suggest that the dominant contribution to the increase in G more than likely comes from an incorporated N in the first several layers below the H-terminated surface, and how this lowers the the energetics involved in surface activation. However, Yiming *et al.* do not suggest a route to which sub-surface N atom got there in the first place, which this study does.

6.4 References

1. Mankelevich, Y. A., Ashfold, M. N. R. & Ma, J. Plasma-chemical processes in microwave plasma-enhanced chemical vapor deposition reactors operating with C/H/Ar gas mixtures. *Journal of Applied Physics* **104,** 113304 (2008).

2. Harris, S. J., Weiner, A. M. & Perry, T. A. Measurement of stable species present during filament-assisted diamond growth. *Applied Physics Letters* **53,** 1605 (1988).

3. Harris, S. J. & Martin, L. R. Methyl versus acetylene as diamond growth species. *Journal of Materials Research* **5,** 2313 (2011).

4. May P W, Mankelevich, Y. A. Experiment and modelling of the deposition of ultrananocrystalline diamond films using hot filament chemical vapor deposition and $Ar/CH_4/H_2$ gas mixtures: A generalized mechanism for ultrananocrystalline diamond growth. *Journal of Applied Physics* **100,** 024301 (2006).

5. Van der Weide, J. *et al.* Negative-electron-affinity effects on the diamond (100) surface. *Phys. Rev. B* **50,** 5803 (1994).

6. Butler J. E., Woodin, R. L., Brown, L. M. & Fallon, P. Thin Film Diamond Growth Mechanisms [and Comment]. *Philosophical Transactions of the Royal Society A: Mathematical, Physical and Engineering Sciences* **342,** 209 (1993).

7. Harris, S. J. Mechanism for diamond growth from methyl radicals. *Applied Physics Letters* **56,** 2298 (1990).

8. Huang, D. Energetics of acetylene-addition mechanism of diamond growth. *The Journal of Physical Chemistry*, **92,** 6379 (1988)

9. Skokov S, Weiner, B. & Frenklach, M. Chemistry of Acetylene on Diamond (100) Surfaces. *The Journal of Physical Chemistry*, **99**, 5616 (1995)

10. Huang D, Frenklach M, Potential energy calculations of diamond growth by methyl radicals. *The Journal of Physical Chemistry* **95,** 3692 (1991).

11. Skokov, S., Weiner, B. & Frenklach, M, Elementary reaction mechanisms for growth of diamond (100) surfaces from methyl radicals, *The Journal of Physical Chemistry*, **98**, 7073 (1994).

12. Cheesman, A., Harvey, J. N., & Ashfold, M. N. R. Studies of carbon incorporation on the diamond [100] surface during chemical vapor deposition using density functional theory. *The journal of physical chemistry. A* **112,** 11436 (2008).

13. Tamura, H. & Gordon, M. S. Ab initio study of nucleation on the diamond (100) surface during chemical vapor deposition with methyl and H radicals. *Chemical Physics Letters* **406,** 197 (2005).

14. Kang, J. K. & Musgrave, C. B. A theoretical study of the chemical vapor deposition of (100) diamond: An explanation for the slow growth of the (100) surface. *The Journal of Chemical Physics* **113,** 7582 (2000).

15. Richley, J. C., Harvey, J. N. & Ashfold, M. N. R. On the role of carbon radical insertion reactions in the growth of diamond by chemical vapor deposition methods. *The journal of physical chemistry. A* **113,** 11416 (2009).

16. Frenklach, M., Skokov, S., Park, U. V & Pennsyl, V. Surface Migration in Diamond Growth. **5647,** 3025 (1997).

17. Tsuda, M., Hata, M. & Oikawa, S. Adatom migrations and nucleations on reconstructed (001) surfaces II. Diamond. *Applied Surface Science* **107,** 116 (1996).

18. Larsson, K. & Carlsson, J.-O. Surface migration during diamond growth studied by molecular orbital calculations. *Physical Review B* **59,** 8315 (1999).

19. Cheesman, A., Harvey, J. N. & Ashfold, M. N. R. Computational studies of elementary steps relating to boron doping during diamond chemical vapour deposition. *Physical Chemistry Chemical Physics* **7,** 1121 (2005).

20. Gries, T., Vandenbulcke, L., de Persis, S., Aubry, O. & Delfau, J. L. Diagnostics and modelling of CH_4–CO_2 plasmas for nanosmooth diamond deposition: Comparison to experimental data. *Journal of Vacuum Science & Technology B: Microelectronics and Nanometer Structures* **27,** 2309 (2009).

21. Hill, G. J., van Wyk, J. A. & Hoch, M. J. R. EPR of oxygen centres in natural diamond. *Radiation Effects and Defects in Solids* **156,** 221 (2001).

22. Goss, J., Briddon, P., Rayson, M., Sque, S. & Jones, R. Vacancy-impurity complexes and limitations for implantation doping of diamond. *Physical Review B* **72,** 035214 (2005).

23. Frisch, M., Trucks, G., Schlegel, H. & Scuseria, G. *et al.*, Gaussian 09, Gaussian, Inc., Pittsburgh, PA, 2009;

24. Ringnalda, M. Jaguar; Schroedinger Inc. *Portland, OR* (1997)

25. Ponder, J. TINKER: Software tools for molecular design. *Washington University School of Medicine, Saint Louis, MO* (2004)

26. Harvey, J. N. Spin-forbidden CO ligand recombination in myoglobin. *Faraday Discussions* **127,** 165 (2004).

27. Yan, C. Very high growth rate chemical vapor deposition of single-crystal diamond. *Proc. Natl. Acad. Sci.* **99,** 12523 (2002).

28. Vandevelde, T., Nesladek, M., Quaeyhaegens, C. & Stals, L. Optical emission spectroscopy of the plasma during microwave CVD of diamond thin films with nitrogen addition and relation to the thin film morphology. *Thin Solid Films* **308,** 154 (1997).

29. Butler, J. E. & Oleynik, I. A mechanism for crystal twinning in the growth of diamond by chemical vapour deposition. *Philos. Trans. A. Math. Phys. Eng. Sci.* **366,** 295, (2008).

30. Yiming, Z., Larsson, Larsson, F., Effect of CVD diamon d growth by doping with nitrogen. *Thero. Chem. Accounts. (in press)*

31. Frauenheim, T. *et al.*. A molecular dynamics study of N-incorporation into carbon systems: Doping, diamond growth and nitride formation. *Diam. Relat. Mater.* **7,** 348 (1998).

32. Vandevelde, T. *et al.*. Correlation between the OES plasma composition and the diamond film properties during microwave PA-CVD with nitrogen addition. *Thin Solid Films* **340,** 159 (1999).

33. Dandy, D. S. Influence of the gas phase on doping in diamond chemical vapor deposition. *Thin Solid Films* **381,** 1 (2001).

34. Bhattacharyya, S. *et al.*. Synthesis and characterization of highly-conducting nitrogen-doped ultrananocrystalline diamond films. *Appl. Phys. Lett.* **79,** 1441 (2001).

35. Chayahara, A. *et al.*. The effect of nitrogen addition during high-rate homoepitaxial growth of diamond by microwave plasma CVD. *Diam. Relat. Mater.* **13,** 1954 (2004).

36. Cao, G. Z., Schermer, J. J., van Enckevort, W. J. P., Elst, W. A. L. M. & Giling, L. J. Growth of {100} textured diamond films by the addition of nitrogen. *J. Appl. Phys.* **79,** 1357 (1996).

37. Jin, S. & Moustakas, T. D. Effect of nitrogen on the growth of diamond films. *Appl. Phys. Lett.* **65,** 403 (1994).

48. Zapol, P., Sternberg, M., Curtiss, L., Frauenheim, T. & Gruen, D. Tight-binding molecular-dynamics simulation of impurities in ultrananocrystalline diamond grain boundaries. *Phys. Rev. B* **65,** 045403 (2001).

49. Kajihara, S., Antonelli, A., Bernholc, J. & Car, R. Nitrogen and potential n-type dopants in diamond. *Phys. Rev. Lett.* **66,** 2010 (1991).

Chapter 7 Thesis summary

7.1 Overview

The gas phase and surface chemistry of both O and N containing species, which is involved in MWPECVD of diamond films from H/C/O and H/C/N gas mixtures, has been studied, using a combination of computational and experimental techniques.

CRDS and OES, in combination with 2-D (r,z) plasma modelling, were used to study the gas phase chemistry in $CH_4/CO_2/H_2$ and CO/H_2 plasmas. It was found that with increasing $X_{C/\Sigma}$, in a plasma with $X_0(H_2)$=0.3 and 0.6, emissions and column densities of C_2 and CH increased when crossing $X_{C/\Sigma}$=0.5, and those of OH decreased. It was found that unlike conventional C/H plasmas, C/H/O plasmas contain peripheral regions around the hot plasma core that are rich in C_xH_y and/or OH_x species. These act as sources of C and O radicals which feed into the plasma centre, which ultimately react to form CO and H_2. When C>O in the input feed gas mixture, C containing species exceed those of O containing species in the peripheral regions, and diamond growth is achieved. The opposite effect occurs if O>C, which results in no growth. When the mole fraction of H_2 in the feed gas was increased, such that $X_0(H_2)$=0.95, the plasma was found to resemble that of C/H gas mixtures; there were no peripheral regions for the mutual destruction of C_xH_y and OH_y species. In moving from $X_0(H_2)$=0.3 to $X_0(H_2)$=0.95, with $X_{C/\Sigma}$=0.5, the plasma modelling showed n_e shifting from an annular region slightly outside the plasma core, into the plasma core. This is because, when $X_0(H_2)$=0.3, n_e follows the localisation of H_3O^+, since H_3O^+ has a lower ion-electron recombination rate than $C_2H_2^+$.

CO/H_2 gas mixtures were studied, and it was found that CH and OH concentrations were much lower in these gas mixtures. This reflects the strength of the CO bond. CO is one of the most thermodynamically stable products in the plasma. Without the CH_4/CO_2 combination, the plasma lacked the peripheral regions in which CH_x radicals form, which are responsible for diamond growth. Diamond films were also grown, from which it was clear from the size of crystalline facets, that optimum growth in a $CH_4/CO_2/H_2$ was achieved when $X_{C/\Sigma}$=0.51. That no diamond growth was

observed when using a CO/H_2 plasma shows an inconsistency with the original work of Bachmann *et al.*, since growth is clearly dependent upon the source of C, H and O in the feed gas, and not just the C/O ratio.

It was also found that the same T_{gas} eg. 2800 K, can be reached in a $CH_4/CO_2/H_2$ plasma at 1 kW, compared to a CH_4/H_2 plasma, which requires 1.5 kW at the same pressure and flow rate. Data returned by the model showed that the reason for this was the decreased thermal conductivity coefficient of C/H/O plasmas compared to C/H plasmas. This allows the input power to be better retained in the localized plasma volume.

CRDS and OES were also used to study C/N/H plasmas. CRDS results showed that NH and CN column density depend strongly on whether N_2 or NH_3 is used in the feed gas mixture. This is thought to be due to the strength of the N_2 bond in comparison to the N-H bond, and it was found that NH column densities stretched to regions of lower T_{gas} when using NH_3, than when using N_2 in the source gas. Lower NH column densities achieved in N_2/H_2 plasmas in comparison to NH_3/H_2 plasmas also resulted in a larger % decrease in NH with the addition of CH_4 into the source gas. This is a result of reactions between C and N containing radicals, which show a larger % drop in [NH] when there is less NH to begin with. CN column density was also found to be greater in $NH_3/CH_4/H_2$ plasmas compared with $N_2/CH_4/H_2$ plasmas, which can be attributed to greater [NH] in NH_3 plasmas, being available to react with C_XH_y species, than in N_2 containing plasmas. Due to the difficulty in measuring NH under conditions suitable for measuring CN and vice versa, it is difficult to assert which species will be in greater concentration near the growing surface, without use of a 2D model. This means that at this stage, from gas phase diagnostics alone, it is difficult to tell whether it is likely that NH or CN radicals may have the greater role in the increased diamond growth rate observed with the inclusion of N into the gas phase.

In order to compliment the modelling and experimental studies of the gas phase chemistry for O and N containing plasmas, computational methods were used to study reactions on a diamond surface. OH, N, NH, NH_2, CN and CNH radicals were investigated to see which species were most likely to incorporate into diamond. Calculated energies suggested that an adsorbed OH radical should incorporate into

diamond, however little O is found in diamond experimentally. Routes for the loss of O from the surface were investigated, however none of these provided a mechanism of low enough energy to compete with that for O incorporation. In terms of N incorporation, only the routes for N and CNH were of low enough energy to be plausible. The calculated route for CNH incorporation was promising, as it left a pendant N group above the growing diamond surface, which could increase diamond growth rates by acting as a nucleation site for growth of a new layer. These results prevent viable routes for N incorporation by both N and CN, which do not narrow down the search for whether NH or CN are the most likely growth species. Identifying pathways for N incorporation helps to validate calculations by Yiming *et al.*, for N 1-3 atomic layers below the surface, and the effect this has on increasing growth rates.

7.2 Future work

Further investigations are yet to be completed for nitrogen containing plasmas. Column densities of the CN radical have been measured at high P, whilst increasing p, increased substantially once p>200 Torr. The distribution of CN at p>200 Torr is not yet fully understood, therefore, plasma profiling should be completed at p>200 Torr.

The relative reactivity of N_2 and NH_3 in nitrogen containing plasmas requires work. It is important to understand the mechanism of forming N_2 in NH_3 containing plasmas (with and without the presence of CH_4), and this requires OES. It is possible that N_2 may be forming on the reactor walls, or the metal substrate, and this work is ongoing. Measurement of N_2* and CN* in NH_3 containing plasmas has also yet to be completed. CRDS investigations, measuring NH column densities, are also to be re-visited. These investigations will focus further on the change in NH column density when moving from NH_3 to N_2 in the feed gas, and back (with and without the presence of CH_4).

Work which is slightly further into the future involves re-designing the MW reactor, as the current reactor design does not allow for estimation of the properties of

electrons ie. T_e and n_e. The MW reactor is currently being redesigned in order to generate short pulses of bias voltage, and investigate electron properties via spatially resolved OES.

The QM modelling for reactions of N containing plasmas is complete, showing energetically feasible pathways for CNH and N, which are yet to be investigated using QM/MM calculations, although all previous work suggests that there is little difference between the two methods. An interesting project which would bridge the gap between the surface reactions completed in this thesis, and the work by Yiming *et a*,[1] would be to calculate the steps leading to the incorporation of N as a dopant in the sub-surface layers of diamond. This method could also be applied to diamond growth incorporating a surface (divalent) O group, and may provide a mechanism for the removal of O.

7.3 References

1. Yiming, Z., Larsson, F., Larsson, K., Effect of CVD diamond growth by doping with nitrogen. *Theor. Chem. Accounts*

Appendix A Species concentrations in C/H/O plasmas

Table A. 1. Gas temperatures (T_{gas} / K) and selected species concentrations (in cm^{-3}) above the substrate centre (at z = 0.5 mm) returned by the present 2-D modelling for a range of C/H/O gas mixtures. Where p=150 Torr and P = 1 kW.

Feed gas	30%CH_4/ 40%CO_2/ 30%H_2	35%CH_4/ 35%CO_2/ 30%H_2	40%CH_4/ 30%CO_2/ 30%H_2	2.55%CH_4/ 2.45%CO_2/ 95%H_2	2.85%CH_4/ 2.15%CO_2/ 95%H_2	41.2%CO/ 58.8%H_2
T_{gas} / K	1460	1385	1469	1273	1272	1385
H	1.27E+16	9.23E+15	8.89E+15	6.22E+15	6.03E+15	1.15E+16
CH_3	8.28E+11	2.55E+13	4.85E+13	1.03E+14	1.15E+14	9.73E+12
$^3CH_2$	2.44E+10	1.92E+11	2.58E+11	2.44E+11	2.55E+11	1.24E+11
$^1CH_2$	5.55E+08	7.37E+09	1.77E+10	6.94E+09	7.48E+09	3.24E+09
CH	3.09E+09	1.44E+10	1.63E+10	7.01E+09	7.06E+09	1.08E+10
C	1.25E+11	1.88E+11	9.92E+10	2.84E+10	2.52E+10	3.39E+11
$C_2(a)$	2.36E+04	5.93E+07	1.12E+09	1.21E+07	1.75E+07	5.36E+06
$C_2(X)$	1.19E+03	1.54E+07	3.53E+08	1.20E+06	1.44E+06	1.07E+06
C_2H	1.42E+06	3.13E+10	6.71E+11	8.34E+09	1.03E+10	2.05E+09
C_2H_2	4.40E+10	2.82E+15	3.38E+16	4.05E+15	5.16E+15	1.68E+14
C_2H_3	5.51E+07	4.07E+12	3.25E+13	7.57E+12	9.51E+12	2.58E+11
C_2H_4	4.35E+08	5.06E+13	3.62E+14	2.48E+14	3.20E+14	2.95E+12
C_2H_5	5.25E+05	1.84E+10	9.23E+10	1.66E+11	2.15E+11	1.13E+09
C_2H_6	8.86E+06	2.85E+10	7.82E+10	1.23E+12	1.61E+12	2.78E+09
C_3	7.36E+07	1.41E+13	6.88E+13	2.61E+12	3.21E+12	1.08E+12
C_3H	4.88E+05	1.32E+11	8.29E+11	4.43E+10	5.76E+10	9.04E+09
C_3H_2	1.50E+08	6.92E+13	4.29E+14	6.88E+13	9.28E+13	4.25E+12
C_3H_3	8.00E+05	3.62E+11	4.22E+12	4.38E+11	6.07E+11	1.97E+10
C_4	2.43E-01	3.92E+05	2.99E+07	2.72E+04	3.69E+04	1.20E+04
C_4H	1.20E+01	5.98E+07	5.96E+09	1.40E+07	2.01E+07	1.23E+06
C_4H_2	1.75E+05	3.13E+12	1.91E+14	4.11E+12	6.09E+12	5.20E+10
C_6H_6	5.30E+01	6.86E+09	5.61E+11	3.35E+10	6.37E+10	1.57E+07
H(n=2)	2.19E+06	2.61E+06	4.51E+06	6.11E+06	6.04E+06	2.22E+06
H(n=3)	8.02E+04	1.05E+05	1.69E+05	3.80E+05	3.76E+05	8.26E+04
O_2	7.58E+10	8.17E+05	4.88E+04	5.48E+07	3.12E+07	1.89E+06
H_2O	3.73E+16	1.71E+14	2.55E+13	5.01E+15	3.84E+15	3.03E+14
O	6.13E+11	2.67E+09	1.56E+09	2.70E+09	2.03E+09	2.83E+09
OH	2.44E+13	5.18E+10	1.14E+10	3.33E+11	2.45E+11	1.01E+11
HCO	9.78E+11	9.47E+11	6.45E+11	2.61E+11	7.68E+10	8.98E+11
CH_2O	1.19E+10	1.01E+10	9.66E+09	8.41E+09	4.34E+09	8.64E+09
CH_3O	3.86E+05	2.63E+04	1.43E+04	7.34E+05	6.23E+05	1.61E+04
CO(a)	2.55E+10	3.81E+10	7.50E+10	8.56E+09	7.93E+09	2.78E+10
e	3.82E+10	3.07E+10	7.17E+10	9.40E+10	9.40E+10	3.18E+10

$C_2H_2^+$	1.24E+05	2.47E+10	5.65E+10	1.55E+10	2.41E+10	4.60E+09
$C_2H_3^+$	1.05E+02	1.11E+09	1.48E+10	2.56E+08	3.88E+08	1.04E+08
H_3O^+	3.82E+10	4.84E+09	4.28E+08	7.83E+10	6.95E+10	2.70E+10
CH_4	2.36E+12	1.18E+14	1.83E+14	1.29E+15	1.48E+15	4.33E+13
CO_2	9.64E+15	4.21E+13	9.71E+12	2.68E+13	1.86E+13	5.39E+13
CO	4.65E+17	4.69E+17	3.97E+17	2.88E+16	2.60E+16	4.03E+17
H_2	4.68E+17	5.65E+17	5.46E+17	1.09E+18	1.10E+18	6.32E+17

Appendix B Constants used in analysis of CRDS data

Table B. 1. List of wavenumbers, upper and lower level degeberacies and Einstein A coefficients and Pgopher constants for transitions used in this work. These are given for C_2[1], CH[1,2], OH[3,4], NH[5] and CN[6].

Species Transition	J	$\bar{\nu}$/cm^{-1}	A / s^{-1}	g upper	g lower	P At 2800 K
C_2 (d-a) 0,0	$R_{3f}(8)$	19422.97	7.21×10^6	6	6	0.00261
	$R_{2e}(9)$	19424.12	7.21×10^6	6	6	0.00287
	$R_{1f}(10)$	19425.42	7.21×10^6	6	6	0.00317
	$P_{3e}(37)$	19426.39	7.21×10^6	6	6	0.00343
CH (A-X) 0,0	$R_{1e}(15)$	23422.98	1.85×10^6	4	4	0.00509
	$R_{1f}(15) + R_{2f}(13)$	23424.88	1.85×10^6	4	4	0.00963
	$R_{2e}(13)$	23426.99	1.85×10^6	4	4	0.00454
CH(B-X)	$R_1(12.5)$	25736.53	2.8×10^6	4	4	0.006636
	$R_1(13.5)$	25737.82	2.5×10^6	4	4	0.006146
OH (A-X) 0,0	$Q_{21}(3.5)$	32582.11	1.45×10^6	4	4	0.00287
	$R_1(3.5)$	32587.43	1.45×10^6	4	4	0.00539
	$R_2(11.5)$	32588.63	1.45×10^6	4	4	0.00605
NH(A-X)	$P_1(10)$	29466.02	2.44×10^6	6	6	0.00376
	$P_{32}(9)$	29471.65	2.44×10^6	6	6	0.00332
CN(B-X)	$P_1(20.5)$ $P_2(19.5)$	25748.1	1.48×10^7	4	4	0.017229
	$P_1(36.5)$ $P_1(19.5)$ $P_2(18.5)$	25749.28	1.48×10^7	4	4	0.016853
	$P_1(37.5)$ $P_1(18.5)$ $P_2(17.5)$	25750.63	1.48×10^7	4	4	0.016422
	$P_1(38.5)$ $R_1(2.5)$ $R_2(1.5)$	25810.04	1.48×10^7	4	4	0.002879

References

1. Wills, J. B. *et al.*. Measurements of C_2 and CH concentrations and temperatures in a dc arc jet using cavity ring-down spectroscopy. *J. Appl. Phys.* **92,** 4213 (2002).

2. Garland, N. L. & Crosley, D. R. Relative transition probability measurements in the A-X and B-X systems of CH. *J. Quant. Spectrosc. Radiat. Transf.* **33,** 591–595 (1985).

3. Cageao, R. P. *et al.*. Calculated hydroxyl $A^2\sum \rightarrow X^2\Pi$ (0, 0) band emission rate factors applicable to atmospheric spectroscopy. *J. Quant. Spectrosc. Radiat. Transf.* **57,** 703–717 (1997).

4. Luque, J. & Crosley, D. R. Transition probabilities in the $A^2\Sigma^+ - X^2\Pi$ electronic system of OH. *J. Chem. Phys.* **109,** 439 (1998).

5. Kirby, K. P. & Goldfield, E. M. Theoretical study of the radiative properties of the triplet states of the NH radical: Transition dipole moments, radiative lifetimes, photodissociation cross sections. *J. Chem. Phys.* **94,** 1271 (1991).

6. Bauschlicher Jr, C. W., Langhoff, S. R. & Taylor, P. R. Theoretical study of the dissociation energy and the red and violet band systems of CN. *Astrophys. J.* **332,** 531–538 (1988).